Tuning light-induced superconductivity in K_3C_{60}

Dissertation

zur Erlangung des Doktorgrades an der Fakultät für
Mathematik, Informatik und Naturwissenschaften

Fachbereich Physik
der Universität Hamburg

Vorgelegt vor

Alice Cantaluppi

aus Como, Italien

Hamburg

2017

Gutachter der Dissertation: Prof. Dr. Andrea Cavalleri
Prof. Dr. Wilfried Wurth

Zusammensetzung der Prüfungskommission:
Prof. Dr. Andrea Cavalleri
Prof. Dr. Alexander Lichtenstein
Prof. Dr. Michael Martins
Prof. Dr. Ludwig Mathey
Prof. Dr. Michael Rübhausen

Vorsitzender des Prüfungskommission: Prof. Dr. Michael Rübhausen

Datum der Disputation: 29/01/2018

Vorsitzender des Promotionsausschusses: Prof. Dr. Wolfgang Hansen

Leiter des Fachbereich Physik: Prof. Dr. Michael Potthoff

Dekan der Fakultät MIN: Prof. Dr. Heinrich Graener

Hiermit erkläre ich an Eides statt, dass ich die vorliegende Dissertationsschrift selbst verfasst und keine anderen als die angegebenen Quellen und Hilfsmittel benutzt habe. Diese Arbeit lag noch keiner anderen Person oder Prüfungsbehörde im Rahmen einer Prüfung vor.

I hereby declare, on oath, that I have written the present dissertation on my own and have not used other than the mentioned resources and aids. This work has never been presented to other persons or evaluation panels in the context of an examination.

Hamburg, den   Alice Cantaluppi

Abstract

Recently, excitations with intense, ultrashort laser pulses have emerged as effective means to drive complex solids away from equilibrium and change their functional properties transiently. The most attractive feature of this approach is the capability of *coherently* and *selectively* exciting a targeted degree of freedom, as well as the possibility of driving these excitations at very high speed.

The resonant excitation of terahertz-frequency lattice distortions in different complex solids allows for the tuning of these materials across different, sometimes intertwined broken symmetry ground states. It also provides a route for accessing hidden phases.

In recent investigations of the cuprate superconductors, the excitation of specific lattice vibrations has been used to demonstrate transient light-induced superconductivity, observed at temperatures far higher than the equilibrium critical temperature. In a similar way the vibrational excitation of molecular superconductors based on alkali doped fullerides will be shown here to induce dramatic changes in their electronic properties.

Crucially, the A_3C_{60} are strongly affected by local interactions at each C_{60} site, and distortions along local molecular modes are strongly coupled with changes in the electronic ground state. The three-dimensional organic molecular superconductor K_3C_{60} has been investigated in this thesis. It has been shown that the equilibrium superconducting properties of K_3C_{60} can be en-

hanced by the resonant excitation of an intramolecular vibration, and that the high temperature metal can be turned into a non-equilibrium state with the optical conductivity of a superconductor.

This new physics has been investigated here also in combination with the application of external hydrostatic pressure. The key finding is that as pressure is applied, the strength of the transient superconducting phase reduces, as expected in an equilibrium superconductor. This finding strengthens the interpretation of the out-of-equilibrium phase of K_3C_{60} as a finite-lifetime superconductor, which is observed up to room temperature.

Zusammenfassung

Anregungen mit intensiven, ultrakurzen Laserpulsen haben sich in letzter Zeit als ein wirkungsvolles Mittel erwiesen, um komplexe Festkörper aus dem Gleichgewichtszustand auszulenken und um ihre funktionellen Eigenschaften vorübergehend zu verändern. Das attraktivste Merkmal dieses Ansatzes ist die Fähigkeit, kohärent und selektiv einen gezielten Freiheitgrad mit sehr hoher Geschwindigkeit anzuregen.

Die resonante Anregung von Gitterverzerrungen im Terahertz Frequenzbereich in verschiedenen komplexen Festkörpern ermöglicht die Einstellung ihrer Materialeigenschaften über verschiedene, teilweise ineinander verschlungene, gebrochene Symmetrie-Grundzustände. Außerdem bietet es einen Zugang zu versteckten Phasenzuständen.

In neueren Untersuchungen der Cuprat-Supraleiter wurde die Anregung spektraler Gitterschwingungen genutzt, um transiente, durch Licht induzierte Supraleitung bei Temperaturen zu demonstrieren, die weit über der kritischen Temperatur im Gleichgewicht liegen. In ähnlicher Weise wird hier gezeigt, dass die Schwingungsanregung molekularer Supraleiter auf der Basis alkali-dotierter Fulleride genutzt werden kann, um dramatische Veränderungen ihrer elektronischen Eigenschaften zu induzieren.

Bemerkenswert ist, dass die A_3C_{60}-Eigenschaften durch lokale Interaktionen an jedem C_{60}-Standort stark beeinflusst werden und Verzerrungen entlang der lokalen molekularen Moden stark an Veränderungen im elektronischen

Grundzustand gekoppelt sind. In dieser Arbeit wurde der dreidimensionale organische molekulare Supraleiter K_3C_{60} untersucht. Es hat sich gezeigt, dass die Gleichgewichtssupraleitung von K_3C_{60} durch die resonante Anregung einer intramolekularen Schwingung verbessert werden kann und dass der metallische Zustand bei hohen Temperaturen in einen Nichtgleichgewichtszustand mit der optischen Leitfähigkeit eines Supraleiters überführt werden kann.

Diese neue Physik wurde hier auch in Kombination mit der Ausübung von externem hydrostatischen Druck untersucht. Das Schlüsselergebnis ist, dass sich die Stärke der transienten supraleitenden Phase mit zunehmendem Druck verringert, wie es in einem Gleichgewichtssupraleiter zu erwarten ist. Dieses Resultat bekräftigt die Interpretation der Nichtgleichgewichtsphase von K_3C_{60} als einen bis zur Raumtemperatur beobachtbaren Supraleiter mit endlicher Lebensdauer.

List of Pubblications

The present thesis is based on my work as a doctoral student at the Max Planck Institute for the Structure and Dynamics of Matter, Hamburg, within the Quantum Condensed Matter Division and at the University of Hamburg. In addition, I am grateful to The Hamburg Centre for Ultrafast Imaging (CUI) for partly funding the present work.

The results presented in this manuscript are based on the following papers:

1. **A. Cantaluppi**, M. Buzzi, D. Nicoletti, M. Mitrano, D. Pontiroli, M. Riccò, A. Perucchi, P. Di Pietro, A. Cavalleri, *Pressure tuning of light-induced superconductivity in K_3C_{60}*, arXiv:1705.05939 (2017).

2. M. Mitrano, **A. Cantaluppi**, D. Nicoletti, S. Kaiser, A. Perucchi, S. Lupi, P. Di Pietro, D. Pontiroli, M. Riccò, S. R. Clark, D. Jaksch, and A. Cavalleri, *Possible light-induced superconductivity in K_3C_{60} at high temperature*, *Nature*, 530, 461–464 (2016).

Other publications beyond the ones related to the results discussed in the thesis:

1. T. F. Nova, A. Cartella, **A. Cantaluppi**, M. Först, D. Bossini, R. V. Mikhaylovskiy, A. V. Kimel, R. Merlin, A. Cavalleri, *An effective magnetic field from optically driven phonons*, *Nature Physics*, 13, 2, 132–136 (2017, Adv. Online 2016).

Contents

Introduction

Most materials in nature display several ground states that can be accessed by varying external parameters. At a given temperature, pressure and volume, a material exhibits a specific phase, and under the right conditions, it experiences phase transitions. Condensed matter systems can be found in complex ground states not only defined by atomic or molecular density, but that emerge from other more subtle orders.

Important information on a system at equilibrium are gained from the observation of how it evolves with varying external conditions. This becomes rather challenging when a multitude of degrees of freedom are intertwined together in a non-trivial way. From the competing requirements of minimising the total internal energy of a system and maximising its entropy, finally, a specific phase sets over the other ones [1].

Most phase transitions are often accompanied by the appearance of order, from an otherwise (dis)ordered system. A (anti)ferromagnet, for example, emerges across the critical temperature when the spins of the lattice arrange themselves in a (anti)parallel fashion, or, similarly, a superconductor forms at cold temperatures when a macroscopic order sets in the electronic wave function [2].

In condensed matter, symmetries are commonly invoked to differentiate amongst different phases. The ground state of a given system can be described, for example, in terms of conservation of translational, rotational or temporal
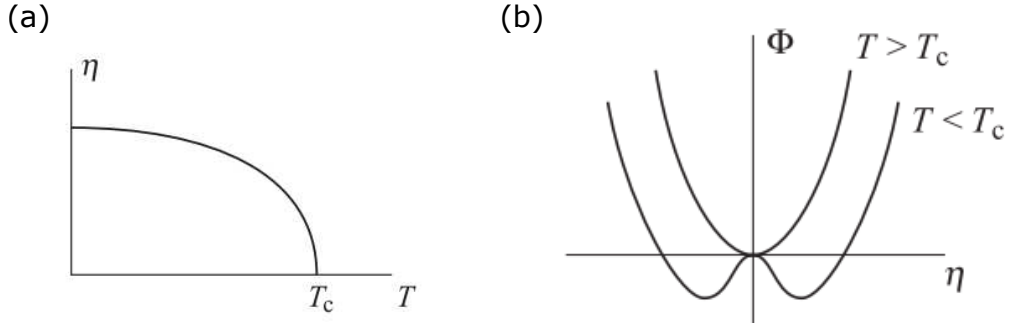
Figure 1: **(a)** Continuous evolution of the order parameter η across a second order phase transition as a function of temperature. **(b)** Free energy ϕ across a second order phase transition plotted as a function of order parameter η, accompanied by a breaking of a symmetry. While the equilibrium position of the highly symmetric phase is centred at zero, below T_c two distinctive minima appear leading to symmetry breaking [1].

symmetry. Finding symmetries in complex structures constitutes a valid way to simplify a problem with mathematical formalism.

In the case of a solid, rigidity, superconductivity or ferromagnetism are the result of new equilibria emerging once a certain symmetry is lost [3, 1]. It is of interest understanding the mechanisms behind the formation of the characteristic collective modes, as they occur only in the macroscopic phase and not at the atomic level, where symmetries and broken symmetries are ill-defined.

Phase transitions accompanied by a gradual reduction of symmetry are commonly referred as continuous or second order phase transitions. Such transitions are usually described by an *order parameter* whose magnitude accounts for the degree of broken symmetry, and it continuously evolves from zero in the symmetric phase to a finite value (see Fig 1**(a)**).

At equilibrium the state of the system is set by the condition of the minimum of the corresponding thermodynamic potential, i.e. its free energy. It is possible to express this latter quantity as an expansion of the order parameter, which holds for the overall symmetry of the system [1]. As schematically represented in Fig. 1**(b)**, once a symmetry is broken below the critical transition temperature ($T < T_c$), new energy minima of the free energy are unveiled and phenomena like collective electronic interactions such as antiferromag-
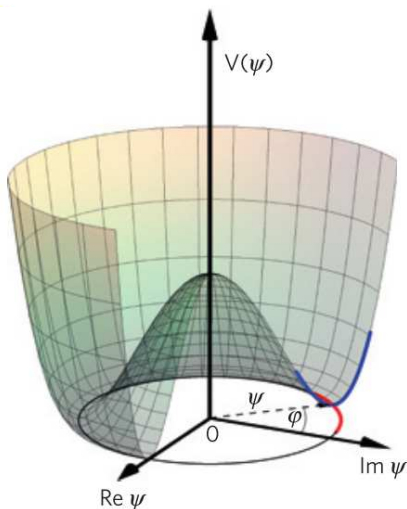
Figure 2: Characteristic Mexican hat potential, with a circle of potential minima along the brim (black solid circle). Transverse modes of the order parameter $\psi = |\psi|e^{i\phi}$ along the brim (red line) are Nambu–Goldstone (phase) modes, and longitudinal modes (blue line) are Higgs (amplitude) modes associated with a finite energy [5].

netic or superconducting states can be stabilised.

Conventional superconductivity emerges from a spontaneous symmetry breaking associated with particle number conservation [4]. As the metal turns into a superconductor below fairly low transition temperatures, the electrons at the Fermi surface feel an attractive potential and Cooper pairs are formed. In conventional superconductors, explained by means of the standard Bardeen-Cooper-Schrieffer (BCS) theory, the electron-electron attractive potential is generally attributed to electron-lattice interactions. The superconducting condensate results from the condensation of all the bosonic pairs into the same ground state and is macroscopically described by a single wave function $\psi = |\psi|e^{i\phi}$ which holds phase-coherence over long distances.

The potential, i.e. the free energy, across the broken-symmetry superconducting phase transition evolves into a Mexican hat shaped potential, expressed as a function of the complex order parameter ψ (see Fig 2) [4]. Excitations from the ground state, defined by a specific phase ϕ of the bosonic wavefunc-

tion, can be classified as transverse phase modes (Nambu–Goldstone) and massive longitudinal amplitude modes (Higgs) (see blue and red lines in Fig. 2) [5].

BCS theory nicely describes conventional superconductivity; however it fails in describing high temperature superconductors where electronic coherence derives from other broken symmetries [6, 4]. In the last years high-T_c superconductors have been widely investigated, aiming at bringing to light more insights of the possible responsible mechanism behind it.

The discovery and stabilisation of specific phases of matter often brings important technological innovations. External perturbations constitute interesting tools to unbalance the existing strong interactions and may support the onset of new stable broken-symmetry states. Pressure, chemical doping and magnetic fields are well known variables that allow moving among different adjacent phases of a complex system. The observation of the emergent equilibrium phase diagrams allowed scientist reaching specific interpretations to various problems [7, 8, 9].

On the same lines, unstable equilibria of physical systems can be dynamically stabilised by external periodic perturbations [10]. The recent advent of intense ultrashort laser pulses stands as a breakthrough for new selective excitation of a broader number of parameters in condensed systems which could be used to possibly induce phase switching [11, 12].

In a crystal, most of the intertwined degrees of freedom are associated with the broken translational order [13]. Electromagnetic radiation can launch vibrational excitations in periodic crystalline structures and can therefore lead to dramatic changes in the physics of the system. Importantly, light *selectively* activates coherent dynamics in a solid, unlike other kinds of external stimuli, offering the possibility of a more accurate study of the emergent transient states. The final behaviour of the driven non-equilibrium phase will strongly depend on the specific photo-induced broken-symmetry.

In light of the recent technological development, strong resonant low-energy excitations can additionally be used to drive the material beyond the linear regime. As a result, as discussed more in details in Chapter 1, the directly excited degrees of freedom couple nonlinearly to other ones, such magnetic
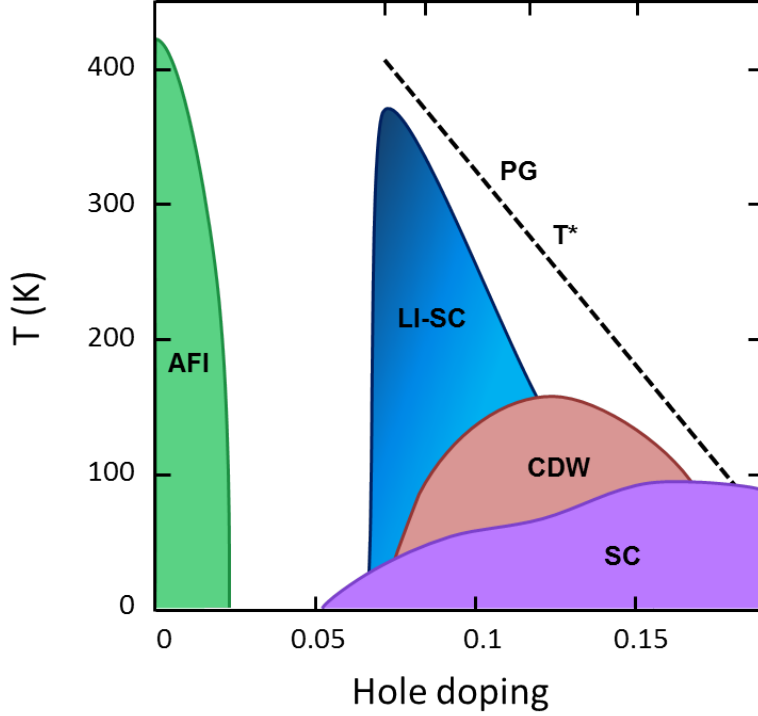
Figure 3: Schematic out-of-equilibrium phase diagram for $YBa_2Cu_3O_{6+x}$ as a function of holes concentration. On top of the equilibrium superconducting (SC), antiferromagnetic (AFI) and charge-density wave (CDW) phases, a light-induced superconductivity (LI-SC) phase arises when the material is resonantly driven at mid-infrared frequencies. The black dashed line identifies the pseudo-gap (PG) crossover across T^* [17, 18].

spin waves [14] and, specifically to the case of molecular solids, on site electronic correlations [15, 16].

The strong connection between structural and electronic degrees of freedom in superconducting materials stresses further the potential of the optical excitations of lattice distortions. The recent resonant selective excitation of low energy phonons responsible for the pairing of the electrons in copper superconductors has finally unveiled that it is possible to strengthen the superconducting fluctuations even up to room temperature [17]. For the specific case of $YBa_2Cu_3O_{6+x}$, it is then possible to draw an attempted out-of-equilibrium phase diagram, shown in Fig. 3, in which light-induced superconducting phase (LI-SC) has been added to the equilibrium plot [17, 18].

In order to understand whether this excitation scheme could be used to a more general class of materials, the more conventional fullerides superconductors have been excited by means of ultrashort strong laser pulses. This thesis reports the evidence of ultrafast light-induced dynamics in alkali doped fullerides. The resonant excitation of vibrational molecular modes is expected to break or restore some of the existing symmetries and thus bring the system into new out-of-equilibrium phases.

In 1985 Kroto et al. combined sixty carbon atoms together to form the so called "Buckminsterfullerenes", which have the characteristic soccer ball atomic arrangement illustrated in Fig. 4 [19]. This molecule belongs to the highest symmetry spatial group and are invariant under rotational, reflection, and inversion symmetry. Combining all the possible transformations, one finds 120 different symmetry operations which leave the C_{60} molecules unaffected. Fullerenes may look simple due to their high symmetry and elementally purity; however the large number of atoms involved leads to complicated dynamics [20].

C_{60} molecular solids are insulating as their highest molecular orbital is completely filled. Alkali atoms are commonly used to dope these solids that become metallic. Interestingly, the macroscopic properties of alkali doped fullerides are defined by on-ball physics, dominated by electronic and structural orders. This leads to a coexistence of multiple low energy scales that favour the onset of specific ground states [21].

This thesis will describe the recent finding of an out-of-equilibrium superconducting phase emerging in potassium-doped fullerides in response to the resonant excitation of a C_{60} vibrational mode [23, 24]. This result provides an additional evidence of light-induced material control of condensed matter systems.

The understanding of the onset of such transient superconducting-like state at very high temperatures represents still a massive challenge for theoretical investigation; whether this phenomenology is associated to any breaking of existing symmetries remains the major open question.

At the beginning of this thesis, Chapter 1 will briefly recall some of the most recent experimental evidences of low-energy resonant vibrational excitation
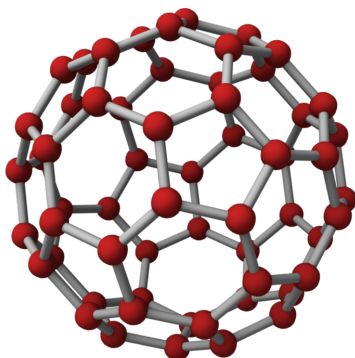
Figure 4: C_{60} molecule discovered in 1985 by Kroto et al.. This molecule belongs to the highest symmetry spacial group and are invariant under rotational, reflection, and inversion symmetry[19]. Image adapted from [22].

of solids, in particular in connection to their superconducting properties. A wider playground opens when molecular solids are excited out of their equilibria. The equilibrium physics of the alkali-doped fullerides representing the only three-dimensional organic molecular conductors will be then discussed in Chapter 2.

The rest of the thesis will focus then on the characterisation of the optical response of potassium-doped fullerides K_3C_{60} at equilibrium (Chapter 3) and out-of-equilibrium (Chapter 4 and 5). Chapter 4, in particular, widely discusses the optical response of potassium doped fullerides K_3C_{60} to local molecular vibrational excitation. When light excites the material, superconducting features appear in its optical response at temperatures higher than the equilibrium T_c. This hints for a light-induced stiffening of the superconducting fluctuations over other perhaps competing orders. Interestingly, as described finally in Chapter 5, the transient superconducting like phase disappears when the material is pressurised.

The suppression of the out-of-equilibrium superconducting like phase in potassium doped fullerides by means of pressure stands for a more unequivocal interpretation of the light-induced phase as a finite-lifetime superconductor.

CHAPTER 1

Light control of complex materials

The capability of light to interact with matter has been intensively exploited since its discovery, aiming at understanding fundamental functional properties of solids and their possible application. In the simplest light-matter interaction scheme, e.g. in a linear optical reflectivity measurement, the incident light weakly perturbs the system and from the observation of the reflected light, information about its equilibrium response can be retrieved. Higher order response, beyond the linear regime can, on the other hand, be triggered in several materials by means of the significantly high electromagnetic peak energies. Sub-picosecond laser pulses can be used to push the system to higher responses. When such pulses impinge on a system, they drive it out of equilibrium and from the observation of its de-excitation, information about the participating dynamics can be extracted.

From the study of both the linear and nonlinear response of a material together, a complete picture of the system can be extracted.

The relevance of such excitations will be widely discussed in the rest of the chapter.

1.1 Light control of strongly correlated materials

Solids can be driven into excited states characterised by new optical properties by means of strong electromagnetic radiation. The type and variety of light sources needed for a nonlinear investigation of matter has grown exponentially in the last years, covering the entire electromagnetic spectrum, from hard X-ray to far-infrared. Diverse techniques allowed for different spectroscopic investigations leading to a broader understanding of matter, and to consequent technological progress.

Over the past few decades, pulsed electromagnetic radiation has been widely employed to control the behaviour of matter in its different phases. On one side, the strong intensity delivered by pulsed lasers has been exploited for high energy excitations, from the visible to the ultraviolet, primarily aiming at the perturbation of high electronic excited states in soft and condensed matter systems [25]. A different type of investigation relies, on the other hand, on the excitation of a system by means of low energy radiation, up to a few eV. When a system is driven by low energy photons, it remains in its electronic ground state and the transfer of entropy is minimised. In this scenario, hence, the emergent out-of-equilibrium phase is expected to depend not only on the electronic response, but also on one of other "heavier" degrees of freedom (e.g. ions).

Beyond its capability of reaching extremely high electric fields, pulsed laser radiation is *coherent*. When coherent light impinges on a sample, a specific phase can be transferred during the interaction, and controlled dynamics can be launched inside the material. This aspect becomes of peculiar interest when the probed system is inclined to collective excitations, e.g. coherent phonons and magnons, that can be stimulated by means of coherent light.

Strongly correlated materials are defined as systems in which the electronic motion is constrained by the Coulomb repulsion and it becomes strictly entangled. This phenomenon leads to the emergence of spectacular ground state properties, such as metal-to-insulator transitions or the appearance of nonconventional superconductivity, and to very large susceptibilities to rela-
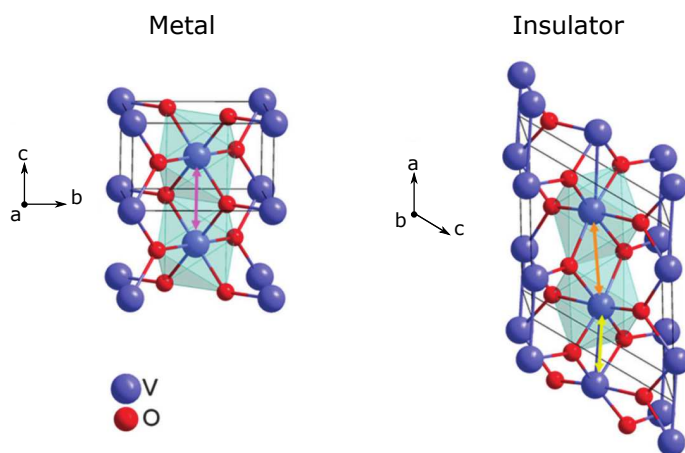
Figure 1.1: Crystallographic transformation from the high-temperature tetragonal rutile (left side) to low-temperature monoclinic (right side) structure in VO_2 associated to the metal-to-insulator phase transition. Figure adapted from [26].

tively weak perturbations [27, 28].

Even if strongly correlated materials are mainly defined by strong electronic interacting forces, their properties result from the coexistence of these latter with other type of interactions. In the late sixties, for example, a structural rearrangement of the ions in the unit cell of some vanadates has been observed accompanying the metal to insulator transition across the critical temperature [29]. While the system is conducting in his high-temperature tetragonal rutile phase (on the left in Fig. 1.1), an insulating phase emerges as the crystalline structure evolves to monoclinic at low temperatures (right panel of Fig. 1.1).

The striking recent observation of a light-induced insulator-to-metal transition in such structure, associated to a structural deformation unveiled the possibility of achieving coherent control of phase transitions [30]. The optimisation of the excitation conditions to maximise a specific product state became therefore of major interest in the scientific community.

By means of intense sub-picosecond laser pulses in the mid-infrared and terahertz regime, low-energy excitations capable to extend beyond the linear regime became accessible. A variety of interesting physical processes have been explored so far and some of the pioneering experiments will be shortly
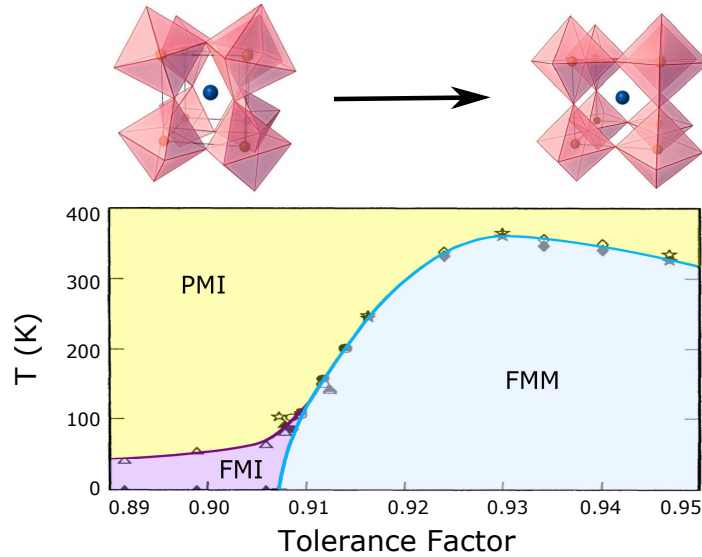
Figure 1.2: Phase diagram temperature vs tolerance factor for the system $A_{0.7}A'_{0.3}MnO_3$, where A is a trivalent rare earth ion and A' is a divalent alkali earth ion. As the crystalline structure is perfectly cubic (tolerance factor approaches the unity) the system is metallic (FMM), while the distorted structure shows an insulating response (paramagnetic or ferromagnetic, PMI or FMI). Figure adapted from [31].

discussed in the rest of the chapter.

1.2 Light-induced metallicity in manganites

The first experimental demonstration of a light-induced insulator-to-metal transition driven by the direct stimulation of the crystal lattice with resonant low-energy pulses has been obtained on manganites AMO_3. In these solids eight oxygen atoms surround the manganese atom to form an octahedron, as depicted in Fig. 1.2. The tilting angle of the octahedra with respect to the crystallographic axis is quantified as tolerance factor and is a fundamental factor in determining the electronic state (see Fig. 1.2). The overlap between the orbitals of the Mn and O atoms influences in fact the hopping integral of the electrons. The more distorted is the structure the more the Coulomb repulsion dominates over the electronic mobility and the material becomes insulating (left side of the phase diagram in Fig. 1.2).

Strong mid-infrared pulses have been used to resonantly excite the Mn-O stretching mode in $Pr_{0.7}Ca_{0.3}MnO_3$ involving the ions relevant for the tolerance factor. A colossal enhancement of the optical conductivity, of more than five orders of magnitude, has been measured in the driven system [32]. The microscopic mechanism beyond this phenomenology has been later on identified in terms of anharmonic phonon coupling. The excitation of the infrared-active mode in manganites by means of strong mid-infrared pulses results in large oscillations of the involved ions. As described in more detail in the next section, upon strong resonant excitations a net displacement of the crystalline structure along other phononic coordinates can take place [33].

In the specific case of manganites the excitation of the Mn-O stretching mode results in an effective net displacement along the Raman coordinate associated to a rotation of the oxygen octahedra. The reconstructed electronic structure based on dynamical mean-field theory (DMFT) provides a clean explanation for the observed metal to insulator phase transition [12].

In the next section the theory of nonlinear phonon coupling will be introduced. As aforementioned, the large oscillations launched by means of the resonant MIR pulses, is expected to indirectly induce a net displacement of the solid structure along the eigenvectors of other specific phonons. On one hand, this theory explains the light-induced phase transition observed in the manganites upon resonant excitation of a MIR phonon, but it also constitutes an extremely useful tool that can be used to target other types of coherent excitations in solids.

1.2.1 Theory on nonlinear phononics

Being electromagnetic radiation an oscillating wave of electric field, it couples only to charge quasiparticles which carry an effective non-zero electric dipole moment. Atoms in a solid are always in motion. Coherent light allows bringing all the random movement of the ions in phase, inducing a collective phase relation to the vibrating ions extending over macroscopic spatial range. The resulting collective phase-locked ionic oscillations goes under the name
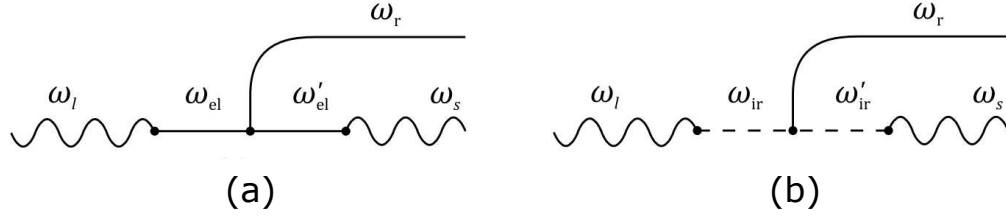
Figure 1.3: **(a)** Impulsive stimulated Raman scattering (IRSR). The excitation of the Raman mode at its own eigenfrequency ω_r is mediated by the electronic scattering ($\omega_{el} \rightarrow \omega'_{el}$). **(b)** Ionic Raman scattering (IRS). The excitation of the Raman mode is assisted by the infrared active mode ω_{ir}. Both processes are triggered by an incident photon at frequency ω_l and emit at ω_s. Figure adapted from [37].

of *coherent phonons.*

When light excites an infrared active mode, large coherent oscillations are launched along its specific eigenvectors. Many functional properties of condensed systems, on the other hand, are related not only to phonons which can be excited directly by means of light but also to ionic vibrations with no net dipole moment. Extending the concept of selective optical coherent drive to more general excitations, e.g. to symmetric Raman modes, becomes therefore of major relevance.

Impulsive stimulated Raman scattering (IRSR) represents one well-established technique for the indirect coherent excitation of Raman active phonons by means of non-resonant excitations of the system with ultrashort broadband laser pulses. In this process, the electronic excitations transfer momentum to the lattice and launch oscillatory motions of Raman modes [34, 35, 36], as schematically shown in Fig. 1.3**(a)**.

A valid alternative to such high-energy excitation has been theoretically predicted already back in the 1970s [37, 38], and experimentally observed only recently [33]. This process is known as ionic Raman scattering (IRS). As schematically represented in Fig. 1.3**(b)**, the selective activation of coherent dynamics of Raman active phonons, relies on the intermediate excitation of infrared-active phonons [39, 38].

When mid-infrared light impinges onto a crystal lattice, oscillatory ionic motions are launched in a material along the eigenvector of the resonantly

(a)

(b)
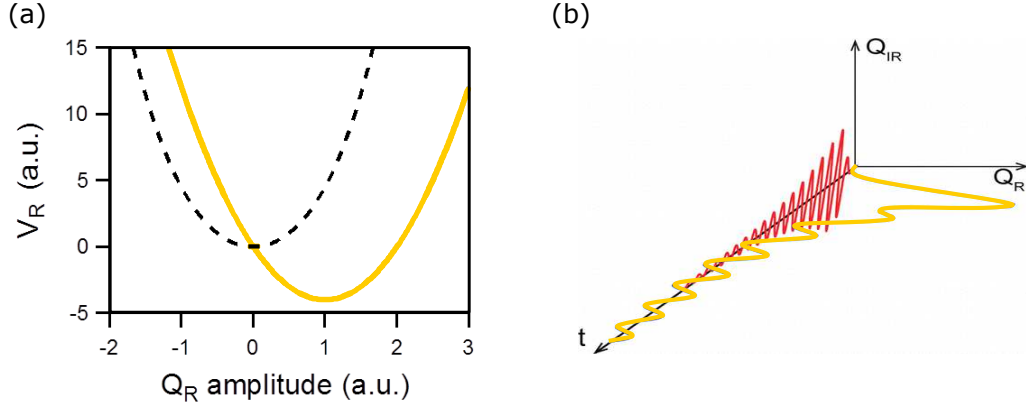
Figure 1.4: **(a)** Harmonic energy potential V_R of a Raman-active phonon mode unperturbed (black curve) and displaced (orange curve) for a finite static displacement of a coupled IR-active mode Q_{IR}. **(b)** Dynamics of the two coupled modes. While the ionic oscillation of the IR-mode happened around zero displacement(red curve), the anharmonically coupled Raman excitation happened around a displaced position (orange curve). If the optical excitation is fast compared to the Raman phonon period, coherent oscillations along Q_R take place [40, 41, 11].

excited vibration (red curve in Fig. 1.4**(b)**). If the displacement of the oscillating ions is big enough, an anharmonic coupling between the driven infrared-active mode and Raman-active modes can take place resulting in an effective non-zero displacement along the coupled mode eigenvectors. In this case, for MIR excitation shorter than the period of the coupled Raman mode, oscillations at the latter natural frequency will be observed, as schematically represented in Fig. 1.4**(b)**.

The crystal response to the optical excitation can be written in an Hamiltonian by considering two independent distinct contributions: a first linear term H_0 which describes the oscillatory motions around the equilibrium position of all the vibrating phonons, and a second anharmonic term H_{int}, which takes into account all the allowed nonlinear couplings among them [42].

The linear Hamiltonian holds for the kinetic and potential energy of the excited phonons and can be written as the sum of the directly excited infrared-

active modes and the anharmonically coupled oscillators, in the form

$$H_0 = \sum_{\mathbf{k}} \frac{1}{2}(P_{\mathbf{k},ir}^2 + \omega_{\mathbf{k},ir}^2 Q_{\mathbf{k},ir}^2) + \sum_{\mathbf{q}} \frac{1}{2}(P_{\mathbf{q},j}^2 + \omega_{\mathbf{q},j}^2 Q_{\mathbf{q},j}^2) - V(t) \qquad (1.1)$$

where $P_{\mathbf{k},ir}$, $\omega_{\mathbf{k},ir}$, $Q_{\mathbf{k},ir}$ and $P_{\mathbf{q},j}$, $\omega_{\mathbf{q},j}$, $Q_{\mathbf{q},j}$ are all possible momenta, eigen-frequencies and normal-mode coordinates of the activated infrared modes and the coupled ones respectively, while the potential $V(t)$ is the external potential.

Infrared light carries a momentum which is negligible with respect to the one of the lattice vibrations and thus accesses only optically active phonon with momentum of $\mathbf{k} \simeq 0$. On the contrary, this constrain doesn't hold for the anharmonically coupled phonons and excitations at finite momentum become possible.

In the case of a single resonant excitation of one infrared-active phonon at $\mathbf{k} = 0$, the interaction Hamiltonian accounting for the anharmonic coupling between the activated phonons can be written as

$$\begin{aligned}
H_{int} = \sum_{\mathbf{q}}(&a_{12}Q_{ir}Q_{\mathbf{q},j}^2 + a_{21}Q_{ir}^2 Q_{\mathbf{q},j} + a_{22}Q_{ir}^2 Q_{\mathbf{q},j}^2 + \\
&a_{13}Q_{ir}Q_{\mathbf{q},j}^3 + a_{31}Q_{ir}^3 Q_{\mathbf{q},j} + ...),
\end{aligned} \qquad (1.2)$$

where a_{nm} are the anharmonic coupling amplitudes. Among all the anharmonic terms of equation (1.2), only the one satisfying the selection rules from group theory will remain.

The simultaneous excitation of different infrared-active phonons can additionally lead to coherent dynamics in the material extending beyond the phononic coupling. In the rare earth orthoferrites ErF_3O_3, a coupling of two driven infrared-active modes to the magnetic order has been indeed observed, and coherent precession motions of the spins have been launched in the material [14].

In manganites as well as in most materials, the interaction Hamiltonian of Eq. (1.2) is dominated by the cubic interacting anharmonicity [32, 12] and

reduces to

$$H_{int} = \sum_{\mathbf{q}} (a_{12} Q_{ir} Q^2_{\mathbf{q},j} + a_{21} Q^2_{ir} Q_{\mathbf{q},j}). \qquad (1.3)$$

For centrosymmetric crystals, whose symmetry is held by the Hamiltonian, the first term in Eq. (1.3) vanishes being the infrared-active mode odd, and only the contributions of Raman modes (even) will be different from zero. For the indirect excitation of a single Raman mode the total Hamiltonian becomes

$$H_{tot} = \frac{1}{2}(P^2_{ir} + \omega^2_{ir} Q^2_{ir}) + \frac{1}{2}(P^2_R + \omega^2_R Q^2_R) + a_{21} Q^2_{ir} Q_R - V(t). \qquad (1.4)$$

Any finite static displacement dQ_{IR} reflects in a shift in the Raman mode's energy potential V_R along its coordinate Q_R, as depicted in Fig. 1.4(**a**). In the case of time-varying external perturbation $f(t)$, it is possible to retrieve the equations of motion for the infrared and the Raman modes as

$$\ddot{Q}_{ir} + 2\gamma_{IR}\dot{Q}_{ir} + \omega^2_{IR} Q_{ir} = 2a_{21} Q_{ir} Q_R + f(t) \qquad (1.5)$$

$$\ddot{Q}_R + 2\gamma_R \dot{Q}_R + \omega^2_R Q_R = a_{21} Q^2_{ir}, \qquad (1.6)$$

where $f(t) = A(t)\sin(\omega_{ir}t)$, with $A(t)$ being a Gaussian envelop, accounts for the driving electromagnetic pulse at frequency ω_{ir}, and the phenomenological damping terms, associated to the damping of the phonons (γ_{IR} and γ_R, infrared and Raman respectively) have been introduced in each equation.
Equations (1.5) describes the dynamic of the resonantly excited infrared mode in terms of a displacement of the eigenvector Q_{ir} around the equilibrium position. The time that the system takes to relax back to equilibrium is equal to the inverse of the damping term $\tau_{ir} = \frac{1}{\gamma_{ir}}$ which is usually around a few *ps*.
Equation (1.6) describes instead the temporal evolution of the anharmonically coupled Raman mode that is directionally driven by the term on the right side $F(t) = a_{21} Q^2_{ir}$. Since the driving oscillates at a frequency much higher with respect to the Raman vibration ($2\omega_{ir} \gg \omega_R$), the effective force acting on the coupled mode is proportional to the envelope of the squared

infrared coordinate. For optical excitations short compared to the Raman mode period, Q_R exhibits coherent oscillations, as shown in Fig. 1.4(**b**) (orange curve).

1.3   Electronic correlation modulation induced by light

As introduced in the previous section, intense THz pulses tuned at resonance with infrared-active modes can be used to create new transient crystal structures. These can emerge from the anharmonic coupling between the driven phonon and other modes.

This excitation scheme becomes more interesting for the case of molecular solids. In these systems light can address molecular vibrational modes and thus couple to local degrees of freedom. The excitation of low-energy modes associated to local distortions of the constituent molecules affects the size and shape of the molecular orbitals and can modify the on-site electronic interacting forces of the solid.

Organic molecular solids are generally characterised by sizeable electronic correlations, comparable with or even far larger than the electronic bandwidth, i.e. the electronic kinetic energy (see Chapter 2). Such energy competition is often responsible for Mott transition from the metallic phase. In most cases the physics of strongly correlated organic molecular solids is nicely captured by the Hubbard model, which is the simplest model of interacting particles in a lattice. This model accounts for two main contributions: one associated to the kinetic energy of the particles, and one potential term, accounting for the on-site correlations U, as explained more in details in the next paragraph.

Most of the molecular vibrational modes of complex molecular solids fall in the mid-infrared spectral region, and is therefore accessible to low-energy radiation. A first experiment of resonant excitation of an infrared active vibrational mode has been done on the quasi-1D organic Mott insulator ET-F$_2$TCNQ. This excitation allows a coherent control of the Hubbard U [16].
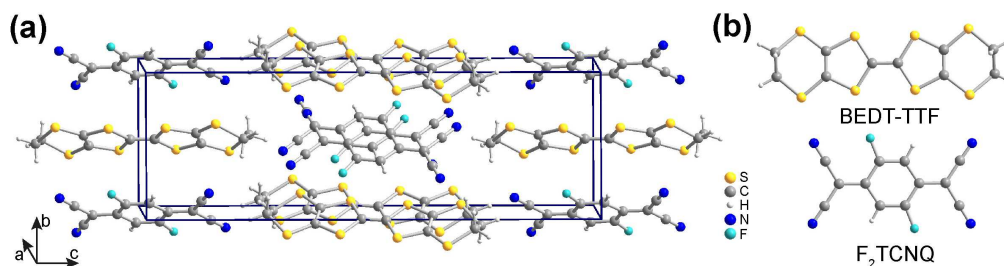
Figure 1.5: (a) Unit cell of the organic Mott insulator ET-F$_2$TCNQ formed by stacked molecules of BEDT-TTF (ET) and F$_2$TCNQ, which structure is displayed in (b) [15].

ET-F$_2$TCNQ is a molecular solid whose unit cell is formed by stacked molecules of BEDT-TTF (ET) and F$_2$TCNQ disposed as shown in Fig. 1.5. This system is a *charge-transfer complex* (see Chapter 2) held together by weak electrostatic attractions generated by the transfer of electronic charges from the donor to the acceptor. Due to the far larger *inter*molecular distances along the b- and c-axis, the molecular orbitals are only weakly overlapped along these directions and the effective macroscopic electrodynamic is only along the chains of ET molecules of adjacent unit cells, i.e. along the a-axis.

In spite of the partially filled conduction band, this material shows an insulating behaviour. This has been interpreted in terms of one-dimensional Mott physics along the ET chains, which are characterised by small intersite tunneling amplitude and large Coulomb repulsion [43].

The excitation by means of broad ultrashort MIR pulses tuned at $\omega_{ir} \sim 10$ μm has been shown to drive an optical response consistent with a time dependent deformation of the valence orbital wave function, and thus of the local charge densities. In particular, according to the extended Hubbard model introduced in more details in the next section, two distinct effects are expected from this type of excitation. First, a time-averaged reduction of the on-site repulsion, proportional to changes in the reflectivity $\Delta R/R$, and its modulation at twice the driving frequency. Both have been observed experimentally, as displayed in Fig. 1.6 [15, 16].

These experimental findings stand for a clear evidence of the possible light-induced control of the on-site molecular electronic properties. The theoretical
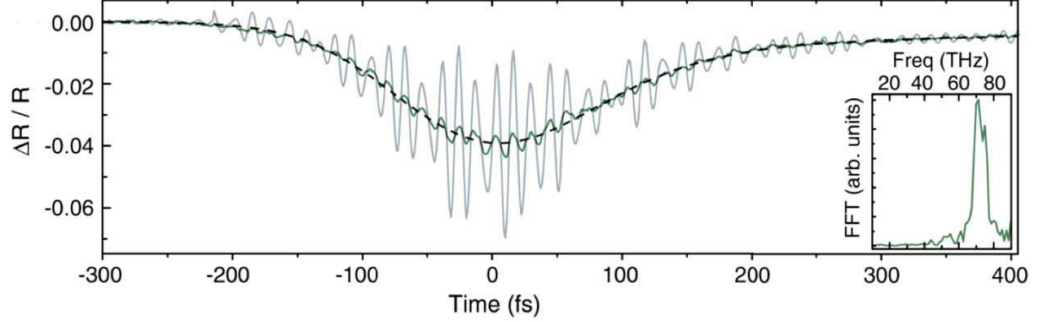
Figure 1.6: Spectrally integrated time-dependent reflectivity changes measured in ET-F$_2$TCNQ with a pump fluence of 0.9 mJ/cm^2 at room temperature. The deconvolved reflectivity changes (solid grey) is also displayed together with a double exponential fit (dashed black). The inset shows a Fourier transformation of the measured oscillations peaking at 70 THz [16].

formalism supporting the former observations will be briefly discussed in the next section.

1.3.1   Theoretical model for the modulation of the Hubbard U

Molecular organic solids represent an ideal system for light-control of matter, as they offer the possibility of coherent control of the local electronic degrees of freedom, via low-energy excitations. The electric properties of their ground states are determined by the molecular orbital conformation of the solid and the resonant excitation by means of infrared light of specific molecular vibrations can change local parameters, such as Mott correlations.

As mentioned in the previous section, the Hubbard model can be used to study the phenomena emerging in molecular solids. The extended Hubbard Hamiltonian holds as follows:

$$H_{Hub} = -t \sum_{l,\sigma} (c_{l\sigma}^{\dagger} c_{(l+1)\sigma} + h.c.) + U \sum_{l} n_{l\uparrow} n_{l\downarrow} + V \sum_{l} n_{l} n_{l+1}. \quad (1.7)$$

In this expression $c_{l\sigma}^{\dagger}$ and $c_{l\sigma}$ are creation and annihilation operators for an electron at site l with spin σ, $n_{l\sigma}$ is its corresponding number operator and $n_l = n_{l\uparrow} + n_{l\downarrow}$. The first term in Eq. (1.7) accounts for the electronic hopping among different sites of the lattice, whose amplitude t derives from the tight-binding model. U and V hold for the on-site and the nearest-neighbour-site Coulomb electronic repulsion respectively.

The total Hamiltonian of the vibrationally-driven state in which electronic correlations are modulated can be written as

$$H_{tot} \ = \ H_{Hub} \ + \ H_{int} \ + \ H_{ph}, \tag{1.8}$$

where H_{ph} accounts for all the activated molecular vibrational modes and H_{int} describes the interactions between the charge driven mode and the electronic configuration. Neglecting any nonlinear phonon coupling, the interaction term per each site j is expected to be a linear combination of the modulation of the electronic density n_j and of the double on-site occupancy $n_{j\uparrow}n_{j\downarrow}$:

$$H_{int,j} \ = \ n_j f(q_j) + n_{j\uparrow}n_{j\downarrow}g(q_j), \tag{1.9}$$

with $f(q_j)$ and $g(q_j)$ being general functions known a priori that depend on the displacement of the infrared mode coordinate q_j. By expanding those functions in series, the interacting Hamiltonian becomes

$$\begin{aligned} H_{int} \ = \ &\sum_j n_j (A_1 q_j + A_2 q_j^2 + A_3 q_j^3 + ...) + \\ &\sum_j n_{j\uparrow}n_{j\downarrow}(B_1 q_j + B_2 q_j^2 + B_3 q_j^3 + ...) \end{aligned} \tag{1.10}$$

with the coupling constants A_i and B_i depending on the symmetry of the molecular modes. In a centrosymmetric molecular solid, local infrared-active vibrations have an odd symmetry, and thus the terms linear in q_j, which would otherwise dominate the coupling for all even modes, vanish ($A_1 = B_1 = 0$).

For excitations at ω_{ir}, at resonance with the natural frequency of an infrared phonon, the quadratic dependence in q_j of the interaction Hamiltonian domi-

nates. Any modulation of the first term of Eq. (1.10), describing the coupling to the total electronic density n_j, will result in an overall shift of the whole energy of the system and hence it will not affect the electronic repulsion [16]. On the contrary, the second term, which refers to the coupling to the on-site double occupation, affects the effective Coulomb repulsion with a quadratic dependence to the phononic coordinate, and leads to modulation of U at twice the driving frequency ω_{ir}.

To the lowest order the interaction Hamiltonian reduces to:

$$H_{int} = B_2 q_j^2 n_{j\uparrow} n_{j\downarrow} \propto B_2[1 - cos(2\omega_{ir})]n_{j\uparrow}n_{j\downarrow} \qquad (1.11)$$

with the constant factor $B_2 < 0$, as a modulation of U leads, in most of the cases, to a spatial expansion of the valence orbital [16].

A more intuitive way to understand why the modulation of the electronic repulsion happens at $2\omega_{ir}$, is by considering the electronic density of the excited molecules oscillating around its equilibrium along the direction of the polarisation of the incident light. The molecule sloshes back and forth at frequency ω_{ir}, and this corresponds to a modification of the local molecular wavefunction at twice the frequency, as illustrated in the cartoon of Fig. 1.7 [16].

1.4   Light control of superconductivity

Low-energy excitations of atomic and molecular solids by means of electromagnetic radiation are capable of inducing transient out-of-equilibrium states. These can either result from structural distortion of the crystalline structure along indirectly excited vibrational modes, or, in molecular solids, from the coherent control of local degrees of freedom.

The experimental evidences reported so far, together with the newly developed theoretical tools, provide guidance for the further directions to take in the framework of light control of strongly correlated materials. Among the many interesting properties of complex solids [28], high temperature su-
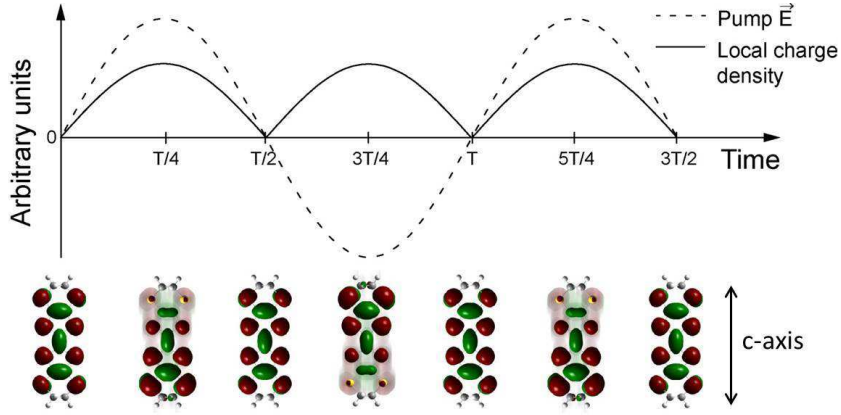
Figure 1.7: (upper panel) Temporal variation of the pump electric field (dashed black line), together with the resultant change in the local charge density (solid black line) and (lower panel) the corresponding orbital motion of vibrationally excited ET-F$_2$TCNQ molecule along the c-axis in time [16].

perconductivity is highly appealing especially when considering its possible functionality.

In the last five years, the effect of light on the superconducting ground state of the unconventional high-T_c cuprates superconductors has been investigated. The main question addressed in these studies is whether it is possible to understand how this phase settles among other competing orders and if it is possible to control it.

In the following paragraphs the resonant excitation of infrared active modes in the single-layer and double-layer cuprates will be discussed. Interestingly, signatures of out-of-equilibrium transient superconductivity were detected starting from the normal ground state at temperatures far higher than the equilibrium transition temperature.

1.4.1 Melting of charge stripes in single-layer cuprates

High-temperature superconductivity was firstly observed in 1980s in the layered copper oxides. These materials are formed by stack of conducting CuO$_2$ planes. The equilibrium superconducting temperature increases with the

number of Cu-O layers per unit cell and the highest T_c has been observed in trilayer compounds.

In the single-layer cuprates, conductivity originates by an excess of charge injected in the CuO_2 conducting planes by chemical doping. For the case of lanthanum copper oxides La_2CuO_4, conductivity arises by chemical substitution of the La atoms with Sr or Ba atoms of the form $La_{2-x}(Ba/Sr)_xCuO_4$, which leads to an unbalance of effective charge in the copper-oxide planes (hole doped). Three-dimensional superconductivity, among the different planes, has been observed for doping level $x > 0.05$, and the highest critical temperature ($T_c = 35$ K) has been detected for $x = 0.16$.

The $x = 1/8$ doping compound of the $La_{2-x}Ba_xCuO_4$ ($LBCO_{1/8}$) compound displays anomalies, as the three-dimensional superconducting phase is strongly suppressed by the presence of 1D charge and spin modulations along the planes. This order is stabilised by a structural transition from an high-temperature tetragonal (HTT), to the low-temperature tetragonal (LTT) phase, in which the angle of the oxygen atoms surrounding the Cu ion in the planes changes, as shown in the right inset of Fig. 1.8. At cold temperatures, the stripe modulations of adjacent planes are stabilised and adjacent layers become decoupled. This results in a complete frustration of the equilibrium three-dimensional superconducting phase.

This phenomenology is also characterising the equilibrium LTT phase of the $La_{1.8-x}Eu_{0.2}Sr_xCuO_4$ (LESCO) compound which exhibits striped spin- and charge-ordered states pinned to the underlying lattice distortions which completely destroy bulk superconductivity at all doping below $x = 0.125$ (grey and blue area respectively in Fig. 1.8) [44].

The resonant excitation of the Cu-O stretching mode in this compound transiently restores the coupling among superconducting layers, and hence three-dimensional superconductivity.

At equilibrium, bulk superconductivity in layered cuprates is reflected in the appearance of a so-called Josephson plasma resonance (JPR) in the c-axis THz optical properties. This feature accounts for the tunnelling between two adjacent superconducting CuO_2 planes, and is the hallmark of a three-dimensional superconducting state. In Fig. 1.9(a) the equilibrium c-axis
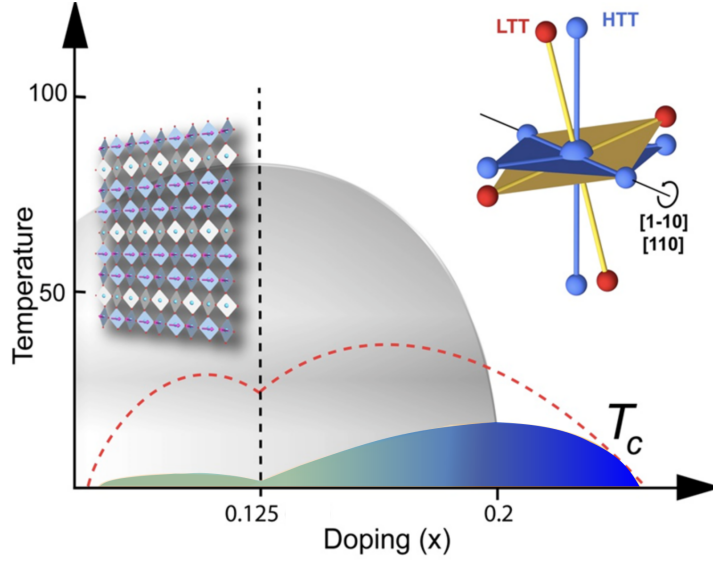
Figure 1.8: Schematic phase diagram for $La_{1.8-x}Eu_{0.2}Sr_xCuO_4$. Weak superconductivity (blue area) quenched by the stripe order phase (gray area) for doping levels below 0.2. At 0.125 doping ($x = 1/8$), a static striped state emerges in the CuO_2 planes (left inset), together with an LTT structural distortion (right inset). The red dashed curve marks the boundary for superconductivity in compounds of the type $La_{2-x}Sr_xCuO_4$, in which the LTT structural modulation is less pronounced. Figure adapted from [44].

reflectivity for the optimally doped parent compound $LSCO_{0.16}$ ($x = 0.16$, $T_C = 35$ K) is shown. While the metallic phase displays a featureless reflectivity coefficient r = E_{refl}/E_{inc}) in the THz frequency range (black dots), the equilibrium superconductor displays an edge and a dip in the reflectivity spectrum at the frequency corresponding to the Josephson plasma resonance between the layers (red dots).

The same feature in the reflectivity coefficient spectrum has been observed and fully formed 5 ps after resonant photoexcitation in $LESCO_{1/8}$, emerging at 10 K from the striped phase (Fig. 1.9**(b)-(c)**). This feature indicates the creation of a light-induced coherent transport in the c-axis across the different layers, quenched at equilibrium by the presence of stripes, and is accompanied by the prompt formation of superfluid density which accounts for a transient, three-dimensional superconducting phase [44].
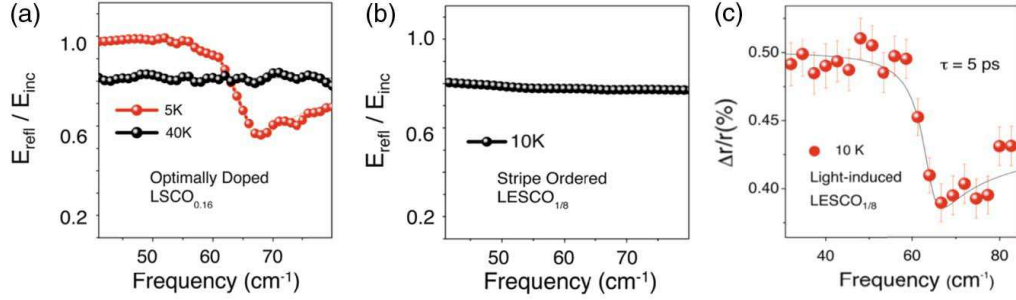
Figure 1.9: **(a)** Equilibrium c-axis reflectivity of $LSCO_{0.16}$ ($T_c = 35K$). In the superconducting state, the appearance of a JPR reflects coherent interlayer transport. Above T_c, incoherent ohmic transport is identified by a flat and featureless spectrum. **(b)** Equilibrium c-axis reflectivity of $LESCO_{1/8}$ at 10 K, showing the response of a non-superconducting compound. **(c)** Reflectivity changes induced in $LESCO_{1/8}$ by MIR excitation at 10 K, displaying a light-induced JPR [44].

Additional evidence of light-induced melting of the charge order has been observed on $LBCO_{1/8}$. The magnitude of the charge ordering peak, measured with soft x-ray scattering (SXR) at the Linac Coherent Light Source (LCLS), has been measured after the resonant excitation of the same Cu-O stretching mode. Figure 1.10**(a)** reports the abrupt reduction of the peak intensity by $\sim 60\%$ which stands for a transient weakening of the charge order, induced by means of electromagnetic radiation [45]. Importantly, the resonant mid-infrared excitation of $LBCO_{1/8}$ was found to affect also the diffraction peak associated to the LTT structure, accounted as responsible for the stabilisation of the stripes. Panel **(b)** of Fig. 1.10 reports the measured reduction of the intensity of such peak as a function of pump-probe delay, characterised by a much slower dynamic compared to the one of the stripe melting [45]. From the comparison of the temporal evolution and relaxation of the optical measurement on $LESCO_{1/8}$ and the x-ray scattering data of $LBCO_{1/8}$, it is possible to infer that there is a tight connection between the stripe order melting and the emergence of superconductivity, while the structural distortion seems to be less relevant in this system.
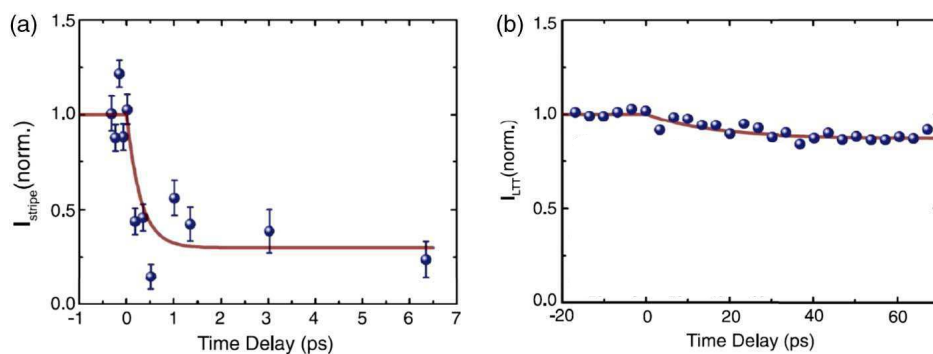
Figure 1.10: (**a**) Light-induced dynamic of the charge stripe order diffraction peak in $LBCO_{1/8}$. A prompt decease of about 60 % of the scattered intensity, characterised by a sub-ps temporal evolution is displayed by the blued circles. The red solid line is an exponential fit with a time constant of 300 fs, comparable to the resolution of the experiment. (**b**) Corresponding changes in the intensity of the diffraction peak associated to the LTT distortion in the same crystal under the same excitation conditions. The red solid line is an exponential fit yielding a time constant of 15 ps [45].

1.4.2 Light-induced superconductivity in double-layer cuprates

In light of the striking results of vibrational excitation on the single layered cuprates, an analogous excitation scheme has been used to drive the bilayer copper oxides $YBa_2Cu_3O_x$ (YBCO) out of equilibrium. The targeted infrared active mode, as explained later in this section, has been shown, upon resonant driving, to control the coherent transport of Cooper pairs between different planes and its excitation is expected to affect the superconducting properties of the system [17].

A representation of the crystalline unit cell of the $x = 6.5$ doped compound $YBCO_{6.5}$ is displayed in Fig. 1.11(**a**). Each cell is formed by two bilayers of stacked charged plains of CuO_2 separated by an insulating layer of yttrium ions. The space in the between of the two bilayers, the *inter*layer region, is instead occupied by barium atoms and CuO chains, of which the latter act as reservoir of charge for the bilayers. The distance of the "apical" oxygen atoms in the *inter*layer from the planes relates to the in-plane hopping and this affects T_c [46].
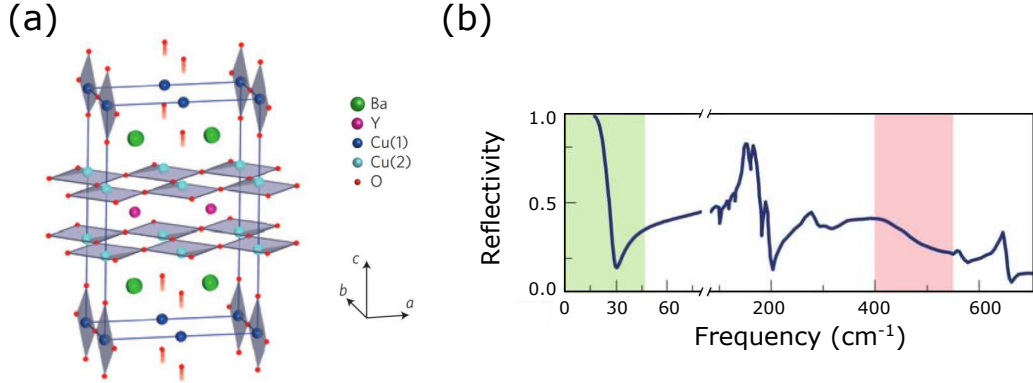
Figure 1.11: **(a)** Structure of YBCO$_{6.5}$ and cartoon of the optically driven distortion for the apical oxygen. The bilayer is formed by the two plains of CuO$_2$ (Cu(2) in the legend) separated by the Y atoms. The intrabilayer space is filled by Ba atoms and the CuO$_4$ diamonds (Cu(1), and O in the *bc*-plane). The vibrational excitation displaces the apical oxygen atoms along the *c* direction. **(b)** Optical reflectivity spectrum at equilibrium measured along the *c*-axis of superconducting YBCO$_{6.5}$ ($T < T_c$). The low frequency JPR (green area) corresponds to the tunneling of electrons between the bilayers, while the high frequency feature (highlighted in red), identifies the intralayer resonance [17].

As already introduced in the previous section, the signature of the three-dimentional superconductivity in layered cuprates is the longitudinal Josephson plasma resonance (JPR) between the different conducting layers, which appears clearly in the optical reflectivity spectrum of the material. In Fig. 1.11**(b)** the optical reflectivity of the superconducting YBCO$_{6.5}$ ($T < T_c$, $T_c = 50$ K) is reported over a broad spectral region. The low frequency portion of the spectrum (green shaded area) is dominated by a sharp JPR at ~ 1 THz, related to the *inter*bilayer tunneling of the electrons. At higher frequencies (red area) another resonance can be identified, relative to the *intra*bilayer coupling (~ 15 THz) [17].

Single crystals of YBCO$_{6.5}$ were excited with sub-picosecond pulses tuned at resonance with an oscillatory eigenfrequency of the apical oxygen ions as schematically illustrated in Fig. 1.11**(a)**. When the system is driven from the superconducting state ($T < T_C$), its optical response is compatible to the one of a superconductor with a transient enhancement of the superfluid density.

This has been attributed to a strengthened coupling within the *inter*bilayer, at the expense of that within the bilayers. In agreement with what found below T_c for photoexcitations at temperatures above the critical transition temperature ($T = 60$ K $> T_C$), the low-frequency superconducting resonance is restored and has been measured up to room temperature [17, 47].

Due to the complexity of the physics of bilayer copper oxides, the interpretation of the out-of-equilibrium light-induced superconducting signatures is not straightforward. The different temporal evolution of the transient state found in $YBCO_{6.5}$ with respect to the one of the single-layer $LESCO_{1/8}$, together with the different temperature at which this effect is observed seems to exclude the hypothesis that the melting of the charge order is the only playing factor.

Hard x-ray diffraction data were taken for further investigation, under the same experimental conditions on $YBCO_{6.5}$ [18]. Once the system is resonantly driven, a sizeable reshape of the scattered intensity peaks of the four anharmonically coupled mode has been observed. The transiently distorted structure, displayed in Fig. 1.12, has been reconstructed from a careful analysis and fit of the light-induced changes in the scattered peaks. In the new out-of-equilibrium structure, obtained under resonant excitation at MIR frequency, is it moreover possible to observe an increase of the *intra*bilayer distance together with a reduction of the *inter*bilayer one.

Importantly, the four reshaped coupled peaks are the ones allowed by symmetry by the thoery of nonlinear phononics (see Section 1.2.1), and stand as clear evidence of anharmonic coupling amongst phonons in ordered solids [18].

Additionally, density functional theory calculations proposed a charge transfer between the CuO_2 planes and the CuO chains as possible phenomenon assisting the onset of the observed transient superconducting-like state at high temperature. This charge redistribution is already of relevance in three-dimensional superconductivity of $YBCO_{6.9}$ at equilibruim [48], where it accompanies the temperature driven metal-superconductor transition and might thus be beneficial for superconductivity.
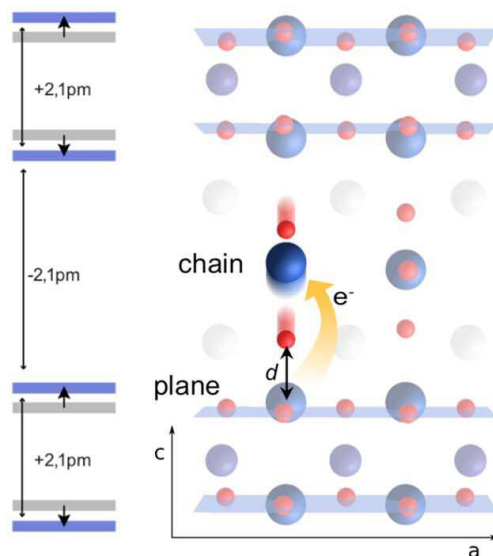
Figure 1.12: Schematic out-of-equilibrium structure of $YBCO_{6.5}$, reconstructed from fits of the transient scattered intensity of several peaks measured with Hard X-rays. The atomic displacements from the equilibrium structure involve a decrease in *inter*bilayer distance, accompanied by an increase in *intra*bilayer distance [18, 40].

1.5   Summary

Electromagnetic radiation couples to matter and constitute a very powerful tool that can be exploited to extend the current knowledge of many complex materials. Resonant excitations by means of low energy photons of collective modes in ordered structures can be used to dynamically drive systems out of equilibrium and favour the formation and stabilisation of new hidden phases. In this chapter some of the more relevant experimental observations of control of matter have been provided for the peculiar case of strongly correlated material, which exhibit interesting functional properties and are extremely sensitive to external perturbation. Copper oxides systems are unconventional high temperature superconductors and their phase diagram is the result of an intricate intertwine of different competing phases.

Mid infrared light has first been used to selectively activate phononic oscillations in the layered cuprates LBCO, for which superconductivity has been

restored transiently by melting the competing stripe order. Similar results have been later on obtained on the double layered cuprate YBCO, for which superconducting features have been detected for few picoseconds up to room temperature.

In light of these successful results, this type of low-energy excitation can be extended also to other materials. The current findings on the high-T_c cuprates superconductors are calling for the investigation of more conventional systems, where equilibrium superconductivity is understood.

In this thesis the response of a completely different class or material will be discussed. Alkali doped fullerides represent a valid candidate for vibrational investigation as they are molecular solids whose electronic response is strongly entangled to the molecular distortions. Moreover these materials shows a more conventional superconducting phase emerging at relatively high critical temperatures, unlike other molecular systems.

As vibrational excitation in organic molecular materials proved that light can modulate the on-site electronic interacting force, as described earlier in the chapter, the study of molecular superconductors could in principle offer new insights on the origin of high temperature superconductivity.

CHAPTER 2

The organic superconductor K_3C_{60}

Organic molecular solids are constituted by periodic arrangements of relatively small molecules, mostly resulting by chemical bonding of light atoms (e.g. C, H, N,...). In spite of their complex structures, there exist a clear energy scale differentiation between the *intra*- and *inter*molecular degrees of freedom that simplifies the physical interpretation of their properties.

Due to the relatively large *inter*molecular distances, the electronic structure of molecular solids is usually characterised by well separated narrow bands, reflecting the confinement of the populating electrons. The small hopping integral makes electronic correlations relevant and often leads to a localisation of the carriers with the consequent emergence of Mott-Hubbard insulating phases.

Among all the organic conductors, alkali doped fullerides A_3C_{60} are the only ones characterised by three-dimensional conducting properties. Despite the strong electronic repulsive interactions, these materials exhibit a common superconducting phase below relatively high critical temperatures.

This chapter will briefly recall the most relevant traits of organic molecular conductors and will specifically discuss the case of the alkali doped fullerides. In Section 2.2, the properties of the metallic and superconducting phase of

A_3C_{60} are described.

2.1   Organic molecular conductors

Organic molecular solids are formed by an ordered and periodic disposition of different molecules held together by weak interacting forces, e.g. Van der Waals forces. Their unit cells typically comprehend several weakly bounded molecules, therefore extend over a few nanometres, i.e. orders of magnitude more than the average extension of orbitals of the constituent atoms. The final crystalline structures of organic molecular solids are characterised by a sparsely-populated, narrow, electronic band structure.

In the same way as in an oriented molecular gas, individual molecules in molecular solids remain unaltered and their vibrational frequencies differ only slightly from the those of the free molecules [21]. These local molecular vibration energies generally occupy the high-frequency part of the excitation spectrum of the crystalline solid (see Fig. 2.1) and are characterised by little dispersion in momentum space. The lower frequency part of the excitation spectrum of molecular solids is instead dominated by the *inter*molecular vibrations, or phonons, which are of essential importance for energy and charge transport across the solid. *Inter*molecular vibrations have frequencies usually below 3 THz (~ 100 cm^{-1}), far lower than those of atomic solids, and include optical phonons, librations and translational vibrations [21].

Organic molecular crystals are soft, with small bulk moduli, and fairly high thermal expansion coefficients, of the order of 10^{-5} K^{-1} [49, 50]. Any variation of the crystal volume, i.e. of the lattice constants, induced by a change of the temperature or by means of external pressure will strongly affect the frequencies of the *inter*molecular phonons, while no relevant changes are expected in the *intra*molecular ones. In the case of thermal expansion at warmer temperatures, for example, the larger lattice constant results in smaller frequencies of the *inter*molecular modes, while no significant changes are expected on the local vibrations.

Organic molecular solids have been firstly regarded as electrical insulator, but at a later time, a richer variety of ground states has been found under
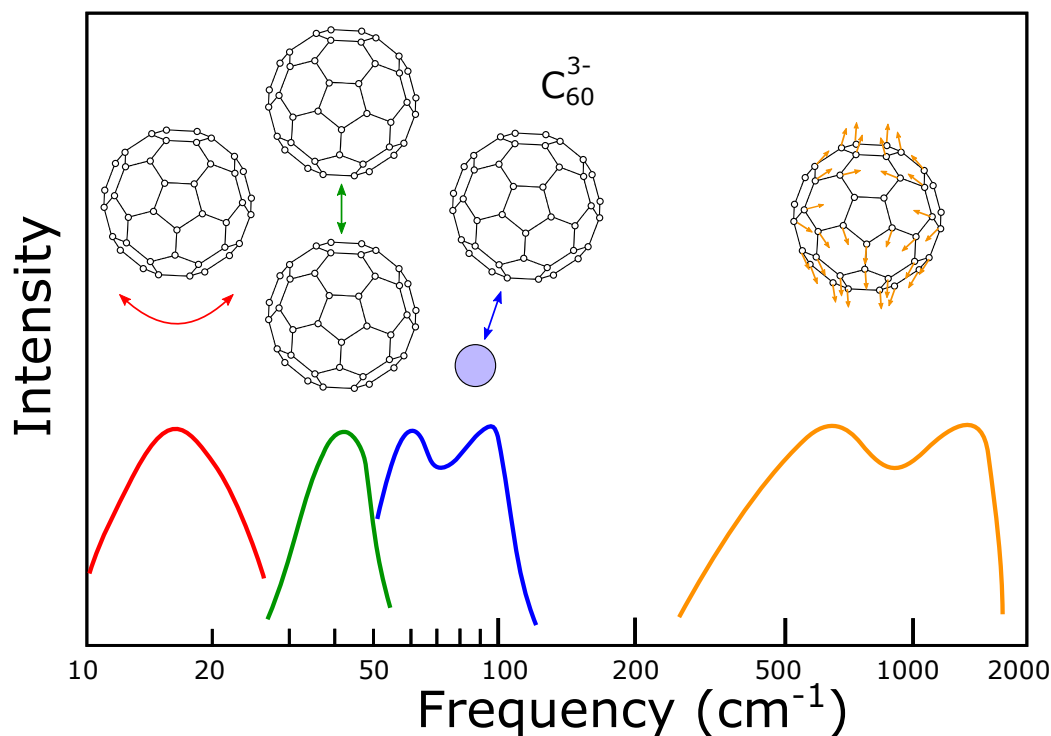
Figure 2.1: Schematic representation of the vibrational spectrum of the three-dimensional alkali-doped fullerines (A_3C_{60}). The high-frequency broad absorption is ascribable to *intra*molecular vibrations (orange), while at low-frequencies *inter*molecular dynamics dominate: librations (red), $C_{60}-C_{60}$ optical phonons (green) and $A-C_{60}$ phonons. The associated distortion of the lattice are schematically displayed. Figure adapted from [21].

different external conditions [51, 52, 53]. Most of the macroscopic physical properties of the organic molecular solids are primarily determined by electrons weakly participating in the bonding of the constituent molecules. These dominant electrons, known as π-electrons, are delocalised along the molecular planes and therefore are responsible to the final conducting properties of the solid.

In molecular solids it is possible to distinguish among the electrons localised within the nearest carbon atoms in the σ-bond, and those that can participate in the conductivity through the π-bonds, as schematically represented for a benzene molecule in Fig. 2.2.

The lowest electronic excitation states in organic molecular solids are often
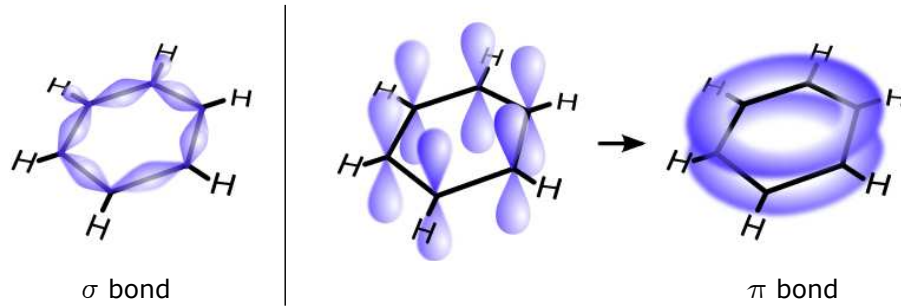
Figure 2.2: Molecular orbitals representation of a benzene molecule C_6H_6. The σ-bond on the left results from the $sp2$ hybrid orbitals of the molecule while the π-bond on the right is formed by the different π_z orbitals of the carbon atoms and provide a delocalised charge cloud distribution along the molecular planes. Figure adapted from [55].

the ones of the π-electrons, which usually respond to energies in the range of a few eV [49]. By studying the behaviour of the π-electrons, which depends on the nuclei, the inner-shell electrons and with the σ-electrons, most of the electronic and chemical properties of organic conductors can be described [53, 49, 54].

A crucial aspect of organic molecular solids is the presence of strong Coulomb interactions that correlate the electronic motion. As the electronic correlations win over the electronic kinetic energy, metals with a partially filled conduction band can become Mott-insulators.

The extended Hubbard model is generally used to describe organic strongly correlated systems and their proximity to the Mott transition, as already introduced in Chapter 1. This model assumes two main counteracting contributions to the total energy of the system: electronic hopping integral t, and electronic repulsion due to other charges on the specific site, U, and between different sites of the lattice, V (See Eq. 1.7). In the case of strong screening, and in half-filled systems, the repulsive contribution due to the nearest neighbours V can be neglected.

The effective electron-electron interaction are typically comparable to the width of the conduction band, around 0.5-1 eV. In the Hubbard model, electronic interactions are therefore measured in comparison to the bandwidth
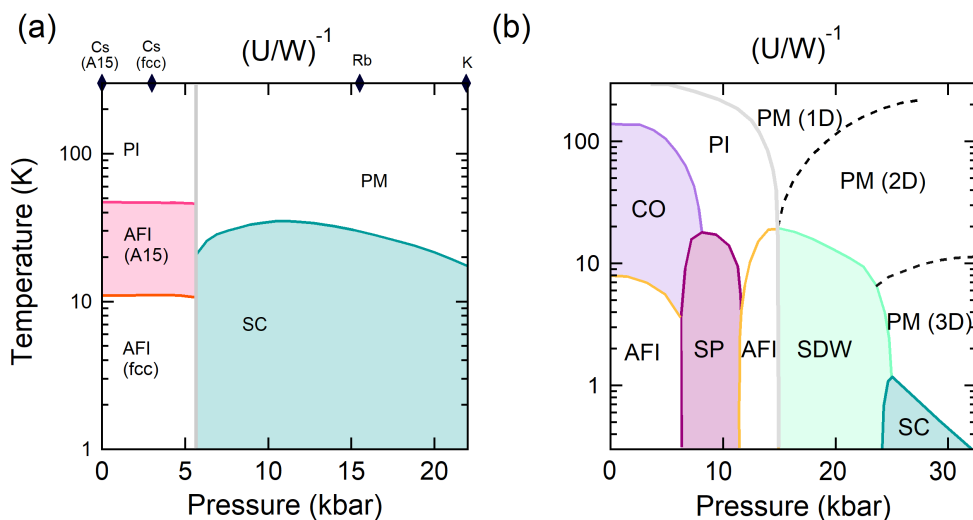
Figure 2.3: Temperature-Pressure phase diagrams for two families of organic molecular solids with different effective dimensionality. **(a)** The three-dimensional alkali fullerides family A_3C_{60} with the black diamonds on the upper axis identifying the equilibrium position of different alkali dopant (adapted from [58]). **(b)** The one-dimentional Bechgaard salts $(TMTTF)_2X$ (or $(TMTSF)_2X$) (adapted from [52]). The variety of ground states scales with the dimensionality. In the plots the following abbreviations have been made: paramagnetic insulator (PI), paramagnetic metal (PM), antiferromagnetic insulator (AFI), superconductor (SC), charge order (CO), spin Peierls insulator (SP) and spin density wave (SDW).

W (defined as $W = zt$, where t is the hopping integral and z depends on the dimensionality of the system) and they are expressed as U/W.

In half-filled systems, within the limit of $U/W = 0$, i.e. $U = 0$, the Hubbard model reduces to the Hartree-Fock description of a Fermi gas, while for $t = 0$ it describes the behaviour of an ideal Mott-insulators [56]. At intermediate U/W values, the competition between hopping transport and Coulomb repulsion leads to mixed ground states within the metal-to-insulator transition (MIT). In most organic materials, insulating phases are stabilised above a critical U/W_c value of about 1-1.5 [21] and the conduction electrons become localised in the fully filled lower Hubbard band [56, 57].

The interplay of molecular condensation, narrow bands, strong correlations, and softness results in an extreme variability of ground states in organic ma-

terials. Figure 2.3 displays phase diagrams of the quasi-1D and 3D organic conductors (panels **(b)** and **(a)** respectively). In both systems a multitude of ground states emerges upon chemical substitution or by means of external pressure, and this is particularly stressed the lower is the dimensionality of the system [59, 60].

Pressure can be translated in terms of intrinsic parameters of the system, as U/W ratio. The more correlated is the system, the more one moves towards the left side of the diagrams, where insulating phases stabilise (paramagnetic (PI) or antiferromagnetic (AFI)). On the contrary, for smaller unit cell the hopping of the electrons generally prevails over the electronic correlations and one moves to the right side of the phase diagrams.

Among all the possible organic conductors, the *donor-acceptor complex* systems constitute a large class. Such charge-transfer complexes are formed by two different molecules which are held together by an exchange of charges from the donor to the acceptor. The effective intermolecular transfer of electrons together with the *inter*molecular coupling defines the number of free carriers available for the metallic conduction.

The most interesting ground state of conducting organic materials is on the other hand, the superconducting one (SC), found even in the low dimensionality systems (see Fig. 2.3). Alkali doped fullerides A_3C_{60}, as discussed in the rest of the chapter, are three-dimensional conductors characterised by bulk superconductivity with relatively high critical temperatures, from 20 K to ~ 40 K, which is only partially explained in terms of conventional BCS superconductivity.

2.2 The alkali-doped fullerides

Alkali-doped fullerides (A_3C_{60}, A = K, Rb, Cs) are organic molecular conductors, whose electronic properties are determined by the excess of charge injected in the system by the alkali atoms. Each C_{60} molecule contains 60 carbon atoms arranged with single or double covalent bonds in 20 hexagonal and 12 pentagonal faces to form a 7 $\mathring{A}$ diameter cage (the soccer ball). This structure belongs to the highly symmetric I_h symmetry point group and its
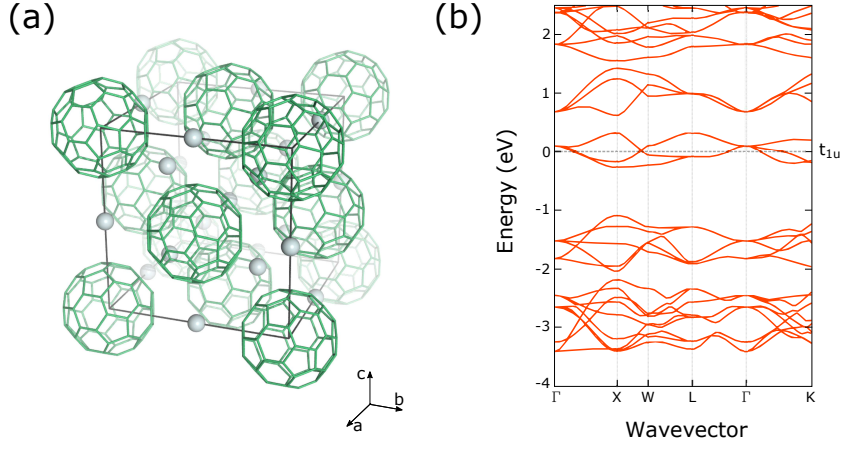
Figure 2.4: **(a)** Cubic unit cell of K_3C_{60}. The C_{60} molecules (green) are arranged in an f.c.c. cell (lattice constant of 14.24 $\mathring{A}$ at room temperature) and the alkali dopant (light grey spheres) occupy the free interstitial spaces. **(b)** Band structure of potassium doped fullerides K_3C_{60} characterised by well separated narrow bands [23].

electronic band structure is highly degenerate.

Alkali-doped fullerides crystallise in a cubic unit cell, in which the C_{60} molecules are arranged in a f.c.c. fashion for A=K, Rb and in a b.c.c. (or A15) or f.c.c. one for Cs_3C_{60}. The alkali atoms (light grey spheres in Fig. 2.4**(a)**) occupy the interstitial volumes. The size of the chosen alkali atoms defines the lattice constant d of the unit cell that varies from 14.24 $\mathring{A}$ for K_3C_{60} to 14.75 $\mathring{A}$ for Cs_3C_{60} at room temperature.

Each C_{60}^{3-} molecule - the acceptor - receives three electrons from three surrounding alkali atoms A^+ - the donors. The resulting ground state of the solid is characterised by an half-filled conduction band t_{1u}, triply-degenerate at the Γ point (Fig. 2.4**(b)**). Electronic correlations in A_3C_{60} are fairly strong, and are comparable to the bandwidth of the conduction molecular orbital ($U/W \sim 1.5 - 2.5$) [21]. While potassium and rubidium fullerides (K_3C_{60}, Rb_3C_{60}) still show a metallic behaviour, the expanded compound Cs_3C_{60}, characterised by narrower bands, is a Mott-insulator [61, 62].

The phase-diagram of the family of alkali-doped fullerides A_3C_{60} is displayed in Fig. 2.3**(a)**. Potassium doped fullerides K_3C_{60} is the most compact compound and sits at the very right side of the diagram. The increase of the

unit cell obtained by alkali atom substitution leads to narrower bands due to a lower overlap of the molecular orbitals. Beyond a critical volume, the electron-electron Coulomb repulsion energy (U) prevails over the electronic kinetic energy (t) and the metal-to-insulator transition takes place. The expanded Cs_3C_{60} at ambient pressure is in fact an insulator ($U \sim 1$ eV, $W \sim 0.5$ eV [21]).

As it will be discussed in the next paragraph, a superconducting phase (SC) emerges from the paramagnetic metallic phase (PM) in K_3C_{60} and Rb_3C_{60} at ambient pressure and in Cs_3C_{60} under pressure characterised by unconventionally high critical temperatures, compared to other organic superconductors [63].

2.2.1   Superconductivity in A_3C_{60}

Superconductivity is a common phase of all A_3C_{60} compounds. Unlike conventional BCS superconductors, the transition temperature T_c does not scale linearly with the lattice spacing or pressure, but it follows more the characteristic dome-shape of the high-temperature superconductors, as reported in Fig. 2.3(**a**). The critical transition temperature T_c increases from ~ 20 K to ~ 30 K only by substituting the potassium alkali atom with the rubidium one, and has a maximum in Cs_3C_{60} under pressure ($T_c = 38$ K and $T_c = 35$ K respectively for the A15 and f.c.c. compounds at $P \simeq 1$ GPa). The high critical temperature values are ascribable to the high electronic density at the Fermi energy [64].

The least correlated compounds of the family of A_3C_{60} can be fairly well described as a type-II superconductor by means of standard BCS theory and the relevant excitation for the pairing mechanism are associated to high frequency *intra*molecular phonon modes [65, 66]. The strong correlations responsible for the Mott-insulating phase of Cs_3C_{60}, on the other hand, are also likely to influence its superconducting state, and a more sophisticated theoretical description of superconductivity is required [67].

Figure 2.5(**a**) reports the measured relation between the superconducting critical temperature and the lattice parameter in all the A_3C_{60}. As long as

the lattice constant remain below a 14.5 Å, i.e. for K_3C_{60} and Rb_3C_{60}, a linear relation, with a small sublinear correction fits the experimental trend. This is in good agreement with standard BCS predictions. On the other hand, a strong deviation can be observed in the values of T_c obtained in Cs_3C_{60} under pressure [67]. Interestingly, a reduction of the lattice constant by means of external pressure brings all the A_3C_{60} compounds to the same curve [68, 69]. Further evidence of the anomalous superconducting phase of A_3C_{60} systems comes from the measurement of the superconductivity gap Δ. By means of NMR and photoemission experiments, a strong deviation from the BCS predicted value of the gap ratio $2\Delta_0/k_BT_c = 3.52$ nearby the metal-insulator transition has been observed. Figure 2.5(**b**) displays the experimental measurements of the gap ratio in Cs_3C_{60} under different values of external hydrostatic pressure, i.e. lattice constant. At ambient pressure, at the right side of the plot, the gap ratio of Cs_3C_{60} deviates from the conventional BCS value (grey dashed line). In the compressed system, i.e. for smaller lattice constants, the gap ratio converges to more standard values, and it reaches 3.4 and 4.1 for a unit cell size comparable to the one of K_3C_{60} and Rb_3C_{60} respectively [70, 61]. A guide to eye (yellow solid line) has been also plotted to capture the trend of the gap ratio as a function of lattice parameter.

The limits of the BCS theory in describing the relation of the gap, the critical temperature and lattice constant when electronic correlations become dominant, stresses the need of a more sophisticated formalism for an universal understanding of superconductivity in the phase diagram of the alkali doped fullerides A_3C_{60}.

Importantly, alkali doped fullerides do not strictly satisfy the weak-coupling approximation $N(E_F)V_{eff} \ll 1$ required in the standard theory, where $N(E_F)$ is the electronic density of states at the Fermi level and V_{eff} is the interaction potential of the electrons mediated by the electron-phonon coupling. In most classic superconductor $N(E_F)V_{eff} < 0.3$ [71]. The strong electronic correlations of A_3C_{60} compounds influence this factor, which in K_3C_{60} stays at the limit of validity of the BCS theory (~ 0.3,), and in Cs_3C_{60} becomes even higher than the unity [72, 73].

A theory of strongly correlated superconductivity (SCS) has been first pro-
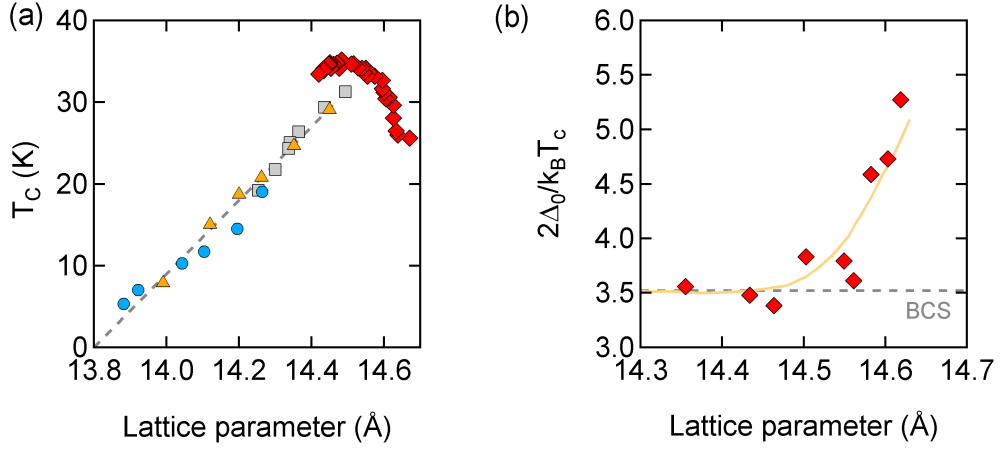
Figure 2.5: **(a)** T_c vs lattice parameter for different samples of A_3C_{60}. Red squares are NMR data measured in f.c.c. Cs_3C_{60} at different external pressure values, yellow triangles and light blue circles are indicated the critical temperature scaling with the lattice parameter for Rb_3C_{60} and K_3C_{60} respectively, while the grey squares refer to the mixed A_3C_{60}. The latter data points are obtained from magnetisation studies [67, 68, 69]. The grey dashed line is the linear BCS expected trend relation between T_c and the lattice constant. **(b)** Dependence of the superconducting gap divided by the superconducting critical temperature, $2\Delta_0/k_BT_c$ of f.c.c Cs_3C_{60} under pressure plotted as a function of lattice parameter, measured with the spin-lattice relaxation rate of ^{13}C in the superconducting state [61]. The solid thick line is a guide to the eye, while the dashed grey line marks the BCS value predicted value of 3.52.

posed by Capone et al.[74, 75]. In alkali doped fullerides, the electronic t_{1u} band is half-populated and the coupling to molecular vibrations is of major relevance. The modes allowed by symmetry to couple to t_{1u} electrons are only A_g and H_g modes.

At equilibrium, a dynamical structural Jahn-Teller distortion of H_g symmetry acts on the C_{60} molecules to lift the degeneracy of the electronic conduction band, minimising the molecular energy. This distortion strongly affects the electronic coupling and stabilises the formation of a low spin and angular momentum ground state [74]. The resulting electronic singlet state, i.e. electron pairs with same momentum, can occupy any of the three degenerate orbitals, and the third electron of the conduction band occupies one of the other two.
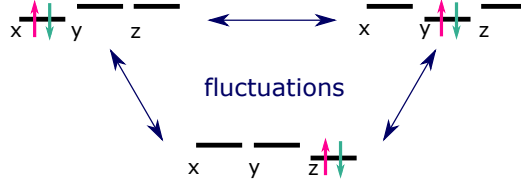
Figure 2.6: Ground-state orbital fluctuations promoting the emergence of the superconducting phase in A_3C_{60}. Data adapted from [77].

More recently, a unified theory for the equilibrium superconductivity in A_3C_{60} disentangled the crucial ingredients needed to describe to the proximity of superconducting and Mott-insulating phases in the same phase diagram [76], lacking in the simple BCS picture.

The key quantity needed to capture the macroscopic properties of A_3C_{60} given their non-negligible electronic contribution is the effective exchange interaction J, that can be defined as the sum of the intramolecular exchange interaction J_H and the one due to the electron-phonon coupling J_{ph}, as $J = J_H + J_{ph}$ [74, 76]. According to the Hund's rule, a high spin state should be stabilised, with parallel-spin electrons sitting on different molecular orbitals, as the bare J_H contribution is positive. On the other hand, the interaction contribution due to the Jahn-Teller distortion $J_{ph} < 0$ would promote the formation of a low spin state. The effective exchange interaction is hence renormalised and, as $J_{ph} > J_H$, the Hund's rule is reversed [74]. This leads to the formation of bound electrons into *intra*orbital pairs which support the superconducting coupling.

Importantly, the electron pairs are delocalised over the three orbitals by means of *intra*molecular pair-hopping (see Fig 2.6), promoting hence three-dimensional superconductivity [77]. Eventually, in the Mott-insulating phase, the pairs stay localised in one of the molecular orbital [74, 76].

To conclude, alkali doped fullerides A_3C_{60} are type-II superconductors characterised by relatively low first critical magnetic field $H_{c1}(0)$ in the range of 10 mT, and a fairly large second critical field $H_{c2}(0)$ of about 30-80 T. The corresponding coherence lengths ξ calculated by means of the Ginzburg-Landau formalism is very small (few tens of nanometers) comparable to the one of other unconventional high-Tc superconductors [78].

2.3   Summary

This chapter provided an overview of the equilibrium properties of the organic molecular conductors, in particular of the three-dimensional alkali doped fullerides A_3C_{60}. The crystalline structure of such solids are poorly dense, and responsible for the formation of narrow electronic bands. The strong correlation of the conduction electrons together with their energy confinement are responsible for the emergence of Mott-insulating ground states. In spite of the half-filled conduction band, the most expanded fullerides Cs_3C_{60} are in fact insulating at ambient pressure, while Rb_3C_{60} and K_3C_{60} are metallic.

An unconventional dome-shaped superconducting phase with fairly high critical transition temperature has been found in the phase diagram of the A_3C_{60}, emerging at cool temperature from the metallic phase. The coexistence of the superconducting and the Mott-insulating phase in the same diagram has been recently captured by means of ab initio calculations. The strongly correlated superconducting phase has been explained in terms of electron-phonon coupling among the conduction electrons and a molecular Jahn-Teller T_{1u} distortion of the C_{60} molecules, while its crossover to the insulating phase has been attributed to the strong interacting forces among electrons. These are indeed responsible for the renormalisation of their kinetic energy leading to charge localisations.

As introduced in Chapter 1, light can be used to drive instabilities in complex correlated systems, leading to the emergence of broken symmetry states. The resonant excitation by means of infrared radiation of *intra*molecular vibrations in K_3C_{60} is expected to perturb the *on-site* molecular properties which are determining its electronic ground state. Before proceeding to the experimental evidences of such vibrational excitation in these compounds, the next chapter will describe its optical linear response.

CHAPTER 3

Equilibrium optical properties of potassium doped fullerides

An ideal tool to investigate solid state electrodynamics is the analysis of their optical properties. *Intra*band and *inter*band transitions are mostly determining the ground state electronic properties of a system and it is possible to identify them by looking at their shapes in the optical spectra.

The most profound description of a medium is given by the complex dielectric constant $\epsilon = \epsilon_1 + i\epsilon_2$ which is a microscopic response function accounting for its electric polarisation. From this quantity, all optical properties can be recalculated. In non-magnetic media (magnetic permeability $\mu = 1$) the same information can be retrieved from the macroscopic observable, the complex refractive index $N = n + ik$ [79].

In the spectroscopic study of materials, practical response functions for condensed matter are the frequency dependent optical reflectivity $R(\omega)$ and complex optical conductivity $\sigma(\omega) = \sigma_1(\omega) + i\sigma_2(\omega)$. The conductivity $\sigma(\omega)$ is defined as the response function of the material to an applied electric field as

$$\mathbf{J} = \sigma \mathbf{E} \tag{3.1}$$

with $\mathbf{J}$ being the current density induced in the medium and $\mathbf{E}$ an external electric field [79]. This quantity becomes of relevance when dealing with low-energy spectroscopic investigations as it is directly reflecting the electrodynamic properties of the systems.

In this chapter the equilibrium optical response of K_3C_{60} single crystal available in literature is first described in order to introduce the main differences between its metallic and superconducting response. Later, in the main part of the chapter, the same optical response is presented for the case of K_3C_{60} powders which have been used in the experiments described in the next chapters. A full infrared characterisation of the response of these samples is then presented as a function of temperature and pressure.

3.1 Optical response of K_3C_{60} single crystal

Metals and superconductors display unique and distinctive hallmarks in their optical spectra ($R(\omega)$ and complex $\sigma(\omega)$), which can be used to discriminate these two ground states. The optical properties of potassium-doped fullerides have been measured on single crystals [70] and on pressurised powder samples [23]. In spite of few quantitative discordances in the far-infrared response which will be discussed later in the chapter, the different datasets are in fairly good agreement with each other.

Figure 3.1 displays the optical reflectivity, the real and the imaginary part of the optical conductivity of K_3C_{60} in its metallic (orange lines) and superconducting phase (light blue lines), measured on a single crystal [70]. The normal state reflectivity ($T = 25$ K), plotted at the sample-diamond interface for convenience, displays the characteristic feature of the free electrons in the conduction band, captured by the Drude model, with a plasma edge located at approximately 300 meV (panel (a)). This contribution appears clearly in the complex optical conductivity spectra: in the real part $\sigma_1(\omega)$ as a wide Lorentzian centred at zero frequency, and in the imaginary part $\sigma_2(\omega)$ as peak at the scattering rate γ around 7.5 meV . On top of the free carriers response, higher energy absorptions characterise the optical spectra. In particular a strong infrared absorption band appears as a Lorentzian peak
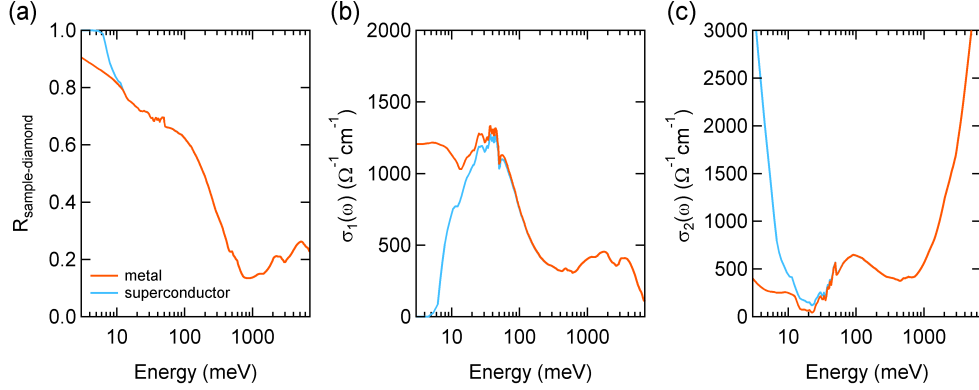
Figure 3.1: Equilibrium optical response of single crystal K$_3$C$_{60}$ above and below T_c (orange and light blue respectively): optical reflectivity at the sample-diamond interface (**(a)**), real and imaginary part of the optical conductivity (**(b),(c)**). Data below T_c are measured at 10 K while the one above T_c are measured at 25 K [70] .

in the real conductivity spectrum and is centred around 50-100 meV. At even higher energies the optical spectra of metallic K$_3$C$_{60}$ are shaped by the contributions of interband electronic transitions [70].

The real part of the optical conductivity $\sigma_1(\omega)$ obeys to the sum rule:

$$\int_0^\infty \sigma_1(\omega)d\omega = \frac{\pi N e^2}{2m} \tag{3.2}$$

where N is the total number of electrons participating in the absorptions, e is the electronic charge and m is their mass. The total spectral weight, defined as the area under the real conductivity spectrum, is thus proportional to the ratio of the electronic density and the mass of the electrons, which is a constant.

The optical reflectivity and conductivity spectra of the superconducting state in potassium-doped fullerides are also plotted in Fig. 3.1 (light blue curves). Optical measurements allow observing the superconducting gap of K$_3$C$_{60}$, due to its isotropy in the momentum space. A fairly strong reshape affects the optical response across the superconducting phase transition. The reflectivity at the sample-diamond interface of superconducting K$_3$C$_{60}$ saturates to unity ($R(\omega) = 1$) up to the optical gap frequency $2\Delta = 6$ meV (panel **(a)**).

(a)

(b)
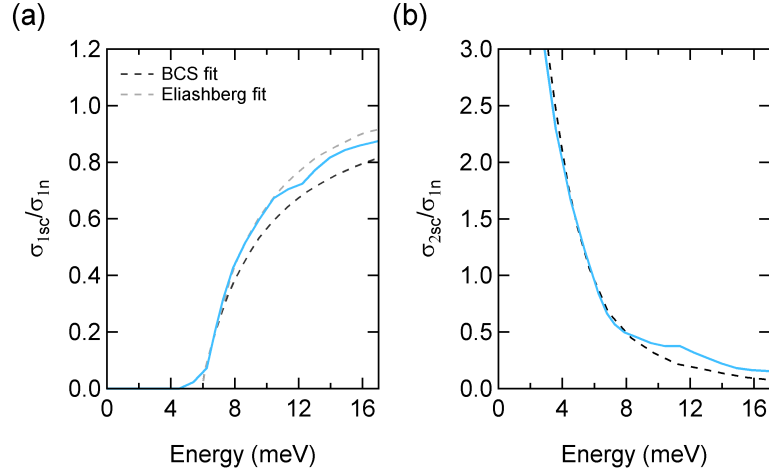
Figure 3.2: Real **(a)** and imaginary part **(b)** of the conductivity spectrum of a superconducting single crystal of K_3C_{60} at 10 K normalised to the real normal conductivity σ_{1n}. The ratio σ_{1sc}/σ_{1n} describes the response of the normal carrier, while σ_{2sc}/σ_{1n} accounts for the coherent response of the superconductor. The black and grey dashed lines are fit respectively for the weak and strong coupling limit. Data adapted from [70].

In accordance, most of the spectral weight in the real part of the optical conductivity is moved to a delta peak at zero frequency and an optical gap opens up to the same cut-off frequency (panel **(b)**). The low-energy spectrum of the imaginary conductivity is instead dominated by an hyperbolic $1/\omega$ divergence scaling with the superfluid density (panel **(c)**).

Since the overall spectral weight in $\sigma_1(\omega)$ is conserved, it is possible to divide the contribution of the superconducting carriers to the one of the normal state by rewriting Eq. 3.2 as

$$\int_0^\infty \sigma_1(\omega)d\omega = \frac{\pi}{2}\frac{N_s e^2}{m} + \frac{\pi(N - N_s)e^2}{2m} \tag{3.3}$$

where N_s is the total number of carriers participating to superconductivity held in the integral of the Delta peak at zero frequency which accounts for the infinite conductivity.

The available Matthis-Bardeen models for BCS superconductors, and the Eliashberg extension for the strong coupling limit, capture the superconducting optical response as a function of frequency and temperature, by

considering only the free carriers contribution. According to these models, only delocalised carriers participate in the superconducting transition.

To remove the contribution of bound carriers, the normalised quantities σ_{1sc}/σ_{1n} and σ_{2sc}/σ_{1n} are defined. Figure 3.2 displays the reduced gap values obtained for single crystal K$_3$C$_{60}$. The normalised real part of the optical conductivity (panel **(a)**), expresses the response of the normal carriers in the superconducting phase [79]. From this plot, the opening of the superconducting optical gap appears clearly. The black dashed line is the result of a conventional Matthis-Bardeen fit of the experimental data, that fails at high energies. The more general Eliashberg model (light gray dashed curve) on the other hand nicely captures the measured trend, highlighting the proximity of K$_3$C$_{60}$ to the strong coupling limit (electron-phonon coupling $\lambda_{e-ph} \sim 1$) [72, 70]. Independently on the model used, the phase transition from the metallic to the superconducting state in K$_3$C$_{60}$ is accompanied by changes in the optical properties only in the lower part of the spectrum, within $\sim 6\Delta$. The normalised imaginary part of the complex conductivity (Fig. 3.2**(b)**) is instead associated to the response of the condensed carriers [79]. Below the optical gap the $1/\omega$ divergence dominates over the other contributions, and it can be capture just by means of the standard BCS model (dark dashed line) [70].

3.2 Optical spectra of K$_3$C$_{60}$ powders

The experimental investigation reported in the next chapters has been performed on K$_3$C$_{60}$ powders. A full characterisation of their equilibrium optical response has been done in order to be able to compare these samples with the ones described in literature. The equilibrium optical response of the metallic polycrystalline K$_3$C$_{60}$ has been measured on compressed powder pellets (100-400 nm average grain size, see Appendix A) by means of a broadband FTIR interferometer at Elettra Synchrotron Facility.

To prevent the sample from any oxygen contamination, the K$_3$C$_{60}$ powders were loaded in pure Argon atmosphere inside a glove box (oxygen level

$< 1ppm$) and sealed behind a diamond window (see Appendix A).

The sample reflectivity spectra were measured in a cryostat at temperatures spanning from 25 K to 300 K. Each spectrum on the sample has been referenced at each temperature to the one of the diamond as commonly done in far infrared interferometric measurement under pressure [80, 81, 82]. The final absolute values of the reflectivity at the sample-diamond interface were obtained by rescaling these ratios with the ones of a gold mirror put in a later time at the sample position ($R_{sample-diamond} = I_{sample}/I_{diamond} \cdot I_{diamond}/I_{gold}$, see Appendix B).

The reflectivity raw curves, ranging from 4 to 1000 meV, were extrapolated to zero frequency below 4 meV by means of the Hagen-Ruben formula valid for $\omega \ll 1/\tau$

$$R(\omega) = 1 - \left(\frac{2\omega}{2\pi\sigma_{DC}}\right)^{\alpha}, \tag{3.4}$$

with $\alpha = 0.385$ to guarantee a smooth connection. At very high frequency, the single crystal reflectivity data were used to extend the spectrum up to 6 eV. By means of Kramers-Kronig transformations for medium against a transparent window [83], broadband complex conductivity spectra were retrieved. The free parameter β accounting for the phase shift contribution of the transparent diamond window, was such to obtain a Kramers-Kronig consistent fit of all the optical properties simultaneously ($\beta = 217$ meV).

The superconducting optical spectra below T_c were retrieved in a later time by means of another FTIR apparatus and a cryostat which allowed for a more efficient cooling of the sample. Broad spectra reflected from the sample below its critical temperature were measured from 8 to 19 K from 3 to ~ 90 meV and referenced to the ones acquired at 25 K, just above T_c. As in the case of a single crystal, major changes of the optical properties affect only the low part of the spectrum and above 40 meV the spectra above and below T_c are identical. The broad spectra at the sample-diamond interface below T_c were finally obtained by multiplying the measured ratio with the broad absolute reflectivity curve at 25 K as $R^{8K}_{sample-diamond} = R^{8K}_{3-90meV}/R^{25K}_{3-90meV} \cdot R^{25K}_{sample-diamond}$.

The optical reflectivity and conductivity spectra across the superconducting phase transition of powders of K_3C_{60} are displayed in Fig. 3.3 for temper-
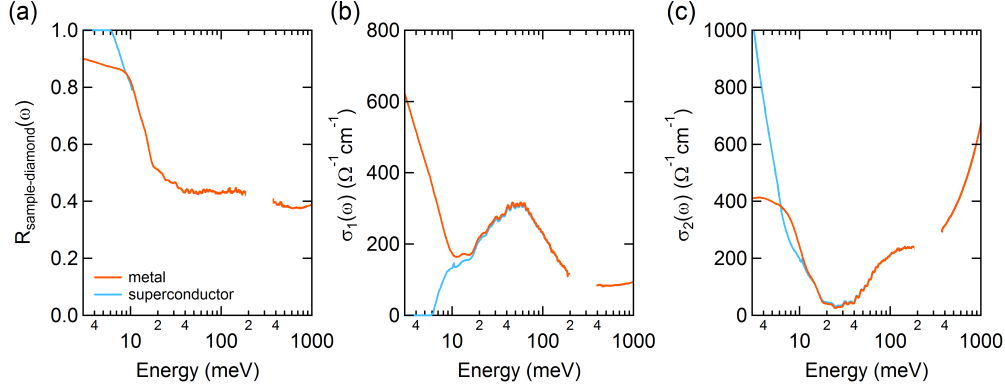
Figure 3.3: Equilibrium optical response of powders of K$_3$C$_{60}$ above and below T_c (orange and light blue respectively): optical reflectivity at the sample-diamond interface **(a)**, real and imaginary part of the optical conductivity **(b,c)**. Data below T_c are measured at 10 K while the one above T_c are measured at 25 K. The blank region in the plot is the diamond absorption window [23].

atures of 8 K and 25 K. As in the single crystal, the low energy spectra of metallic K$_3$C$_{60}$ is occupied by a Drude component on top of an additional absorption. However, from a simultaneous Drude-Lorentz fit of $R(\omega), \sigma_1(\omega)$ and $\sigma_2(\omega)$ below 150 meV, it emerges that in the powder sample both the contributions are less pronounced, and the plasma frequencies of the Drude and the polaronic band together result smaller. As a consequence, the extrapolated DC value of the real part of the optical conductivity of the metallic K$_3$C$_{60}$ is reduced from $\sigma_{DC} \sim 1500~\Omega^{-1}cm^{-1}$ in single crystal to $\sigma_{DC} \sim 1000~\Omega^{-1}cm^{-1}$ in powders. A possible explanation of the different optical properties and electrodynamics of the powder with respect to the single crystal relies on the grain boundaries which could prevent some free carriers from participating in the conduction. The joint observation of a reduced scattering rate in the powder (γ = 3-4 meV) possibly support this interpretation, being the effective electronic density smaller and hence less likely to scatter [23].

The superconducting optical reflectivity and real conductivity σ_1 exhibit the edge at the value of the optical gap which is in agreement with the one previously observed ($2\Delta(T=0) \simeq 6$ meV), while the reduced divergence of the imaginary part of the conductivity with respect to the monocrystal accounts,
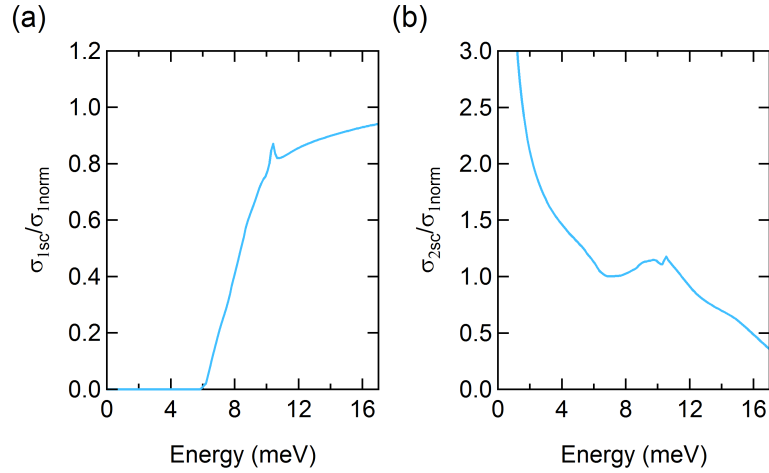
Figure 3.4: Real **(a)** and imaginary part **(b)** of the conductivity spectrum of superconducting powders of K_3C_{60} at 10 K normalised to the real normal conductivity σ_{1n} . The ratio σ_{1sc}/σ_{1n} describes the response of the normal carrier, while σ_{2sc}/σ_{1n} accounts for the coherent response of the superconductor.

once more, for a smaller number of available superconducting carriers.

The normalised real and imaginary part of the optical conductivity are finally plotted in Fig. 3.4 for a more complete description of the superconducting state. While σ_{1sc}/σ_{1n} highlights once more the optical gap size and the region where the optical curves below T_c merges with the one above (panel **(a)**), the ratio σ_{2sc}/σ_{1n} shows the characteristic $1/\omega$ divergence below the 6 meV gap with the onset of a pronounced feature around 10 meV (panel **(b)**). This is likely to be a contribution of localised carriers not participating to superconductivity in the low energy spectra, probably due to some polaronic effect. Even if studies of this feature are lacking in literature, it is interesting to note that the same feature is visible also in the single crystal data with less spectral weight compared to the powder sample.

Temperature dependence

Metallic K_3C_{60} does not show a strong temperature dependence in its optical reflectivity and complex conductivity. Figure 3.5 displays the optical response of the powder sample for different temperatures ranging from 25

Figure 3.5: Temperature dependence of the optical reflectivity **(a)**, real and imaginary part of the complex conductivity **(b,c)** of polycrystalline K$_3$C$_{60}$ above its critical temperature. The blank region in the plot is the diamond absorption window [23].

K (right above the T_c) up to room temperature. The blank regions of the plots are the absorption window of the diamond used for the measurement. Reflectivity and complex optical conductivity spectra for each temperature have been simultaneously fitted below 150 meV using a Drude-Lorentz model, which includes a free-carrier term (i.e., Drude) centred at zero frequency and a Lorentz oscillator at $\omega_{0,osc} = 50\text{-}100$ meV, which accounts for the polaronic absorption [70], of the form

$$\sigma_1(\omega) + i\sigma_2(\omega) = \frac{\omega_{Dp}^2}{4\pi}\frac{1}{\gamma_D - i\omega} + \frac{\omega_{p,osc}^2}{4\pi}\frac{\omega}{i(\omega_{p,osc}^2 - \omega^2) + \gamma_{osc}\omega}. \tag{3.5}$$

Here ω_{Dp} and γ_D are the Drude plasma frequency and scattering rate, while $\omega_{p,osc}$, $\omega_{0,osc}$ and γ_{osc} stand for the oscillator strength, the resonant frequency and the damping coefficient of the Lorentz term. The results of a Kramers-Kronig consistent fit run on all the optical properties together are displayed in Table 3.1.

While no distinctive differences can be appreciated from the reflectivity curves alone, clearer changes affect the complex optical conductivity spectra. The zero frequency component of the real part of the conductivity σ_0, defined as $\omega_{Dp}^2\tau/4\pi$, is extracted from the fit at all temperatures, and does not show a strong temperature dependence. The 50-100 meV absorption

T (K)	σ_0 ($\Omega^{-1}cm^{-1}$)	ω_{Dp} (meV)	γ_D (meV)	$\omega_{0,osc}$ (meV)	$\omega_{p,osc}$ (meV)	γ_{osc} (meV)
25	998 ± 20	179 ± 1	4.32 ± 0.05	47.9 ± 0.3	491 ± 3	98 ± 1
100	1009 ± 20	160 ± 1	3.40 ± 0.06	54.6 ± 0.6	516 ± 6	136 ± 3
200	1369 ± 30	167 ± 1	2.74 ± 0.04	49.6 ± 0.6	513 ± 6	120 ± 3
300	1125 ± 30	159 ± 1	3.03 ± 0.05	58.1 ± 0.7	499 ± 7	136 ± 4

Table 3.1: Drude-Lorentz fit parameters of optical properties of polycrystalline K_3C_{60} at ambient pressure at various temperatures above T_c. The plasma frequency and the scattering rate for the Drude are listed as ω_{Dp} and γ_D respectively, and are used to recalculate the zero frequency values of the conductivity σ_0. The mid-infrared absorption peak has been fitted by an oscillator characterised by the central frequency $\omega_{0,osc}$, its strength $\omega_{p,osc}$ and by a damping γ_{osc}.

band is instead more reshaped by the changing temperature and it evolves in $\sigma_1(\omega)$ from a single-Lorentzian-like peak at 25 K to a double-structured-one at room temperature.

The temperature dependence of the optical properties of superconducting K_3C_{60} is plotted in Fig. 3.6. At the lowest temperature of 10 K the optical reflectivity is saturated ($R(\omega) = 1$) below the optical gap energy, the superconducting gap in the real conductivity spectrum $\sigma_1(\omega)$ is fully formed and the $\sigma_2(\omega)$ spectrum strongly diverges at low energy. For higher temperatures all those features get gradually smeared, and the state is described by a flat but not saturated reflectivity, a not fully depleted gap in $\sigma_1(\omega)$ and a less pronounced divergence in $\sigma_2(\omega)$.

The dependence of the normalised sigmas with increasing temperature is plotted in Fig. 3.7. The ratio σ_{1sc}/σ_{1n} (panel **(a)**) shows the gradual filling of the superconducting gap which strikingly does not happen with the BCS predicted scaling of the optical gap energy. On the contrary, the gap size stays around 6 meV also for temperature as high as $\sim T_c$ and more spectral weight populates the depleted areas uniformly. The same unconventional behaviour of the superconducting gap is observed in optical measurements on single crystals [70]. The temperature dependence of the σ_{2sc}/σ_{1n} ratio is plotted in Fig. 3.7**(b)**. The sharp $1/\omega$ divergence found at 10 K is gradually damped by the contribution of the high frequency oscillator and progressively a sharper peak centred at 10 meV takes form.
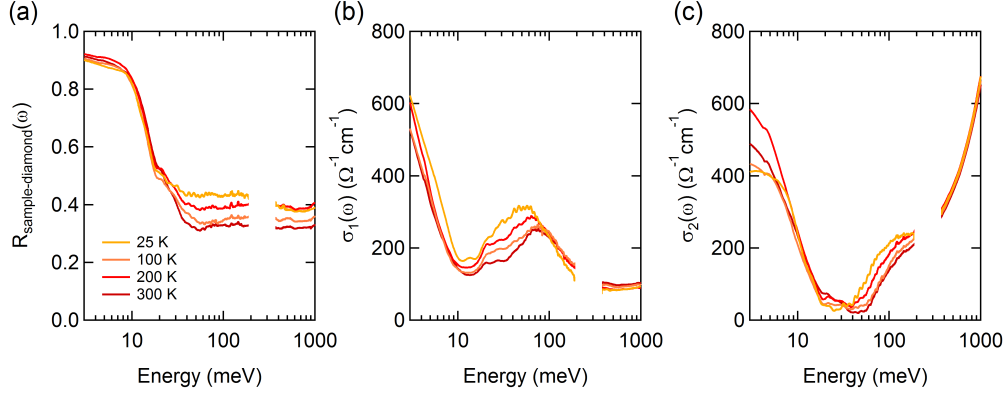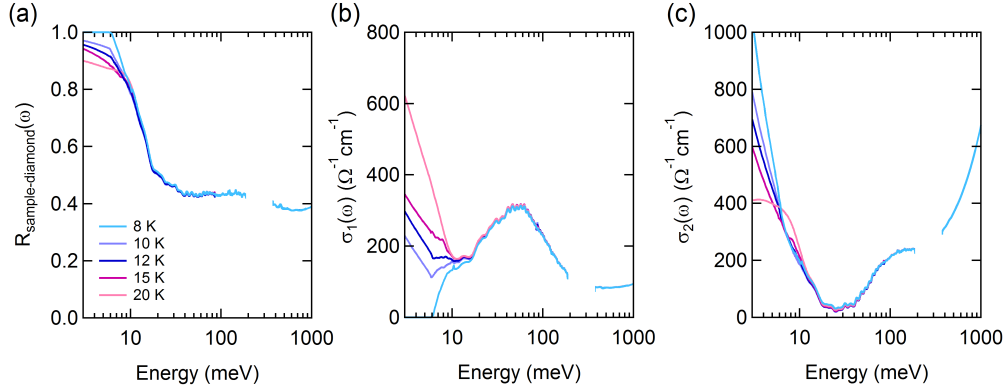
Figure 3.6: Temperature dependence of the optical reflectivity (**(a)**), real and imaginary part of the complex conductivity (**b,c**) of polycrystalline K$_3$C$_{60}$ below its critical temperature. The blank region in the plot is the diamond absorption window.

Pressure dependence

The optical properties of the normal state of powders of potassium-doped fullerides have been acquired also under hydrostatic external pressure at several temperatures. Hydrostatic pressure was applied by a screw-driven opposing plate diamond anvil cell (DAC) using Boehler-Almax type IIac diamond anvils with a culet size of 2 mm. A 250 μm thick Cu foil was pre-indented down to $\sim 100\mu$m and a hole of ~ 1 mm of diameter was drilled by means of an electro microDriller from Almax Easylab as sample compartment (see Appendix B).

Polycrystalline K$_3$C$_{60}$ powders (100-400 nm average grain size, see Appendix A) were used to fill the hole without any hydrostatic medium, being itself a powder, and a few particles of ruby were added for the determination of pressure. This setup allows achieving hydrostatic pressure values as high as 3.5 GPa, which were accurately measured *in situ* using a ruby fluorescence manometer [84, 85] (see Appendix D). The DAC was mounted on the cold finger of a liquid helium cryostat, which allowed varying the sample temperature to study the pressure dependence at all the temperature above T_c previously measured ($T = 30$ K, 100 K, 200 K and 300 K).

The equilibrium reflectivity of K$_3$C$_{60}$ was measured at the sample-diamond
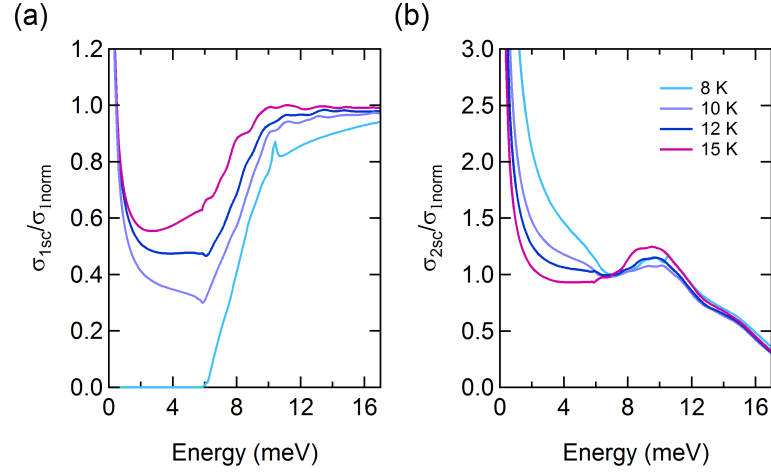
Figure 3.7: Temperature dependence of the real **(a)** and imaginary part **(b)** of the conductivity spectrum of superconducting powders of K_3C_{60} normalised to the real normal conductivity σ_{1n}.

interface by referencing against a gold mirror placed into the same holder at the sample position. The experimental curves were then extrapolated at low frequency (< 5 meV) using Drude-Lorentz fits, while for high frequencies (> 500 meV) literature data on K_3C_{60} single crystals [66] were used. Kramers-Kronig transformations have been performed for samples in contact with a transparent window [83], and the complex optical conductivity of K_3C_{60} at all temperatures and pressures has been reconstructed. Figure 3.8 displays the equilibrium optical properties of powder K_3C_{60} measured for different pressures for all the measured temperatures. The same Drude-Lorentz model of Eq. 3.5 has been used to fit the low energy optical reflectivity and complex conductivity spectra simultaneously (below 130 meV). The results are reported in Table 3.2. The extrapolated values of the zero frequency conductivity σ_0 monotonously increases for higher pressure values, as expected from a metal in which external hydrostatic pressure broadens the bandwidth at fixed number of carriers. No defined trend is observed instead for the high-frequency absorption band at 50-100 meV.

By comparing the optical properties of powder K_3C_{60} under pressure with the ones at ambient pressure, it is possible to observe a discordance in the free-carriers parameters. A double plasma frequency ω_{Dp} and scattering rate

Figure 3.8: Pressure dependence of the optical reflectivity (right), real and imaginary part of the complex conductivity (middle and right) of polycrystalline K$_3$C$_{60}$ above its critical temperature (30 K panel (**a**), 100 K panel (**b**), 200 K panel (**c**) and 300 K panel (**d**)). The blank region in the plot is the diamond absorption window.

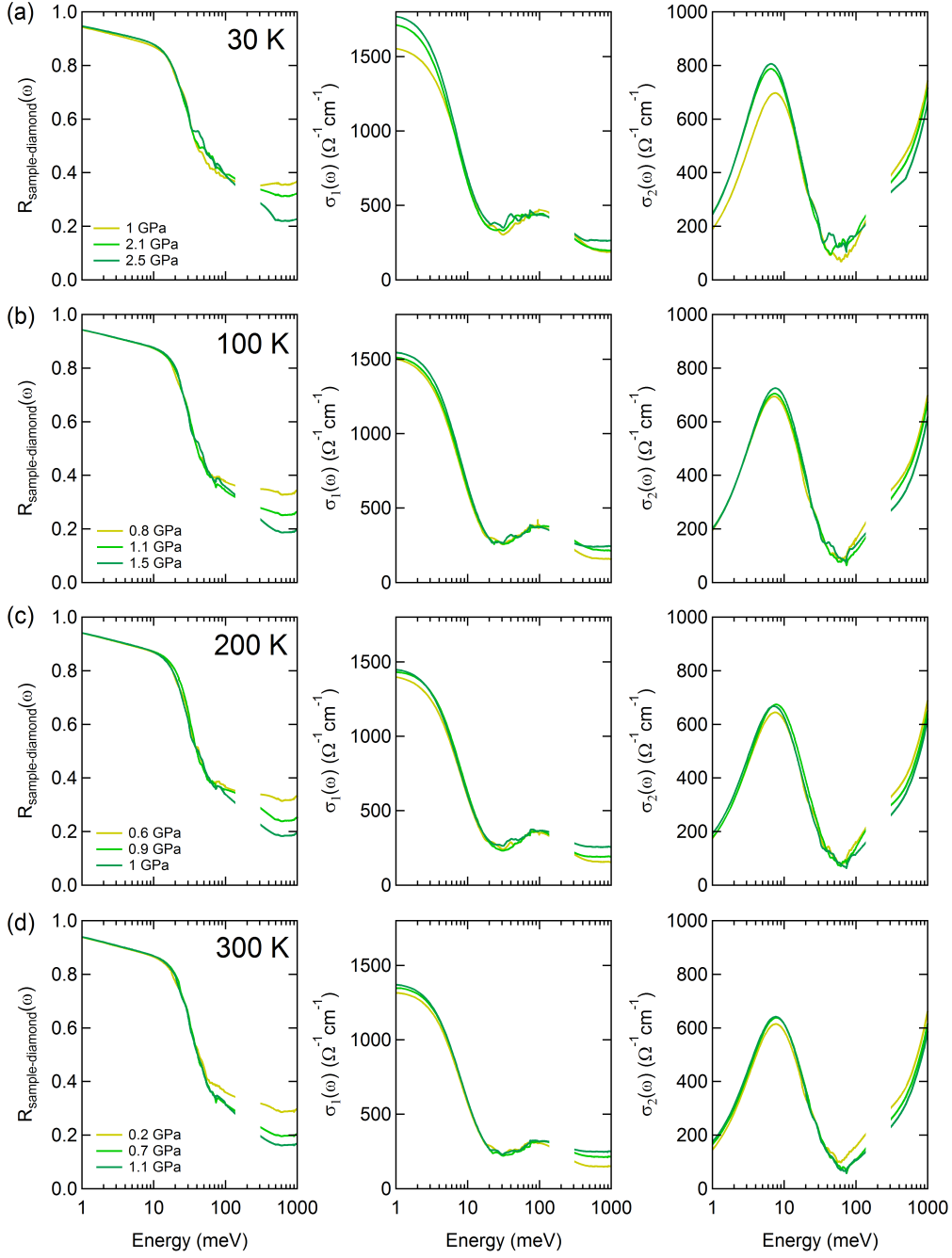| T (K)	P (GPa)	σ_0 ($\Omega^{-1}cm^{-1}$)	ω_{Dp} (meV)	γ_D (meV)	$\omega_{0,osc}$ (meV)	$\omega_{p,osc}$ (meV)	γ_{osc} (meV)
30	1 ± 0.1	1572 ± 20	314 ± 1	8.4 ± 0.1	85.5 ± 0.8	784 ± 10	201 ± 5
30	2.1 ± 0.1	1752 ± 30	310 ± 1	7.4 ± 0.1	76.2 ± 0.9	795 ± 10	216 ± 6
30	2.5 ± 0.1	1811 ± 30	317 ± 1	7.5 ± 0.1	83 ± 1	942 ± 13	271 ± 8

T (K)	P (GPa)	σ_0 ($\Omega^{-1}cm^{-1}$)	ω_{Dp} (meV)	γ_D (meV)	$\omega_{0,osc}$ (meV)	$\omega_{p,osc}$ (meV)	γ_{osc} (meV)
100	0.8 ± 0.1	1520 ± 20	300.2 ± 0.7	8.0 ± 0.1	75.9 ± 0.6	604.0 ± 8	160 ± 4
100	1.1 ± 0.1	1540 ± 20	307 ± 1	8.2 ± 0.1	81 ± 1	633 ± 10	190 ± 6
100	1.5 ± 0.1	1590 ± 30	313 ± 2	8.3 ± 0.1	74 ± 2	523 ± 13	165 ± 9

T (K)	P (GPa)	σ_0 ($\Omega^{-1}cm^{-1}$)	ω_{Dp} (meV)	γ_D (meV)	$\omega_{0,osc}$ (meV)	$\omega_{p,osc}$ (meV)	γ_{osc} (meV)
200	0.6 ± 0.1	1415 ± 20	295.0 ± 0.7	8.3 ± 0.1	75.3 ± 0.7	569.0 ± 8	154 ± 4
200	0.9 ± 0.1	1461 ± 20	308 ± 1	8.7 ± 0.1	81.4 ± 0.9	599.1 ± 9	155 ± 5
200	1.0 ± 0.1	1479 ± 20	300 ± 1	8.1 ± 0.1	67 ± 1	540 ± 9	150 ± 5

T (K)	P (GPa)	σ_0 ($\Omega^{-1}cm^{-1}$)	ω_{Dp} (meV)	γ_D (meV)	$\omega_{0,osc}$ (meV)	$\omega_{p,osc}$ (meV)	γ_{osc} (meV)
300	0.2 ± 0.1	1338 ± 20	290.8 ± 0.7	8.5 ± 0.1	69.8 ± 0.6	503.3 ± 7	141 ± 4
300	0.7 ± 0.1	1386 ± 40	300 ± 2	8.8 ± 0.2	86 ± 2	600 ± 16	200 ± 12
300	1.1 ± 0.1	1402 ± 20	298 ± 1	8.5 ± 0.1	66 ± 1	440 ± 9	135 ± 6

Table 3.2: Drude-Lorentz fit parameters of optical properties of poly-crystalline K_3C_{60} at different external hydrostatic pressure at 20 K (top), 100 K (second from the top), 200 K (middle) and 300 K (bottom). ω_{Dp} and γ_D are the Drude frequency and scattering rate of the free electrons respectively, and are used to recalculate the zero frequency values of the conductivity σ_0. The polaronic absorption peak has been fitted by an oscillator characterised by the central frequency $\omega_{0,osc}$, its strength $\omega_{p,osc}$ and by a damping γ_{osc}.

γ_D hint to an almost completely restored number of free carriers, similar to the one of the single crystal, which can be possibly attributed to the pressurisation of the powders that improves the inter-grain electronic transport. The MIR absorption strength, on the other hand, is not fully restored.

3.3 Summary

In this chapter the equilibrium optical response properties of potassium doped fullerides A_3C_{60} has been introduced. Optical reflectivity and optical complex conductivity spectra were discussed both for the case of single crystal and powders samples. In the metallic phase the optical response in modelled by means of the Drude model and its temperature and pressure dependence are shown. Below the critical temperature, the optical response strongly reshapes and conventional features compatible with the one expected from the BCS theory in the strong-coupling limit appear. The evolution of the superconducting parameters are then described at different temperatures.

The resonant excitation of K_3C_{60} powder by means of strong mid-infrared pulses will be discussed in the rest of the manuscript. The observation of the optical response of a material at equilibrium carries non-trivial information of the analysed system, as discussed in this chapter. In the next chapters the light-induced changes of the optical response will be discussed in light of the emerged properties discussed here.

CHAPTER 4

Light-induced superconductivity in K_3C_{60}

Potassium doped fullerides K_3C_{60} become superconducting below 20 K thanks to the interplay of strong electronic interactions and molecular distortions of the buckyballs. The selective excitation of vibrational modes of the C_{60} molecules by means of mid-infrared light is expected to influence the conditions that at equilibrium support the onset of superconductivity.

The first section of this chapter shortly provides an overview of the possible lattice dynamics accessible to electromagnetic radiation in K_3C_{60}. The response of K_3C_{60} to optical excitation in the mid-infrared is then described in terms of optical spectra measured by means of THz time-domain-spectroscopy, first for powders samples excited from their superconducting state, and, in a later section, for excitations of the metallic sample.

Upon excitation, K_3C_{60} shows a transient response resembling the one of the equilibrium superconductor at temperatures much higher than the equilibrium T_c. The main part of the chapter describes how this exotic transient response varies as a function of pump fluence, temperature and pump photon energies [23].

Finally, possible theoretical explanations for the superconducting-like response of K_3C_{60} are briefly discussed. Both the reported theories postulate

the resonant excitation of a mid-infrared molecular mode and investigate the effect of nonlinear couplings to other degrees of freedom.

4.1 Optically driven lattice dynamics in K_3C_{60}

Chapter 1 introduced some first experimental observations of light-induced phase transitions which motivated scientists to apply strong field pulses to drive instabilities in different systems. The strong excitation of molecular distortions of K_3C_{60} is in the same way expected to trigger anharmonic dynamics in the solid, possibly reflecting on the electronic order [15, 16].

Superconductivity in K_3C_{60} is supported by a dynamic molecular elongation of C_{60} molecules along their poles [65, 21]. Such Jahn-Teller distortion affects the geometry of the interested molecules and lifts the electronic ground state degeneracy of the conduction band (see Chapter 2). This deformation is dynamic, and continuously evolves along the three crystallographic directions reshaping the conduction molecular orbitals and their electronic density distribution along the respective directions [86]. The electronic coupling of the t_{1u} conduction electrons to this molecular distortion is particularly strong [21] and leads to a reversion of the Hund's rule, with the consequent formation of a low spin and angular momentum ground state [74].

The dynamical Jahn-Teller distortion of the C_{60} molecules belongs to highly degenerate Raman active phonons of irreducible representation H_g. Perturbations along the eigenvectors of this molecular vibrational mode, are expected to interfere with the superconducting properties of K_3C_{60}.

As introduced in Chapter 1, infrared active phonons can induce a net displacement along the coordinate of Raman modes which are allowed by symmetry constrains, i.e. which preserve the total symmetry of the system. The high symmetry of C_{60} molecules severely restrict the number of Raman and infrared spectroscopically active modes. The C_{60} molecule possesses 46 distinct vibrational modes classified according to their symmetry as:

$$2A_g + 3T_{1g} + 4T_{2g} + 6G_g + 8H_g + A_u + 4T_{1u} + 5T_{2u} + 6G_u + 7H_u, \quad (4.1)$$
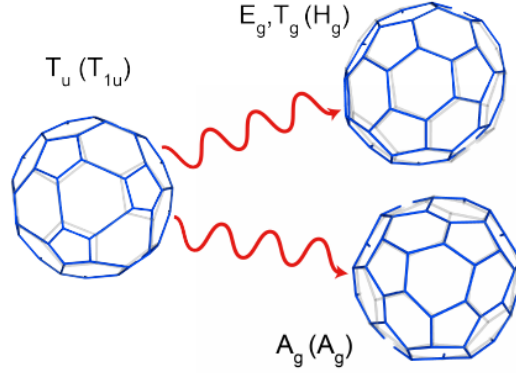
Figure 4.1: Couplings between the $T_{1u}(4)$ mode and H_g Raman vibrations of the C_{60}^{3-} molecules. The distorted structure associated with each mode and for a 9% change of the C-C bond length are shown as blue lines while the equilibrium structure is depicted in light grey. Distorted structures have been kindly provided by Dr. Alaska Subedi.

among which 32 are optically silent [87]. The only first order IR active molecular modes are the one of T_{1u} representation, which are often referred as charged-phonons, because of their increased oscillator strength compared to the case of pure C_{60}, at the expenses of the conducting electrons [88, 65, 89]. Potassium doped fullerides have four different T_{1u} phonons which by symmetry couple to A_g, T_{1g} and H_g Raman modes [90, 91]. By means of this nonlinear phonon coupling, the tangential T_{1u} motion of the carbon atom on the C_{60} molecules (left side) is therefore transferred to breathing modes of the entire buckyball along the H_g eigenvectors (upper right configuration). As the H_g modes show a strong electron-phonon coupling, their anharmonic coupling to infrared active modes opens the possibility of light-control of electronic properties in alkali doped fullerides, which is the topic of the rest of the chapter.

4.2   Mid-infrared resonant excitation of K_3C_{60} below T_c

Ultrashort sub-ps mid-infrared (MIR) pulses have been used to excite K_3C_{60} out of equilibrium starting from its equilibrium superconducting and metallic states. Its optical response has been measured in the THz frequency range by means of THz time domain spectroscopy (THz-TDS).

In this experiment s-polarised MIR pulses of about 300 fs of duration were tuned at resonance with the infrared active $T_{1u}(4)$ vibrational mode at 170 meV. The light-induced changes in the low-frequency electrodynamics of K_3C_{60} have been measured with p-polarised THz pulses from 3 to 11 meV (0.7 - 3 THz). The temporal resolution of the experiment, as explained in Appendix C, is limited by the pump pulse duration while the spectral resolution was set to 0.4 meV (0.1 THz). The fulleride powders have been prepared in an oxygen free environment to avoid contaminations that lead to a structural transition towards an amorphous phase [92, 93, 94], as explained in Appendix A. Cool temperatures have been achieved by means of a liquid He cooled cryostat. A more detailed description of the experimental apparatus can be found in Appendix C.

The response of the superconducting K_3C_{60} has been measured at 10 K, below the critical transition temperature ($T_c = 20$ K). The reflected THz pulse used in the experiment in absence of mid-infrared excitation (dark blue curve) together with the relative changes $\Delta E = E_{on} - E_{off}$ induced by MIR pump measured 2 ps after the excitation (light blue curve) are displayed in Fig. 4.2(a). The light-induced changes of the THz pulse are out-of-phase with respect to the unperturbed pulse, hinting for an overall reduction of the reflectivity in the probed spectrum. By sampling the peak amplitude at several pump probe delays in correspondence of the dashed gray line ($t = 0$ ps), the temporal evolution of the light-induced averaged frequency changes of the reflected THz spectrum is obtained and plotted for a selection of pump fluences (Fig. 4.2(b)). For pump fluences higher than 0.5 mJ/cm^2, the system is overheated and a long-lived feature with ms lifetime appears. The light-induced changes in the reflected THz pulse are characterised by a relatively
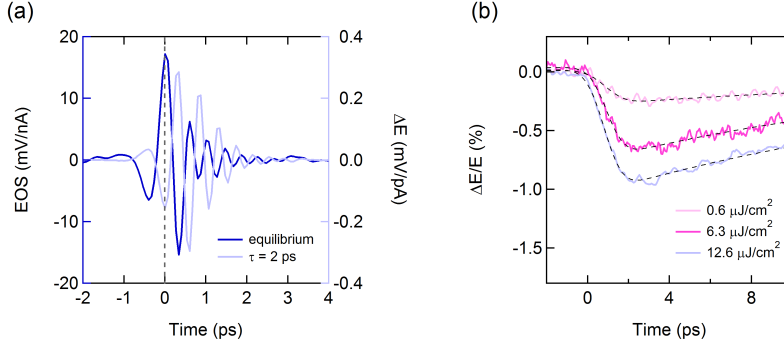
Figure 4.2: **(a)** Reflected THz pulse (dark blue curve) and its relative changes (light blue curve) induced 2 ps after the excitation on K$_3$C$_{60}$ pumped at 10 K, below T_c. **(b)** Frequency integrated temporal evolution of the excited state for selected fluences. Black dashed lines are the result of single exponential fits.

long rise time of about 2 ps, a 20 ps long single exponential decay, and have overall a negative sign, implying that within the probed spectrum the reflectivity is reduced.

More useful and complete insights on the nature of the light-induced state have been obtained from the temporal evolution of the spectrally resolved response below T_c. Figure 4.3 reports snapshots of the optical reflectivity at the sample-diamond interface (panel **(a)**), and of the complex optical conductivity spectra $\sigma_1(\omega)$ and $\sigma_2(\omega)$ (panels **(b)** and **(c)** respectively) at equilibrium (blue curve) and for a selection of pump probe delays. The maximum changes in the THz spectrum are measured 3 ps after the pump arrival (dark pink curve) and at longer pump probe delays they slowly thermalise back to equilibrium. The optical reflectivity spectrum right after the excitation is characterised by an abrupt reduction of the reflectivity (panel **(a)**) which slowly evolves back towards the saturated values of the equilibrium. In correspondence to the reduction of the reflectivity, the gap in $\sigma_1(\omega)$ uniformly fills (panel **(b)**) and the low-frequency divergence of the $\sigma_2(\omega)$ becomes less steep (panel **(c)**). At pump-probe delays longer than 100 fs, the optical properties of the equilibrium superconductor are almost completely restored.

The analysis of the spectra reported in Fig. 4.3 suggests that the resonant excitation of the T_{1u} vibrational mode in K$_3$C$_{60}$ below T_c is detrimental for
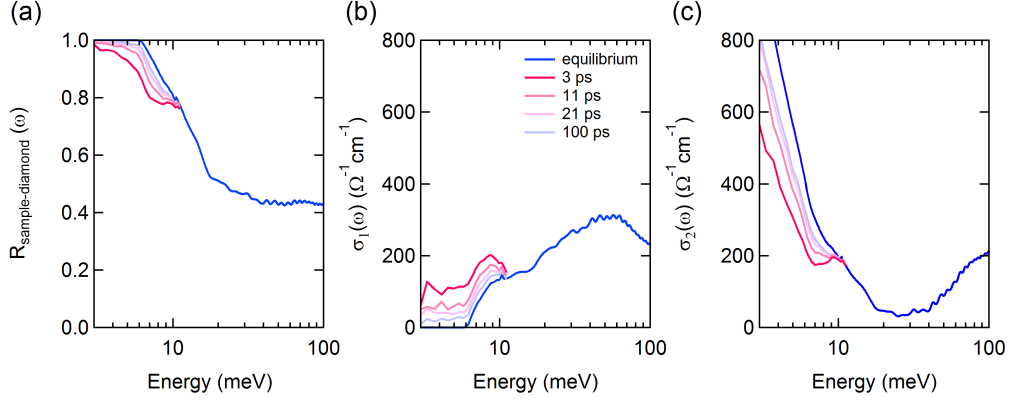
65

Figure 4.3: Spectrally resolved temporal evolution of the optical properties of the photoexcited state of K_3C_{60} at 10 K under resonant MIR excitation. Optical reflectivity at the sample-diamond interface, real and the imaginary part of the optical conductivity in the THz region at different pump probe delays are shown in panels **(a)**, **(b)** and **(c)** respectively, for a pump fluence of 0.4 mJ/cm^2.

superconductivity. The filling of the superconducting gap, the non saturated reflectivity and the reduced number of superconducting carriers (proportional to the slope of $\sigma_2(\omega)$) are likely to be ascribed to a light-induced breaking of Cooper pairs. The observed dynamic of the optical response of photo-excited superconducting K_3C_{60} is indeed compatible with the one of Cooper pairs recombination, on the order of hundreds of *ps* [95, 96].

In the same way as for the equilibrium superconductor-to-metal transition, also the light-induced transition happens without sizeable changes in the optical gap size, identified by the edge in the real spectrum of the conductivity, always around 6 meV.

The position and temporal evolution of the superconducting transient gap size can be better appreciated in the normalised ratio σ_{1sc}/σ_{1n} plotted in Fig. 4.4**(a)**, where $\sigma_{1sc}(\omega)$ is either the equilibrium superconducting real conductivity spectrum (dark blue curve) or the transient one measured at several pump probe delays after the MIR excitation. The normalisation has been done by means of the $\sigma_{1n}(\omega)$ of metallic K_3C_{60} at 25 K. The unexpected changes at the edge of the probed area around 10 meV suggest that not only the free-carriers of the Drude are participating in the transient state, but also
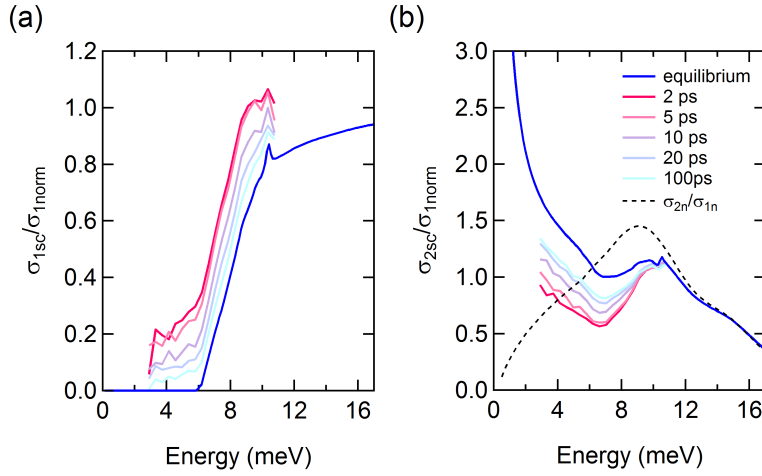
Figure 4.4: Temporal evolution of the normalised real ((**a**)) and imaginary part ((**b**)) of the transient conductivity spectra of powders of K_3C_{60} measured at 10 K, plotted at different pump probe delays. The dark blue curves describe the equilibrium response of K_3C_{60}, while the dashed dark line in panel (**b**) is the σ_{2n}/σ_{1n} ratio of the normal state at 25 K.

that electrons belonging to higher energy absorptions are involved. Finally, Fig. 4.4(**b**) shows the response of the superconducting carriers, proportional to the ratio σ_{2sc}/σ_{1n}. The MIR excitation promptly destroys the coherence of the superconducting carriers, and the peak at 11 meV, already discussed for the equilibrium case in Chapter 3, becomes more evident. As previously envisaged already in the normal carrier response, the photo-stimulated evolution of the superconducting K_3C_{60} towards a transient metallic phase is accompanied by a suppression of the $1/\omega$ coherent response even at frequencies higher than the equilibrium optical gap (6 meV), hinting that the MIR excitation is not trivially influencing the electronic response.

4.3 Light-induced superconducting-like phase above T_c

Resonant MIR excitation at 170 meV has been additionally used to drive powders of K_3C_{60} out of equilibrium above T_c. THz probe pulses were used
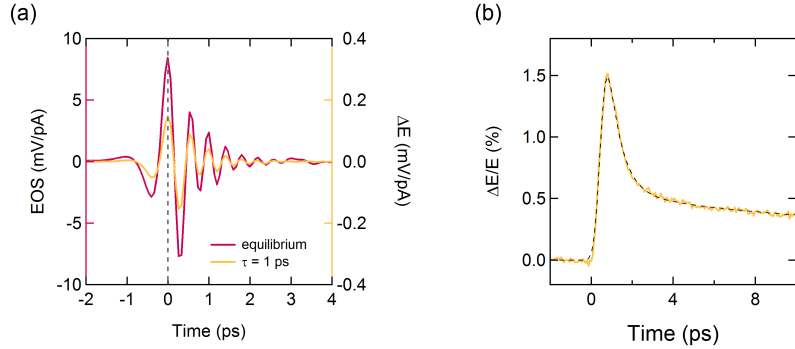
Figure 4.5: **(a)** Reflected THz pulse (red curve) and its relative changes (yellow curve) induced 1 ps after the excitation on K_3C_{60} pumped at 25 K, above T_c. **(b)** Frequency integrated temporal evolution of the excited state for a pump fluence of 1 mJ/cm^2. The black dashed line is the result of a double exponential fit.

to track changes in the low-frequency optical response of the sample, first, from 3 to 11 meV, and, subsequently, from 5 to 31 meV, in order to explore an even broader spectral window.

Figure 4.5**(a)** shows the narrower THz electric pulse reflected by the unperturbed sample at 25 K (red line) measured with THz-TDS, and the relative light-induced changes 1 ps after the excitation (yellow curve). While the response below T_c is characterised by an overall reduction of the reflectivity (negative sign), when K_3C_{60} is excited above its critical temperature the reflectivity is on average enhanced. The frequency integrated response sampled on the peak of the THz pulse (identified by the dashed line at $t = 0$ ps in panel **(a)**), has a positive sign (panel **(b)**). The rise-time of the dynamic of K_3C_{60} above T_c is limited to the resolution of the setup (300 fs), while its temporal evolution is captured by a double exponential decay. A first fast dynamic with time constant of 0.64 ps (± 0.02 ps) is on top of a second slower one characterised by a time constant of 9.36 ps (± 0.89 ps).

The different dynamic of the light-induced state in K_3C_{60} pumped at 25 K with respect to the one induced below its critical temperature hints for a different nature of the photo-excited state, which can be better appreciated by looking at the frequency resolved optical response [23].

The optical reflectivity at the sample-diamond interface (panel **(a)**) and com-
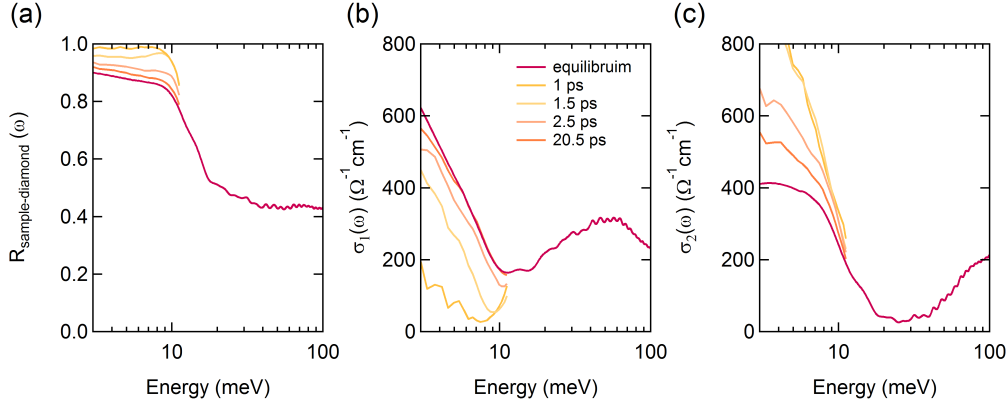
Figure 4.6: Spectrally resolved temporal evolution of the optical properties of the photoexcited state of K_3C_{60}, pumped at 25 K under resonant MIR excitation. Optical reflectivity at the sample-diamond interface, real and the imaginary part of the optical conductivity in the THz region at different pump probe delays are shown in panels **(a)**, **(b)** and **(c)** respectively, for a pump fluence of 1.1 mJ/cm^2.

plex optical conductivity spectra (panels **(b)** and **(c)**) of K_3C_{60} in its equilibrium metallic phase at 25 K (red curves) and at different pump-probe delays after the MIR pump are reported in Fig. 4.6. On the peak of the transient response ($\tau = 1$ ps) the optical reflectivity is strongly enhanced in most of the probed area, and saturates to $R(\omega) = 1$ below 10 meV. Correspondingly, in $\sigma_1(\omega)$ most of the spectral weight is moved elsewhere, and an optical gap resembling the one of a superconductor at finite temperature appears. These changes are accompanied by the appearance of a strong $1/\omega$ divergence at low energy in $\sigma_2(\omega)$. At longer pump probe delays the effect gradually weakens: the reflectivity decreases, more spectral weight is moved back in the depleted $\sigma_1(\omega)$ and a finite peak reappears in $\sigma_2(\omega)$. After 20 ps from the excitation, the optical properties of photo-excited K_3C_{60} resemble the one at equilibrium.

First insights on the nature of the light-induced state of K_3C_{60} above T_c can be obtained by comparing the transient optical response to the one of the thermally induced superconducting phase transition, shown in Fig. 3.3. The strong similarity of these optical spectra supports the interpretation of the photo-excited state as a transient superconductor, likely strengthened by the

MIR resonant excitation. Following this hypothesis the in-gap spectral content which populates the lower part of the $\sigma_1(\omega)$ spectrum can be attributed to the high temperature of the sample, and to the finite lifetime of the superconducting state. The biggest difference compared with the equilibrium superconductor is the size of the optical gap 2Δ. In the unperturbed case 2Δ is around 6 meV, while in the transient state it broadens up to at least 10 meV.

The strength of the light-induced state has been quantified by means of a figure of merit chosen to be related to the depletion of the real conductivity. The relative Spectral Weight Loss in $\sigma_1(\omega)$ at a fix pump-probe delay τ (SWL_τ) is defined as,

$$SWL_\tau = \frac{\int_a^b (\sigma_{1,eq}(\omega) - \sigma_{1,\tau}(\omega))}{\int_a^b \sigma_{1,eq}, (\omega)} \tag{4.2}$$

with a and b set within the photo-induced gap in the probed spectral region. The maximum depleted $\sigma_1(\omega)$ spectrum at 1 ps after the pump arrival has been integrated between 3.1 and 10.3 meV and has been plotted as a function of pump probe delay (Fig. 4.7$(\mathbf{a})$). The temporal evolution of the light-induced spectral weight loss can be fitted by a single exponential decay, with a time constant compatible with the fast one of Fig. 4.5$(\mathbf{b})$. The relevant time scale for the existence of the transient state is about 1 ps.

To further investigate the distinctive properties of the anomalous transient phase, the response of K_3C_{60} has been measured under other experimental conditions. The full characterisation of the light-induced state has been hence studied as a function of pump fluence, pump energy and temperature.

Fluence dependence

The response of K_3C_{60} to MIR excitation has been studied as a function of impinging pump fluence. The mid-infrared pump pulses, tuned at 170 meV were attenuated by means of a pair of crossed wired grid polarisers, conveniently disposed to adjust the throughput. The pump fluences used in the experiment were spanning from zero to 3 mJ/cm^2 circa.
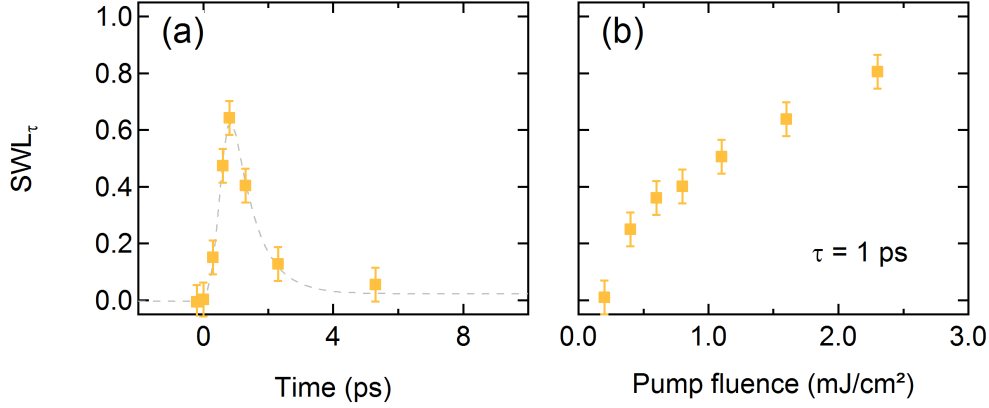
Figure 4.7: Photo-induced reduction in $\sigma_1(\omega)$ spectral weight integrated between 3.1 and 10.3 meV, measured in K_3C_{60} pumped at 25 K, plotted as a function of pump probe delay **(a)** and as pump fluence **(b)**. Data in **(a)** are measured with a pump fluence of 1.1 mJ/cm^2. The grey dashed line is the result of a single exponential fit of the data. Data in **(b)** refer to 1 ps pump probe delay.

The summary of the fluence dependence is shown in Fig. 4.7**(b)**. Within the explored range, no clear threshold, nor a saturation can be observed, and the light-induced changes are smoothly enhanced by stronger excitations. Based on the frequency resolved optical snapshots it is additionally possible to define two regions. A first one in which a fully formed optical gap opens in the $\sigma_1(\omega)$ spectrum, corresponding to $SWL_\tau \geq 0.5$ and pump fluences higher than 0.8 mJ/cm^2, and another one where only a partial depletion is found, for $SWL_\tau < 0.5$ and reduced pump fluences.

Wavelength dependence

The photo-susceptibility of K_3C_{60} to different phonon pump energies is reported in Fig. 4.8**(a)**. The MIR pulses were tuned from 80 to 700 meV excluding the diamond absorption window, dashed area in the figure (210 - 500 meV). The yellow and orange squares refer to two dataset of wavelength dependences, acquired at a fixed pump fluence of 1.1 mJ/cm^2 and 0.4 mJ/cm^2 respectively. In both cases of fully- or partially-formed gap, no sharp resonance is found at 170 meV, but a rather broad response is observed
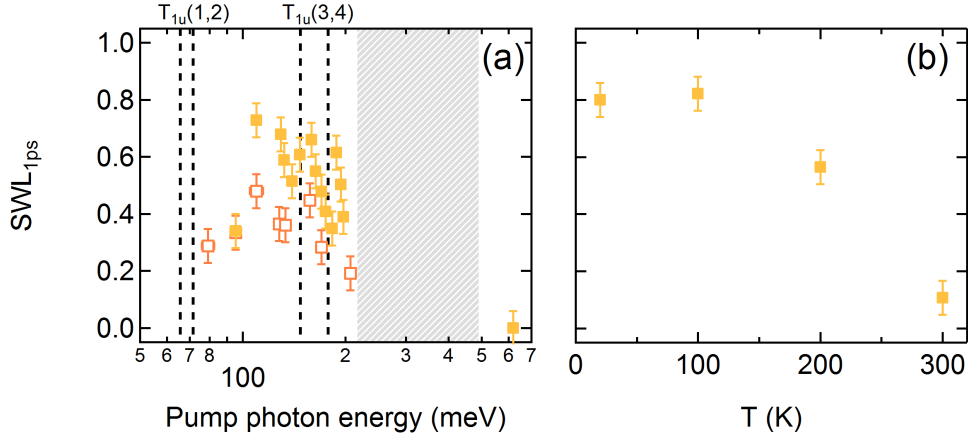
Figure 4.8: Photo-induced reduction in $\sigma_1(\omega)$ spectral weight integrated between 3.1 and 10.3 meV, 1 ps after the excitation of K_3C_{60} plotted as a function of pump photon energy **(a)** and for different temperatures **(b)**. Data in **(a)** are measured at 25 K and the dark vertical lines are the frequencies of the four T_{1u} vibrational modes. All data have been measured with a pump fluence of 1.1 mJ/cm^2.

around two of the molecular vibrations $T_{1u}(3)$ and $T_{1u}(4)$, corresponding to stretching and compression of the hexagons and pentagons of the fulleride molecules. A weaker response is still observed for wavelengths extending towards the $T_{1u}(1)$ and $T_{1u}(2)$ resonances. When higher pump energies are used, i.e. around 600 meV, no pump-probe signal can be measured, suggesting that the low energy, vibrational excitation might be of key importance in the understanding of this transient phenomena.

Temperature dependence

The behaviour of the light-induced transient phase in metallic K_3C_{60} has been finally studied above its critical temperature by measuring the response at different temperatures at a constant pump fluence of 1.1 mJ/cm^2. Strikingly, by driving the system at 100 K, the optical response resembles the ones obtained at 25 K. The reflectivity at the sample-diamond interface, 1 ps after the pump arrival, saturates to one ($R(\omega) = 1$), a complete gap opens in the real conductivity spectrum and a strong divergence in the low energy of its imaginary part appears. The effect is then gradually reduced for in-

creasing temperatures, and at 200 and 300 K the enhancement of the optical reflectivity is only partial, the depletion of the $\sigma_1(\omega)$ not complete and the divergence in $\sigma_2(\omega)$ not that pronounced. The temperature dependence is summarised in terms of SWL_τ in Fig. 4.8(**b**).

The characterisation of the light-induced response of K_3C_{60} has been supported by a fitting procedure in which a superconducting and a metallic model have been used. Given the similarities with the equilibrium superconductor, first, an extended model for superconductor with arbitrary purity [97] has been used to fit simultaneously the optical properties (reflectivity and complex conductivity) at all the measured temperatures. Even if the photo-susceptibility of K_3C_{60} to MIR excitation reduces when approaching room temperature, the size of the light-induced optical gap does not follow the predicted behaviour of BCS theory. At all the measured temperatures, the gap value extracted from the fit falls around 10 meV.

A Drude model could also be used to fit the optical properties of the light-induced state. Importantly, in the limit of a perfect conductor with infinite scattering time ($\tau \to \infty$), a Drude model of a metal gives optical properties which cannot be distinguished from the ones of a superconductor. In this limit, the optical conductivity of the Drude model simplifies to

$$\lim_{\tau \to \infty} \sigma_1(\omega) + i\sigma_2(\omega) = \lim_{\tau \to \infty} \frac{Ne^2\tau}{m} \frac{1 + i\omega\tau}{1 + \omega^2\tau^2} = \frac{Ne^2}{m} \left(\frac{\pi}{2}\delta(0) + \frac{i}{\omega} \right), \quad (4.3)$$

where N, e and m stand respectively for the number of conducting carriers, the charge of the electrons and their mass. In the same way as an equilibrium superconductor, also a perfect conductor will be described hence by a depleted $\sigma_1(\omega)$ with a delta peak at zero frequency, and a $1/\omega$ divergent contribution in the $\sigma_2(\omega)$.

Such model has been used to fit the results measured at 200 K and 300 K. In both cases a strong reduction of the scattering rate with respect to the static response is found.

Using such model also for the 25 K and 100 K data sets would prevent from doing mistakes related to inconsistencies deriving from broken BCS constrains, like the temperature dependence of the optical gap size. In order

to proceed, broader THz pulses to measure the superconducting-like optical response of K_3C_{60} at ambient pressure are needed.

4.3.1 Broadband THz data for the superconducting-like response

The superconducting-like response of K_3C_{60} to resonant MIR excitation has been measured in an extended probed spectral region by means of broader THz-pulse with spectral content from 5 to 31 meV (1 - 7.5 THz). These pulses have been generated by means of optical rectification in a GaP non-linear crystal, as discussed in detail in Appendix C.

The extended optical reflectivity and the complex optical conductivity spectra of photo-excited potassium fulleride pumped at 100 K are displayed in Fig. 4.9, together with the narrower ones for direct comparison. After 1 ps from the excitation, the lower spectral content of the optical reflectivity in the two experimental conditions are in agreement with each other. The broad THz data, on the other hand, show that the reflectivity edge falls at an even higher energy with respect to the one previously identified. The same difference emerges from the direct comparison of the real part of the optical conductivity (panel **(b)**). Rather different curves have been obtained for the imaginary $\sigma_2(\omega)$ where for the broadband dataset a stronger divergence at low energy emerges. This difference can be ascribed to the improved detection scheme, more accurate in the measurement of phase changes (see Appendix C).

To discuss the formation of the possible transient superconducting state, the ratios of the real and imaginary part of the conductivity normalised to the real normal conductivity at 100 K are displayed in Fig. 4.10 for different pump probe delays. In panel **(a)** the ratio of the transient superconducting-like $\sigma_{1sc}(\omega)$ and the normal $\sigma_{1n}(\omega)$ has been plotted for a fully formed gap ($\tau = 1$ ps) and at longer pump-probe delays. The light-induce response extends up to 30 meV, beyond the one at equilibrium, and the spectral weight lost within the gap region quickly recovers. Additionally, the ratio σ_{2sc}/σ_{1n} plotted in panel **(b)**, clearly shows that MIR excitation induces a strong co-
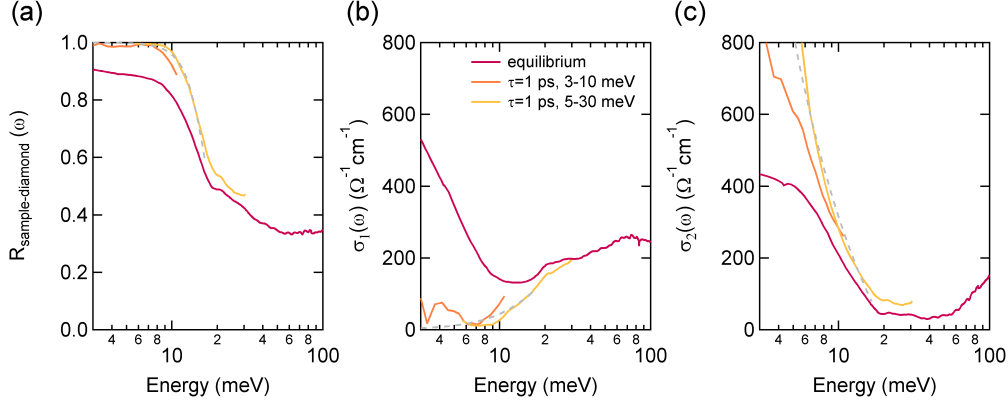
Figure 4.9: Reflectivity at the sample-diamond interface (**(a)**), real (**(b)**) and imaginary (**(c)**) optical conductivity of K_3C_{60} at equilibrium (red) and 1 ps after photoexcitation at $T = 100$ K. The orange curves show the data measured with a THz pulse with spectral content from 3 to 10.5 meV at a pump fluence of 1 mJ/cm^2, while those in light yellow are measured with a broader probe spectrum (5 - 31 meV) and a higher pump fluence (3 mJ/cm^2). Dashed light grey curve are the result of a Drude fit. Figure adapted from [24].

herent response in K_3C_{60}, extending to all the measured spectral region. At longer delays, around 20 ps the system is already back to equilibrium.

The broader transient optical properties of K_3C_{60} have been modelled at all measured temperatures (25 K, 100 K, 200 K and 300 K) with a Drude-Lorentz function in which a high-frequency oscillator was added to the Drude term to account for the polaronic band (Eq. 3.5 in Chapter 2). The starting parameter used are based on the equilibrium response fits. The light-induced reflectivity and complex optical conductivity were simultaneously fitted by letting free only the Drude characteristic frequencies (plasma frequency and scattering rate). Figure 4.9 shows a representative fit of the transient optical properties at 100 K in light grey dashed lines.

The optical conductivity at zero frequency σ_0 was calculated from the fit results, as

$$\sigma_0 = \frac{\omega_P^2 \tau}{4\pi}. \tag{4.4}$$

In the case of the 100 K dataset, the value of the zero frequency conductivity approaches infinity, being the fitted scattering rate almost zero. Table 4.1
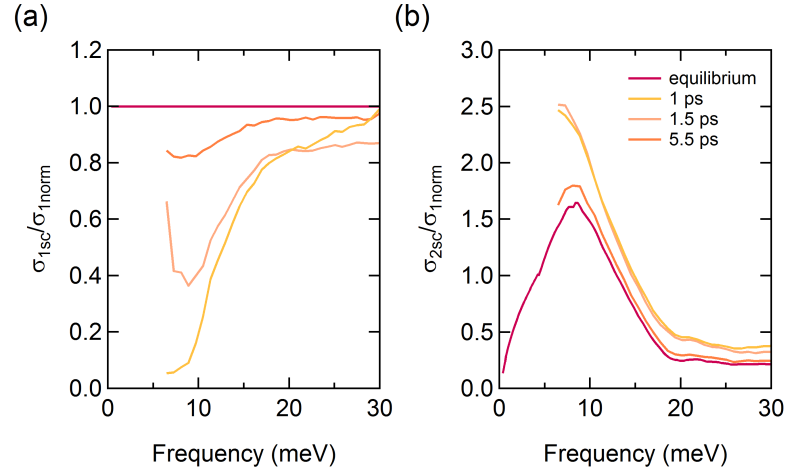
Figure 4.10: Evolution of the normalised real (**(a)**) and imaginary part (**(b)**) of the transient conductivity spectra of powders of K_3C_{60} measured at 100 K, plotted at different pump probe delays after the MIR excitation. The dark red curves describe the equilibrium starting conditions.

reports the fit parameters for all the measured temperatures together with the retrieved value of the zero frequency conductivity. As expected, the transient states at 25 K and 100 K are compatible with the superconducting-like picture, as they are characterised by extremely high zero-frequency conductivity and zero scattering rate. Interestingly, the high temperature datasets display transient conductivities enhanced by almost an order of magnitude with respect to the starting metallic phase.

In absence of further investigation, on the other hand, the optical spectra of the light-induced transient state hold the ambiguity between their possible superconducting and metallic natures. While the low temperature data sets, with $SWL_\tau \geq 0.5$, can be properly described by a superconducting-like model with extremely high conductivity, the high temperature ones, with $SWL_\tau < 0.5$ are more compatible with a light-induced high mobility metal. To remove such ambiguity, the photo-induced response of K_3C_{60} has been studied in presence of external pressure, as discussed in detail in the next chapter.

T (K)	σ_0 ($\Omega^{-1}cm^{-1}$)	ω_{Dp} (meV)	γ_D (meV)
25	$10^{14} \pm 10^{10}$	197.14 ± 15	0 ± 0.1
100	$10^{18} \pm 10^{13}$	183 ± 62	0 ± 0.13
200	11499 ± 5902	184 ± 2	0.39 ± 0.24
300	9276 ± 2403	$162.6 \pm .8$	3.09 ± 0.81

Table 4.1: Drude-Lorentz fit parameters of the transient optical properties of polycrystalline K$_3$C$_{60}$ measured at 1 ps pump-probe delay, at different temperatures above T_c. The plasma frequency ω_{Dp} and the scattering rate γ_D of the Drude are used to recalculate the zero frequency values of the conductivity σ_0.

4.4 Interpretation for the out-of-equilibrium superconductivity in K$_3$C$_{60}$

The transient optical response from driven K$_3$C$_{60}$ shows remarkable similarities to the optical properties of the equilibrium superconductor. However, in absence of further investigations the optical properties alone cannot unambiguously discriminate its superconducting nature. Independently to the nature of this exotic phase the strong enhancement of the conductivity of the material makes this experiment of particular interest but the understanding of the microscopic mechanism behind it is still not complete.

Several theoretical works have been proposed to possibly interpret the origin of the transient state found in K$_3$C$_{60}$ and all of them postulate the resonant excitation of the mid-infrared T_{1u} vibrational mode. The extremely high intensity of the laser pulses used for the experiment, of the order of 1 MV cm^{-1}, is expected to induce large oscillatory distortion of the C-C bonds. Therefore, in these experimental conditions, higher order interactions are expected to affect the system and must be thus taken into account.

Based on recent findings [17, 18], one possible interpretation for the light-induced superconducting-like state in potassium fullerides, proposes that an indirect excitation of Raman molecular vibrations, via nonlinear phononics, can be responsible for the coherently stimulated transition from the high-temperature metallic state into a non-equilibrium superconductor. Specifically, the MIR driver is expected to deform the system along the infrared
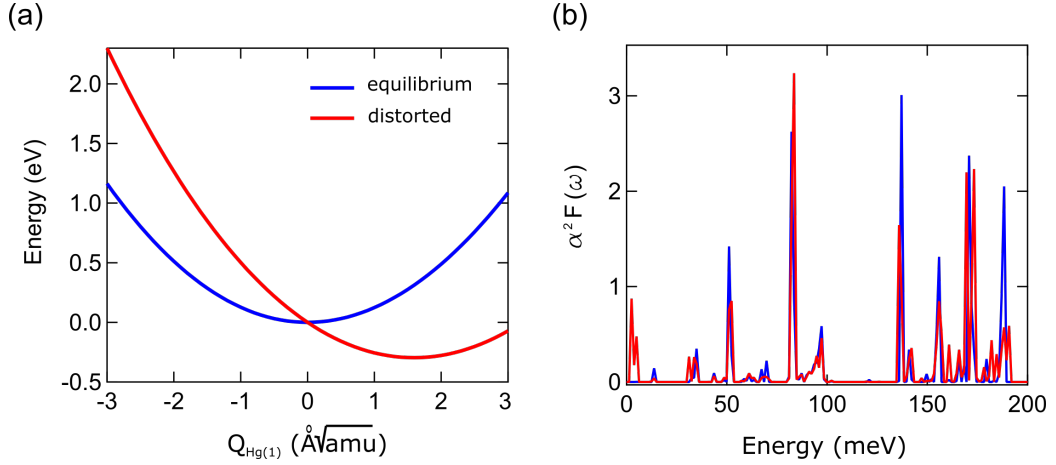
Figure 4.11: **(a)** Calculated total energy curves of the $H_g(1)$ vibrational mode in the unperturbed case (blue curve) and its reshape due to the excitation of the $T_{1u}(4)$ mode by 2 Å$\sqrt{amu}$ (red curve). **(b)** Calculated frequency resolved electron–phonon coupling function of the unperturbed and distorted structure, plotted in the same color scale [23].

coordinate and along other anharmonically allowed coordinates, according to the nonlinear phononics theory (see Chapter 1). To the lowest order, the quadratic coupling considered is of the form $Q_{IR}^2 Q_R$, with Q_{IR} being the directly excited coordinate relative to the $T_{1u}(4)$ phonon, and Q_R the anharmonically activated one. As introduced at the beginning of this chapter, among all the allowed Raman modes, H_g phonons are coupled to the excited T_{1u} molecular mode. Density functional theory (DFT) calculations with a plane-wave basis set and projector augmented wave pseudopotentials [23], predict a shift of the $H_g(1)$ Raman mode energy minimum for finite amplitude of the $T_{1u}(4)$ vibration. Figure 4.11**(a)** shows the displaced minimum of the $H_g(1)$ potential when the amplitude of the $T_{1u}(4)$ mode is 2.0 Å$\sqrt{amu}$, resulting in an effective net displacement of the structure along the Raman coordinate. Importantly, the recalculated band structure of such displaced system exhibit a lifted degeneracy of the conduction band manifold at the Γ point.

All these structural changes reflect onto the electron-phonon coupling λ, cal-

culated by integrating the Eliashberg function $\alpha^2 F(\omega)$ as

$$\lambda = 2 \int_0^\infty \frac{\alpha^2 F(\omega)}{\omega} d\omega. \qquad (4.5)$$

Strikingly, the distorted structure is characterised by a doubled coupling force between the Raman activated phonon $H_g(1)$ and the electrons of the t_{1u} conduction band (Fig. 4.11(**b**)). Such enhancement of the electron-phonon coupling is expected to influence the superconducting properties of the photo-excited K_3C_{60} and leads to a higher pairing strength and T_c [23]. The out-of-equilibrium phase of potassium fullerides could be on the other hand the result of a direct second order coupling of the infrared active phonon of irreducible representation $T_{1u} \times T_{1u}$ to the t_{1u} conduction electrons. In the same way as in other organic materials [15, 16], strong excitation of an infrared active phonon are likely to modulate the effective electronic repulsion of the half-filled conduction bands. The tight-binding Hückel model can be used to estimate the changes of *inter*- and *intra*molecular Coulomb repulsion of the t_{1u} orbitals on a single C_{60} molecule, when the $T_{1u}(4)$ mode is driven. The on-site Hubbard U are estimated in the undistorted and the distorted structure for a driving light polarised along the x-direction. This model is based on 'frozen-phonon' approach, which assumes the Born–Oppenheimer approximation to be strictly obeyed and that the molecular orbitals adiabatically follow the atomic distortions. Calculations of the t_{1u} molecular orbitals for a distortion of 5 pm along the $T_{1u}(4)$ coordinate predict modulations in single particle energies and Coulomb repulsions U over one period of the drive, like the one reported in Fig. 4.12 (**a**) and (**b**) respectively. Interestingly, the perceived modulation of U along the direction of the polarisation of the pump is smaller in amplitude with respect to the ones along the y and z orbitals [23].

Additional first-principle calculations of the changes in the electronic structure and in the screened Coulomb matrix elements of K_3C_{60} have been performed by considering the deformation associated with the pumped T_{1u} intramolecular mode [77]. The different possible interaction imbalances and their relation to the superconducting order parameter have been investigated.
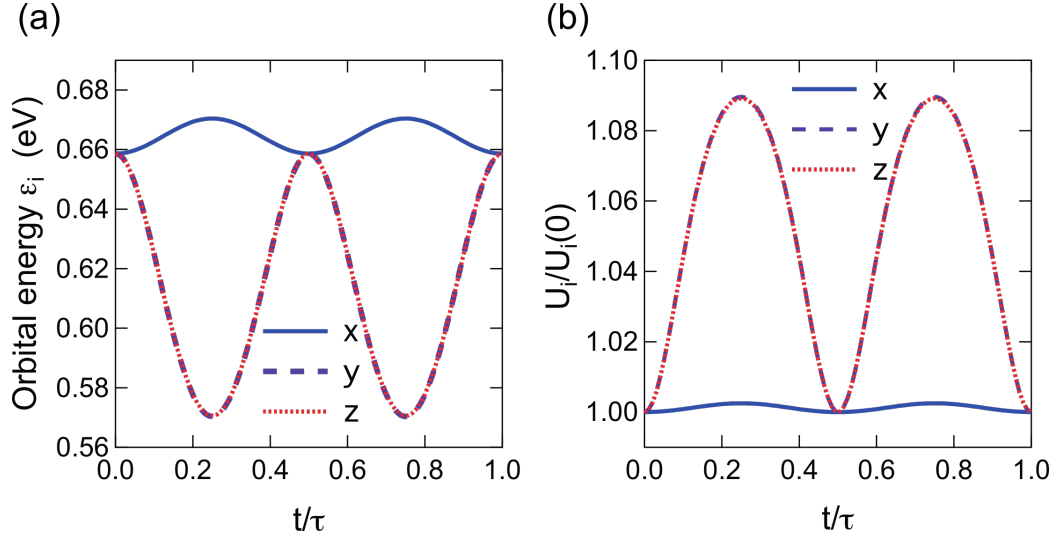
(a)

(b)

Figure 4.12: Pump-induced modulation of the orbital energy and of the onsite correlation in K_3C_{60}. **(a)** Changes in the energies of the t_{1u} orbitals along the three crystallografic directions over one period of the $T_{1u}(4)$ vibration with an amplitude 5 pm. **(b)** Relative changes in the intraorbital Coulomb repulsions [23].

While the lift of the degeneracy and an increased electronic repulsion seem to be detrimental for superconductivity, the reduction of the intramolecular Coulomb force leads to strong consequences in favour of superconductivity. According to this model, the physical mechanism responsible for the strengthening of superconductivity is the stabilisation of the intramolecular states containing a singlet pair together with a preservation of the orbital fluctuations allowing for a coherent interorbital delocalisation of the pair [77].

Figure 4.13 reports the results of the calculation relative to an increase in the electronic repulsion in terms of electronic orbitals x, y and z, for an excitation polarised along the x-axis. The ground and excited states of the electronic conduction band for the unperturbed molecule are reported on the left of the diagram. The sixfold degenerate (210) configuration, which sees two electrons on the same orbital and one in another free one, is the one that minimises the total energy. When a perturbation dU is applied along x, states with the spin-singlet pair in the x orbital are unaffected, while those
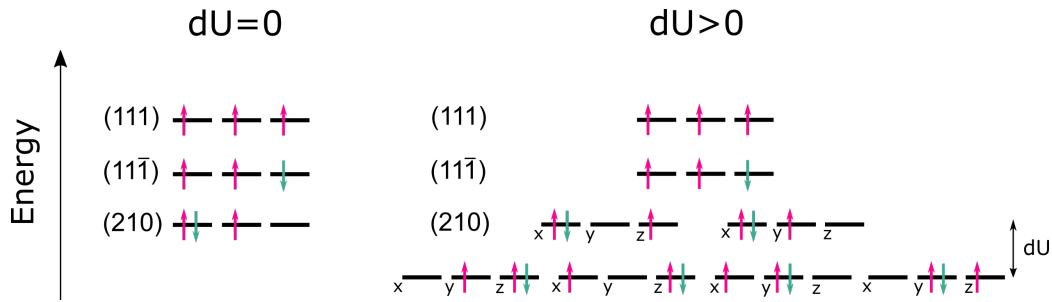
Figure 4.13: Ground and excited states for a half-filled t_{1u} shell occupied by three electrons, for an isolated molecular site, at equilibrium (left) and in the presence of the perturbations $dU > 0$ (right). (111), $(11\bar{1})$ and (210) refer to the electronic population of the conduction orbital [77].

with the pair in the z or y orbital are energetically stabilized, by an amount equal to the amplitude of the perturbation. In the distorted configuration the singlet pair are still allowed hopping within different orbitals, and therefore promote the onset of superconductivity. Within this theoretical explanation which has been also investigated in the case of dynamic stimulation [98], an anisotropic gap is expected, depending on the polarisation of the incident light.

Various and more elaborated theoretical mechanism have been invoked to explain the observation of the superconducting-like response of K_3C_{60}, including a dynamical reduction of the electronic bandwidth [99], a parametric amplification of the pairing instability [100] and a full derivation in second quantisation of the induced changes in the electron attraction [101]. The optical excitation of above-gap thermal quasi-particles into a super-excitonic state has also been proposed as a possible scenario, in which the MIR excitation is responsible for an effective cooling of the excited state, which thus promote the emergence of superconductivity at temperature higher than T_c.

4.5   Summary

The recent results obtained from powder of K_3C_{60} when excited at resonance with MIR pulses were discussed in this chapter. A transient superconducting-like response has been found from the sample, when excited from its metallic

phase ($T > 100$ K). The optical spectra measured with THz-TDS, on the peak of the pump-probe response, resemble the ones of the equilibrium superconductor, with a saturated reflectivity up to a cut-off frequency of about 11 meV, corresponding to a gapped real conductivity spectrum $\sigma_1(\omega)$ and a divergent $\sigma_2(\omega)$.

The superconducting-like transient phase lives for about 2 ps, and emerges only when the excitation is in the proximity of the infrared active T_{1u} phonons, excluding the role of direct electronic excitation from the possible interpretation.

So far different theoretical investigations were proposed, all relying on the nonlinear driving of infrared active phonons which can possibly couple to other degrees of freedom of the structure. A first possible explanation is based on the nonlinear phonon coupling among the directly excited MIR active phonon and H_g Raman active phonons, known to be of key importance for superconductivity in K_3C_{60}. A strengthened electron-phonon coupling has been attributed responsible for the stronger pairing force found in the transient superconducting-like state.

Alternatively, the indirect perturbation of the local electronic Coulomb repulsion via the direct excitation of the T_{1u} phonon has been proposed to interpret the former results. In this framework, the excitation induces a modulation of the electronic interaction term U along the direction of the excitation, removing the degeneracy of the threefold degenerate conduction band. This favours the formation of electron pairs and strengthen the superconducting order parameter.

Despite the possible microscopical explanations of the measured effect on K_3C_{60}, the experimental evidences highlight the possibility of inducing new phases characterised by an extremely high mobility of electrons. These results extending up to room temperature put scientist in front of clear signatures of striking out-of-equilibrium physical properties, resembling superconductivity, that constitute another building brick for the understanding of superconductivity at very high temperature.

CHAPTER 5

Pressure tuning of the light-induced state in K_3C_{60}

Organic materials are rather soft solids, characterised by a low bulk modulus and a relatively high compressibility. These properties result from the weak Van der Waals interactions that hold together the constituent molecules.

Alkali doped fullerides are very sensitive to external hydrostatic pressure, as it strongly affects the size of the unit cell [69], as discussed already in Chapter 2. Upon external pressure, the C_{60} molecules are put closer, their molecular overlap is altered and the electronic bands become broader [102].

In the first section of this chapter an overview of the response of equilibrium K_3C_{60} to external pressure is provided, in terms of the most relevant parameters of the metallic and superconducting state. The broadening of the band structure is associated with an enhancement of the DC conductivity of the equilibrium metal. At the same time the electronic density of states at the Fermi energy reduces with pressure and it is responsible for the suppression of the equilibrium superconducting phase.

External pressure has been applied to K_3C_{60} while performing resonant mid-infrared vibrational excitation described in the previous chapter. External hydrostatic pressure up to ~ 3 GPa has been applied to the powder sample by means of a diamond anvil cell (DAC) integrated in the THz-TDS setup.

These experiments show a quick suppression of the superconducting-like state as a function of pressure, determined by the optical spectra. This strongly supports the interpretation of the light-induced phase as a transient superconducting-like state.

5.1 Pressure dependences in equilibrium K_3C_{60}

Potassium doped fullerides are the most compact compound among the whole family of alkali doped fullerides A_3C_{60}. As introduced in Chapter 2, the lattice parameter of the unit cell is strongly affected by the diameter of the alkali atom, and for the case of K_3C_{60} is around 14.24 $\mathring{A}$ at room temperature [69]. The equilibrium properties of K_3C_{60} summarised in the phase diagram of Fig. 2.3(a) clearly show the importance of the unit cell size, especially in relation to the superconducting phase. The more expanded is the lattice, the higher is the superconducting transition temperature T_c.

In the last thirty years, external hydrostatic pressure has been applied on potassium doped fullerides and by means of different techniques, the scaling of various parameters has been measured [103, 104, 105, 106, 107]. Theoretical investigations have also been carried out to support these observations [108, 102].

K_3C_{60} is characterised by a relatively low bulk modulus of about 28 GPa [108] and by a fairly high linear compressibility of about $1.2\,10^{-2}$ GPa^{-1} [103, 109]. This means that moderate pressures can impart large changes to the structural and electronic properties. Importantly, within this pressure range, no structural changes are expected to affect the individual C_{60} molecules, which will thus just get closer to each other [21].

The electronic band structure of K_3C_{60} has been retrieved from local density approximation of the linear combination of atomic orbitals method (LDA-LCAO) for different pressure values and is plotted in Fig. 5.1 [102]. The narrow and well separated band of the unperturbed state (panel (a)), broadens as pressure increases. In particular for an external pressure of about 0.3 GPa the calculation predicts a significant broadening of the valence bands together with a less pronounced broadening of the conduction band cross-
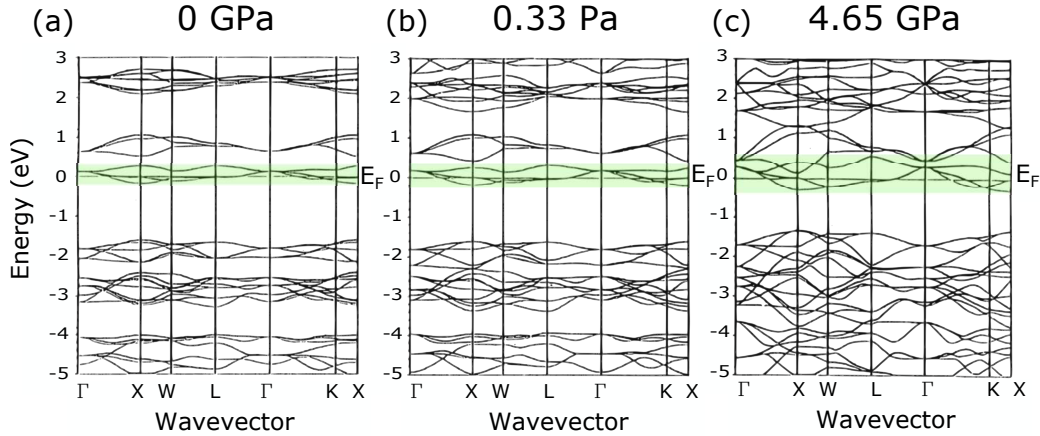
Figure 5.1: Calculated electronic structure of K_3C_{60} at room temperature under isotropic pressure. The narrow and well separated bands at **(a)** ambient pressure (lattice constant $a = 14.25$ Å, conduction bandwidth $W = 0.442$ eV) are strongly affected already at **(b)** 0.33 GPa ($a = 14.198$ Å, $W = 0.496$ eV) and **(c)** are completely overlapped at a moderate pressure value of 4.65 GPa ($a = 13.65$ Å, $W > 0.5$ eV) [102]. The green rectangles highlight the band across the Fermi level.

ing the Fermi energy (panel **(b)**). At 4.65 GPa also the conduction band is strongly affected and significant overlap among the different bands can be observed (panel **(c)**) [102]. Interestingly the gap between the conduction band and the valence band remains fairly large, around 1 eV.

Such dramatic broadening of the band structure at the Fermi level affects the electronic density of states $N(E)$ of the system. Figure 5.2**(a)** shows the reshaping of the electronic distribution within the conduction band as a function of pressure, while panel **(b)** highlights the scaling of the calculated density of the electrons at the Fermi level $N(E_F)$. The electronic density at E_F scales linearly with reducing pressure and, thus, with the lattice parameter. A sizeable reduction of $N(E_F)$, of about 25 - 30 % is expected for an external pressure of 3 GPa [108, 102].

Before describing the effect of pressure on the light-induced state found in K_3C_{60} by means of MIR excitation tuned at resonance with the intramolecular vibration at 170 meV, a short description of the scaling of fundamental parameters in both the equilibrium metallic and superconducting phase will be given in the next sections.
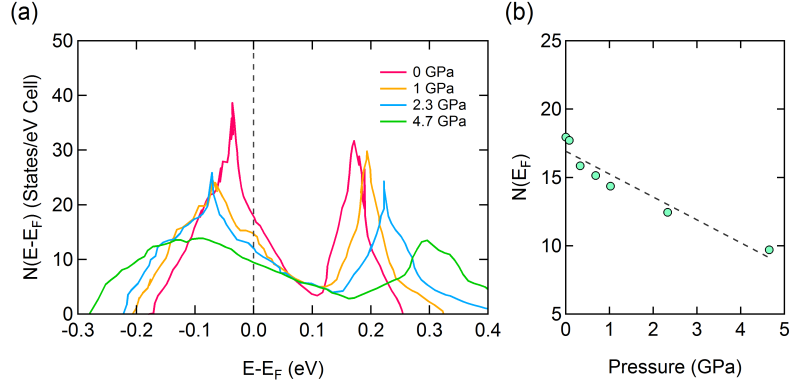
Figure 5.2: Calculated broadening of the electronic density of states of the conduction band of K_3C_{60} with external hydrostatic pressure **(a)** and predicted scaling at the Fermi energy **(b)** at room temperature. The vertical dashed line at 0 eV in panel **(a)** indicates the Fermi energy, while the one in panel **(b)** is the result of a linear fit. Figure adapted from [102].

5.1.1   Metallic response of K_3C_{60} under pressure

The response of equilibrium metallic K_3C_{60} has been investigated under external hydrostatic pressure. The sizeable increase of the electronic bandwidth, due to the smaller C_{60} ball-to-ball distance, corresponds to a change in the tunneling rate of the conducting electrons, affecting thus the resistivity, i.e. the DC conductivity of the system.

Potassium doped fullerides are characterised by a zero-frequency resistivity which scales with temperature following a rather conventional T^2-law valid for metals, and thus decreases for smaller temperatures [110].

A reduction of the resistivity is also expected to follow any volume contraction obtained either by doping or by means of external pressure. The chemical substitution from rubidium to potassium atoms in A_3C_{60}, induces indeed a reduction of the resistivity by almost a factor of 2. Additionally, the resistivity of Rb_3C_{60}, which is expected to react similarly to K_3C_{60}, has also been fully characterised in the presence of external hydrostatic pressure and it decreases exponentially for smaller unit cells [110].

The same qualitative trend has been confirmed by optical measurements on single crystals of K_3C_{60} and Rb_3C_{60}. By means of far-infrared spectroscopy, the real part of the optical conductivity has been measured for both materials

at ambient pressure. The extrapolated value of the zero-frequency conductivity of the expanded Rb_3C_{60} is smaller than the one of K_3C_{60} [70].

Additional measurements of the optical properties of powders of potassium doped fullerides confirmed that the DC conductivity under pressure increases, as discussed previously in Chapter 2 [24].

As in most conventional metals, the response of K_3C_{60} above its critical temperature is thus strengthened by means of external pressure.

5.1.2 Superconducting response of K_3C_{60} under pressure

The equilibrium superconducting phase of K_3C_{60} is strongly quenched by external pressure, as the electronic density of states at the Fermi energy is directly related to the superconducting critical temperature. According to the weak-coupling BCS theory, T_c is expressed by

$$k_B T_c = 1.13 \ \hbar\omega_D \ e^{-\frac{1}{\lambda}} \tag{5.1}$$

where ω_D is the Debye frequency, $\lambda = N(E_F)V_{\text{eff}}$ with V_{eff} is the effective interaction between the electrons mediated by the electron-phonon coupling [111]. To fully predict the effect of pressure on the superconducting state, the scaling of both $N(E_F)$ and of the interaction term must be known. A reduction of the electron phonon coupling λ will cause a drop of the critical temperature T_c.

A strong suppression of T_c with external hydrostatic pressure has been experimentally observed by means of x-ray scattering measurements combined with susceptibility ones [103, 69]. Figure 5.3(a) reports the measured reduction of lattice parameter a as a function of external pressure measured on K_3C_{60} at room temperature [69]. The grey dashed line in the figure is a linear fit of the data, which nicely approximate the $a(P)$ relation.

Interestingly, a linear dependence has been measured also in the scaling of the superconducting critical temperature as a function of pressure $T_c(P)$, and thus lattice parameter, as shown in Fig. 5.3(b). This finding implies that
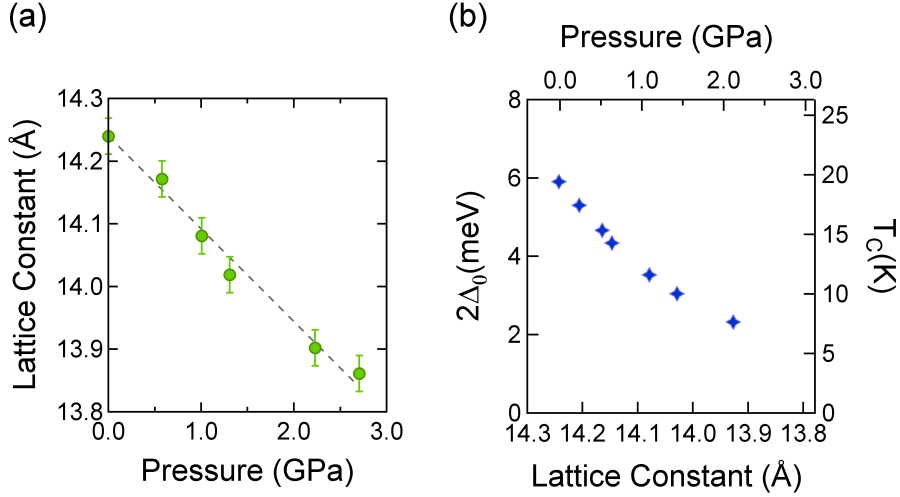
Figure 5.3: **(a)** Reduction of the lattice parameter as a function of pressure measured with x-ray scattering. The grey dashed line in a linear fit of the data. [69]. **(b)** Superconducting transition temperature T_c and optical gap size retrieved from the BCS formula $2\Delta_0/k_BT = 3.52$ [61], plotted as a function of lattice parameter and external pressure. Data adapted from Ref. [103].

the dependency dT_c/dP (of about -7.8 K/GPa [103]) is mostly dominated by the linear compressibility as $[dT_c/da] \cdot [da/dP]$. Within the BCS weak-coupling limit for which Eq. 5.1 holds, the observed linear dependence of $T_c(P)$ can only be explained in terms of linear approximations of $T_c(P)$ and $a(P)$, within the pressure range shown.

Any phonon hardening and alteration of the effective electronic interaction induced by pressure would require, on the other hand, pressures higher than 3 GPa [111], and their contribution to the $T_c(P)$ relation in the considered pressure range can be, in first approximation, neglected [69].

Figure 5.3**(b)** additionally shows the value of the optical gap as a function of pressure, recalculated from the BCS relation $2\Delta_0/k_BT = 3.52$, which holds for K_3C_{60} [61, 70]. As expected from the BCS theory the optical gap size decreases with pressure, and its evolution can be nicely tracked by means of the optical response of the system. At a finite temperature $T < T_c$, the reduction of the gap size will be in fact accompanied by a gradual filling of the gapped area in the real optical conductivity spectrum $\sigma_1(\omega)$ and by a

less pronounced divergence of the imaginary $\sigma_2(\omega)$ (see Chapter 3).

5.2 Pressure tuning of the out-of-equilibrium phase of K$_3$C$_{60}$

The excitation of metallic K$_3$C$_{60}$ ($T > T_c$) with ultrashort sub-ps mid-infrared pulses unveils the existence of a transient state compatible with a transient superconductor, with a lifetime of few ps. The optical response of the photo-excited state is characterised by 100% reflectivity below a cut-off frequency of about 10 meV, and by the formation of an optical gap in the real conductivity spectrum $\sigma_1(\omega)$ and by a strong coherent response in the imaginary $\sigma_2(\omega)$.
While the sample at low temperature (20 K and 100 K) is highly photo-susceptible and the out-of-equilibrium optical response is almost saturated, at 200 K and 300 K the effect is reduced and the optical spectra become compatible not only with a finite temperature superconducting model, but also with one for a metal with an enhanced mobility of carriers with respect to the equilibrium (see Chapter 4).
Optical measurements alone do not constitute a proof for superconductivity, as the response of a perfect metal will coincide with the one of a finite lifetime superconductor (See Chapter 3). It is then possible to integrate infrared optical measurements to additional external perturbations and observe the evolution of the optical response. Due to the relevance of pressure for K$_3$C$_{60}$ at equilibrium, which triggers different and opposite behaviours based on the specific starting ground state, the superconducting-like response has been studied in the presence of external hydrostatic pressure.
As previously discussed, hydrostatic pressure mainly affects the electronic band structure of samples of K$_3$C$_{60}$, hence altering the starting conditions for the pump-probe experiment. The experimental investigation of the scaling of the superconducting-like transient state within the low-pressure range could provide a more unequivocal and satisfactory interpretation of this state.

5.2.1   Experimental results

External pressure has been applied on powders of K_3C_{60} by means of a membrane diamond anvil cell (DAC), see Appendix D. To guarantee alignment stability over the entire measurement, an inflatable membrane has been used to apply force to the piston [24]. The sample was pelletised in an oxygen free environment (< 0.1 ppm) to prevent any deterioration (see Appendix A).

To combine THz-TDS and high-pressure, the size of the culet of the anvils has been chosen such that clean THz spectra could be measure, but that still relatively high pressures could be reached (see Appendix C and D).

The diamonds chosen, type IIac, have a culet of 2 mm diameter, that compact the powders of K_3C_{60} confined in a hole of 1.1 mm diameter drilled into a pre-indented Cu gasket (thickness 100 μm). No hydrostatic medium has been used in the loading since up the measured pressure, isotropy was provided by the granular sample itself. The whole assembly has been mounted on a cryostat, allowing for a fine temperature control down to 100 K. The shift of the fluorescence lines of the R1 and R2 levels of rubies loaded inside the powder has been used as an *in-situ* pressure gauge, after having calibrated their thermal drift contribution [85, 84] (see Appendix D).

Unfortunately no data from the superconducting state under pressure could be recorded, given the abrupt reduction of the equilibrium T_c and the limited base temperature of the implemented assembly.

K_3C_{60} has been excited by strong MIR pulses tuned to 170 meV, at resonance with the infrared active $T_{1u}(4)$ phonon. Broadband (5 - 31 meV) and narrowband (3 - 11 meV) THz pulses were used to characterise the low-energy response under pressure. Multiple data sets were combined to achieve a finer pressure dependence, as the initial pressure after each sample loading can only be coarsely controlled through the cell assembly. The additional thermal contraction of the cell during thermal cycles couldn't be finely controlled and the effective pressure, especially at low temperatures, couldn't be easily tuned to very low values.

Figure 5.4(a) displays the narrowband THz electric field reflected by the unperturbed sample at 100 K (red line) measured with THz-TDS, and its
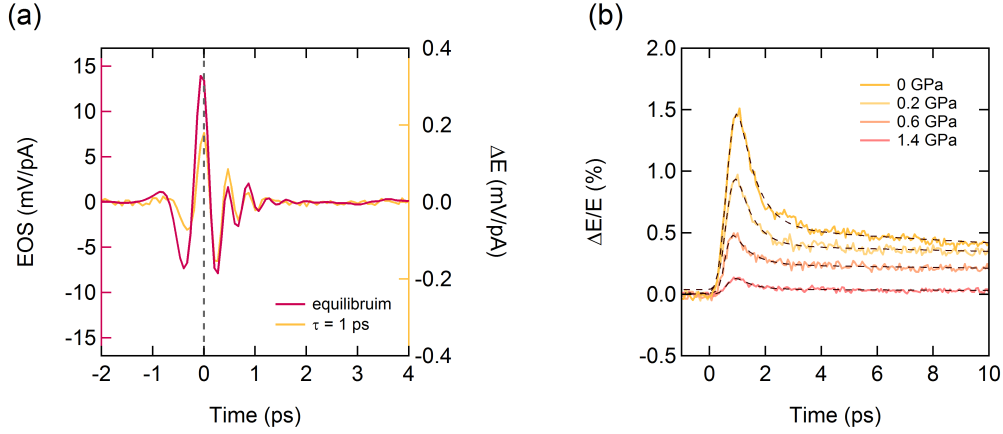
Figure 5.4: **(a)** Reflected THz pulse (red curve) and its relative pump-probe changes (yellow curve) induced 1 ps after the excitation on K_3C_{60} pumped at 100 K, at 0.2 GPa. **(b)** Temporal evolution of the peak of the reflected electric field (identified by the dashed line in panel **(a)**), measured with a pump fluence of 3 mJ/cm^2 for selected values of pressure. The dark dashed line are the result of a double exponential fit.

relative light-induced changes, 1 ps after the excitation at the smallest pressure of 0.2 GPa (yellow curve), at a constant fluence of about 3 mJ/cm^2. In the same way as for the ambient pressure measurements, the photo-induced changes are *in-phase* with the static THz pulse, and the averaged response, measured at 0 ps (vertical dark dashed line), is positive. In panel **(b)** the averaged frequency responses of K_3C_{60} for increasing values of pressure are reported. Independent of the specific value of the external pressure, the light-induced reflectivity changes are always positive and can be fitted with a double exponential decay with relaxation time constants $\tau_1 \simeq 1$ ps and $\tau_2 \gg 10$ ps, comparable to the ones found for the ambient pressure data. The risetime of the dynamics is limited to the temporal resolution of the experiment (300 fs), as described in Appendix C .

Figure 5.5 displays snapshots of the measured optical reflectivity $R(\omega)$ at the sample-diamond interface, along with complex conductivity spectra $\sigma_1(\omega)$ and $\sigma_2(\omega)$, 1 ps after the excitation, for different values of static pressure. Energies below 6 meV have been ignored in order not to consider spurious contribution in the reflected THz pulse not impinging only to the sample, as
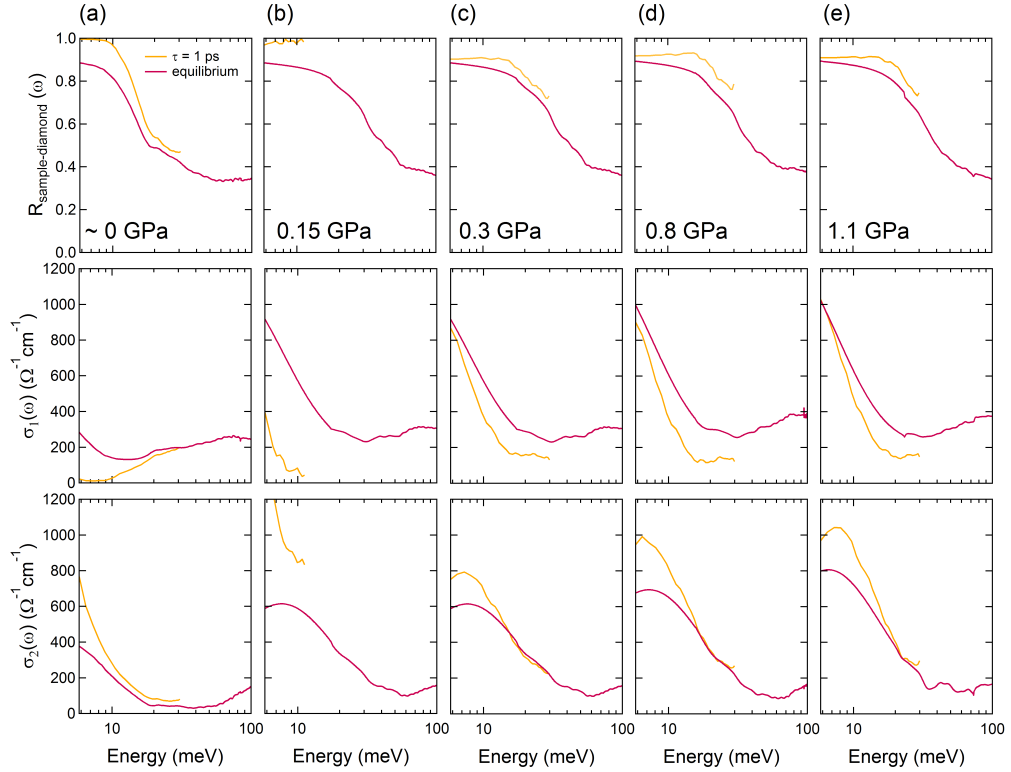
Figure 5.5: Pressure dependence of the transient optical properties of K_3C_{60} at 100K. Reflectivity (sample-diamond interface) and complex optical conductivity of K_3C_{60} measured at equilibrium (red) and 1 ps after photo-excitation (yellow), for different external pressures. The data in **(b)** have been measured using a probe pulse with narrower bandwidth. All data were taken with the same pump fluence of 3 mJ/cm^2 [24].

below this frequency the THz spot size is bigger than the sample (See Appendices C and D). In each panel, the red and yellow curves are the optical properties of the equilibrium metal, and those of the non-equilibrium state induced by photo-excitation, respectively. Panel **(a)** reports the response of K_3C_{60} at ambient pressure characterised by the same features discussed in the previous chapter. For P = 0.15 GPa (panel **(b)**, measured only with narrow THz spectra), the transient optical response is still pronounced, the reflectivity is saturated $R(\omega) = 1$, $\sigma_1(\omega)$ is gapped and $\sigma_2(\omega)$ diverges towards low energies. However, spectral weight fills $\sigma_1(\omega)$ at the lower edge of the displayed region. For larger pressures (Fig. 5.5**(c)**-**(e)**), a strong suppres-

sion of the light-induced changes in the optical response is observed. Above 0.3 GPa the enhancement in the reflectivity is clearly less pronounced, and a progressively broader Drude peak appears in the low energy conductivity. The finite-frequency peak in the imaginary conductivity quantifies the onset of a finite scattering rate.

The reduction in light-induced coherence observed for pressures smaller than 0.3 GPa does not follow the expected behaviour of a photo-excited metallic state, where the lattice compression is known to be associated to larger electronic bandwidth, smaller effective mass and thus larger mobility (i.e. higher plasma frequency ω_P). On the other hand those data seem to support the interpretation of the out of equilibrium state as a superconducting-like one [24].

Further insights can be obtained from the observation of the pressure dependence at different base temperatures.

Temperature dependence

The effect of external pressure on the photo-susceptibility of K_3C_{60} has also been investigated at higher temperatures. Figures 5.6 and 5.7 summarise the optical response of photo-excited potassium fullerides 1 ps after the MIR excitation for different pressure values, at 200 K and 300 K respectively, while the pump fluence has been kept constant (3 mJ/cm^2).

For both temperatures, the ambient pressure response (panel **(a)**) shows a partially formed light-induced gap in $\sigma_1(\omega)$, accompanied by a low-frequency divergence in $\sigma_2(\omega)$. On the other hand, all data taken at a finite pressure ($P \geq 0.2$ GPa) display moderate photo-induced changes and the measured transient conductivity is that of a metal with slightly enhanced carrier mobility (narrower Drude peak). Interestingly for even higher pressures, above 0.6 GPa, the light-induced changes in the optical response become more pronounced.

The complete overview of the scaling of the light-induced state as a function

Figure 5.6: Pressure dependence of the transient optical properties of K_3C_{60} at 200K. Reflectivity (sample-diamond interface) and complex optical conductivity of K_3C_{60} measured at equilibrium (red) and 1 ps after photo-excitation (yellow), for different external pressures. All data were taken with the same pump fluence of 3 mJ/cm^2 [24].

of external pressure at different temperature can be obtained by plotting the fractional spectral weight loss of the real conductivity spectrum at the peak of the transient response, 1 ps after the excitation (SWL_{1ps}).

The depleted spectrum of $\sigma_1(\omega)$ has been integrated from 5.3 meV and 11.6 meV, according Eq. 4.2, in order to be able to use both the narrow and broad THz probe data. The summary of the temperature and pressure dependence is plotted in Fig. 5.8 for 100 K **(a)**, 200 K **(b)** and 300 K **(c)**. Overall, the light-induced effect scales with pressure following two distinctive trends: for moderate values, it first rapidly decays (light blue dashed area), while it shows an almost pressure-independent trend above a certain threshold (green shaded area), which is smaller for increasing base temperature.

A simultaneous fit of the optical reflectivity at the sample-diamond interface
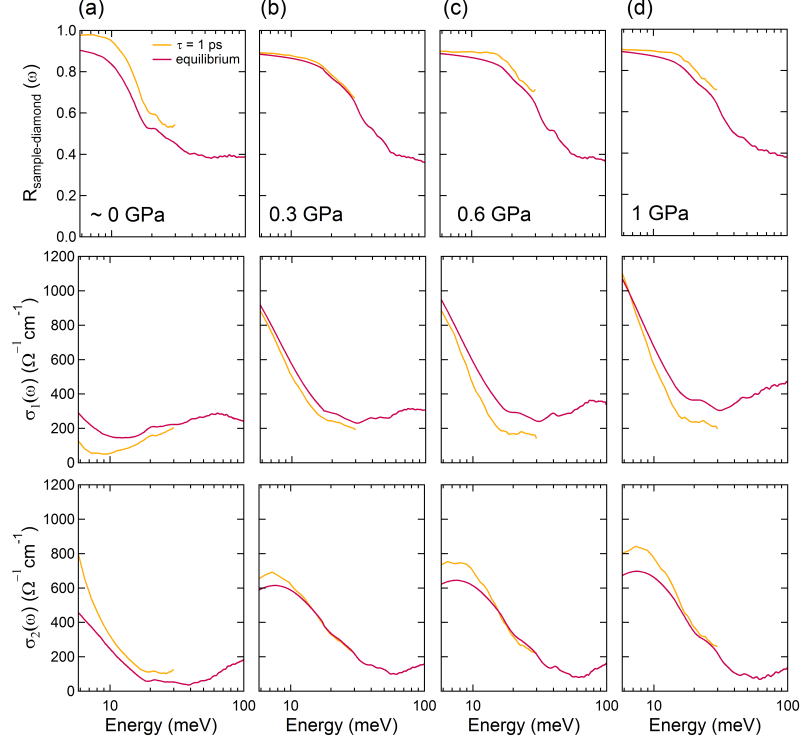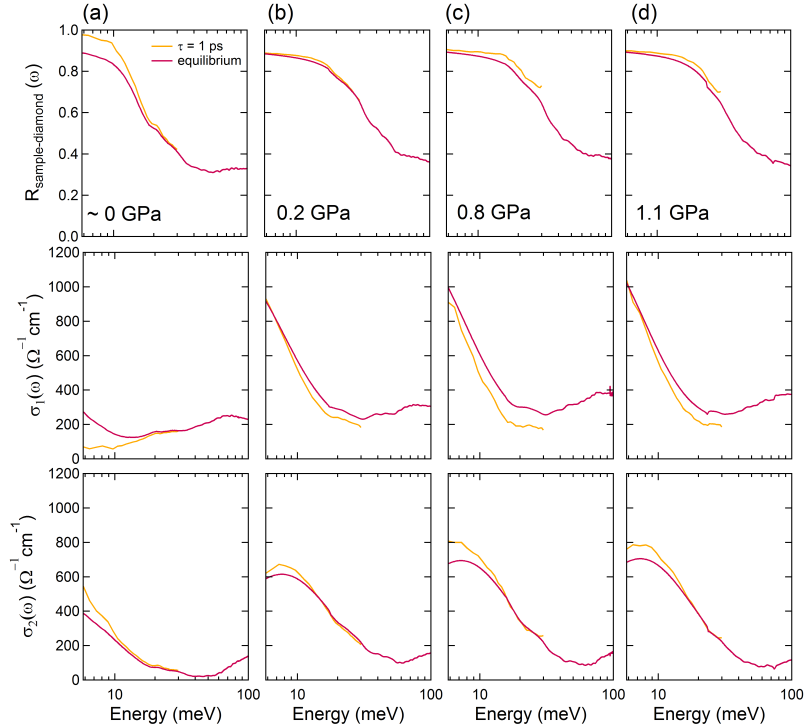
Figure 5.7: Pressure dependence of the transient optical properties of K_3C_{60} at 300 K. Reflectivity (sample-diamond interface) and complex optical conductivity of K_3C_{60} measured at equilibrium (red) and 1 ps after photo-excitation (yellow), for different external pressures. All data were taken with the same pump fluence of 3 mJ/cm^2 [24].

and of the real and imaginary part of the optical conductivity has been run on the measured data at all temperatures and pressures, 1 ps after the MIR excitation. The transient optical properties of K_3C_{60} under pressure were modelled at all measured temperatures and pressures using the same Drude-Lorentz model employed to fit the ambient pressure transient and equilibrium response (see Eq. 3.5). The advantage of this model is that it captures both the transient superconducting-like state in the limit of infinite scattering time ($\tau \to \infty$) and the one of a metal, and thus the possible transition from the former to the latter.

Figure 5.9 displays representative fits to the transient and the equilibrium optical response of K_3C_{60} at 100 K. The Drude parameters extracted from the fit are summarised in Table 5.1 for the three temperatures and their pressure

Figure 5.8: Scaling of the $\sigma_1(\omega)$ gap with external pressure at 100 K (**a**), 200 K (**b**) and 300 K (**c**). Photo-induced reduction in $\sigma_1(\omega)$ spectral weight, integrated in the gap region between 5.3 meV to 11.6 meV, normalised by the equilibrium value (integrated in the same range). Yellow and orange circles refer to data sets taken with pro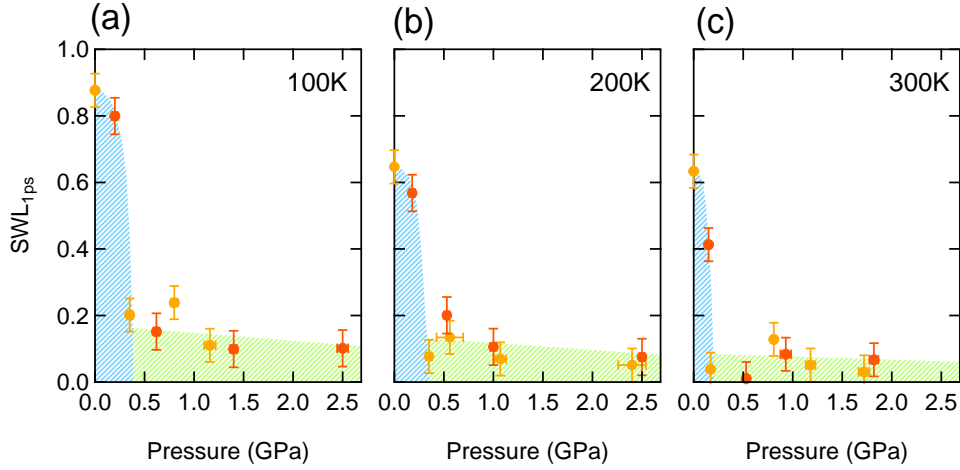be pulses with broader and narrower bandwidth, respectively. The light blue shaded areas identify the regions in which a photo-induced conductivity gapping is measured ($SWL_{1ps} > 0.5$). Those in green instead refer to the regime where no gapping was observed ($SWL_{1ps} < 0.5$). All data were taken with the same pump fluence of 3 mJ/cm^2 [24].

dependence, together with the extracted value of the zero frequency conductivity defined as $\sigma_0 = \omega_{Dp}^2 \tau / 4\pi$. The central frequency of the Lorentzian accounting for the polaronic band, its weight and damping terms were kept constant since they do not influence the free-carrier Drude parameters. Different parameters for the polaronic band were in fact tested to prove the solidity of the used fitting procedure, and no consistent differences on the final Drude properties have been found. The extracted values of σ_0 evolve from infinite to finite values as expected from the transition from a conventional metal to a perfect conductor.

The zero-frequency conductivity of the photo-excited state is plotted as a function of applied pressure, for all the temperatures in Fig. 5.10, together with the values obtained from the fit of the static curves. The equilibrium metallic conductivity (green squares) increases linearly with applied pressure with a less pronounced slope for increasing temperature. The transient
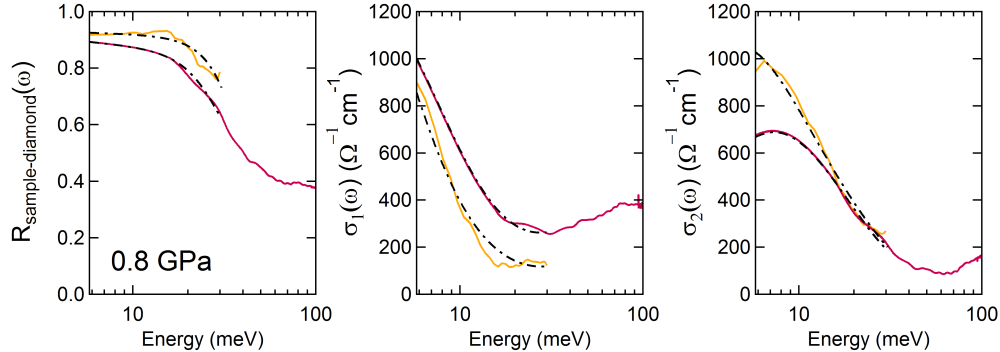
Figure 5.9: Drude-Lorentz fits to the transient and equilibrium optical response under pressure at 100K. Reflectivity at the sample-diamond interface and complex optical conductivity of K_3C_{60} measured at equilibrium (red) and 1 ps after photoexcitation (yellow) at P = 0.8 GPa. [24].

conductivity, measured with the broad (yellow circles) and narrow (orange circles) THz probe pulses, scales instead not monotonically with pressure. At all temperatures, in the same way as for the spectrally integrated weight loss of the real conductivity response, σ_0 is firstly reduced by external pressure ($d\sigma_0/dP < 0$, light blue dashed area), and above 0.3 GPa starts to increase ($d\sigma_0/dP > 0$, green dashed area).

The two different trends of the light-induced state add crucial information to the overall picture. At low pressures, the photo-excited state has clear superconducting-like pressure dependence, being $d\sigma_0/dP < 0$, and the fact that the equilibrium superconductor is quenched by pressure supports this interpretation. On the other hand, for higher pressures ($P > 0.3$ GPa) the transient response is clearly metallic-like, with $d\sigma_0/dP > 0$, and the conductivity enhancement induced by means of infrared radiation is pressure independent. The σ_0 of the photo-excited state in this second regime follows indeed the dependence of the equilibrium metal.

From the comparison of the response of photo-excited K_3C_{60} to external pressure at the different temperatures plotted in Fig. 5.10**(a-c)** one observes that the critical pressure value at which the light-induced response switches from the one of a transient superconductor to the one of a metal, reduces in the warmer samples. Interestingly, contrary to what was inferred from the ambi-
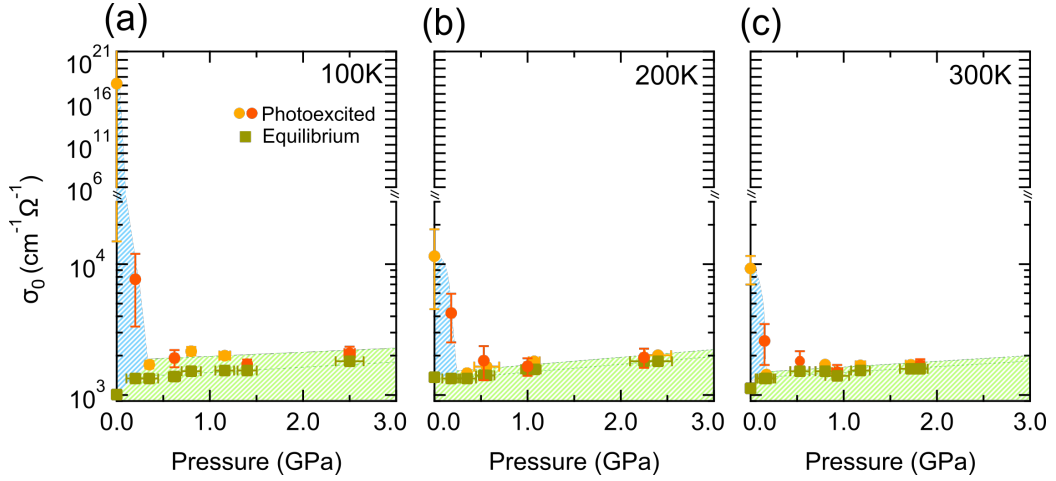
Figure 5.10: Pressure dependence of the extrapolated conductivity $\sigma_0(P)$ resulting from Drude-Lorentz fits of the experimental data as a function of pressure, plotted for three different temperatures: 100 K **(a)**, 200 K **(b)** and 300 K **(c)**. Yellow and orange circles refer to data sets taken with probe pulses with broader and narrower bandwidth, respectively. The green squares are the corresponding zero-frequency conductivities determined at equilibrium. The light blue areas identify the regions in which the transient σ_0 is suppressed by pressure ($d\sigma_0/dP < 0$) while those in green indicate the regime in which $d\sigma_0/dP > 0$. All data were taken with the same pump fluence of 3 mJ/cm^2 [24].

ent pressure measurements alone, the data at 200 K and 300 K also show the same pressure dependence as the data at 100 K. The former interpretation of the optical response of K_3C_{60} at those temperatures, which allowed for the possibility of a light-induced high-mobility metal now seems less likely. Up to room temperature, potassium fullerides in fact react to mid-infrared excitation in the same way as at 20 K, but with a lower photo-susceptibility.

5.3   Considerations on the effect of pressure on the superconducting-like state of K_3C_{60}

The most striking aspect of the pressure dependence of the superconducting-like response of K_3C_{60} is its quick suppression which happens for external

T (K)	P (GPa)	σ_0 ($\Omega^{-1}cm^{-1}$)	ω_{Dp} (meV)	γ_D (meV)
100	0 ± 0	$10^{18} \pm 10^{13}$	183 ± 62	0 ± 0.13
100*	0.20 ± 0.03	7667 ± 4172	260 ± 22	1.16 ± 0.62
100	0.35 ± 0.03	1702 ± 73	264 ± 3	5.49 ± 0.22
100*	0.62 ± 0.03	1917 ± 285	282 ± 6	5.6 ± 0.8
100	0.80 ± 0.04	2159 ± 145	274 ± 3	4.7 ± 0.3
100	1.16 ± 0.06	1999 ± 81	292 ± 3	5.71 ± 0.25
100*	1.40 ± 0.04	1722 ± 137	293 ± 4	6.69 ± 0.53
100*	2.5 ± 0.06	2091 ± 253	308 ± 6	6.11 ± 0.7
100	3.2 ± 0.05	2276 ± 137	306 ± 4	5.54 ± 0.34

T (K)	P (GPa)	σ_0 ($\Omega^{-1}cm^{-1}$)	ω_{Dp} (meV)	γ_D (meV)
200	0 ± 0	11499 ± 5902	184 ± 2	0.39 ± 0.24
200*	0.18 ± 0.03	4235 ± 1560	270 ± 19	2.35 ± 0.89
200	0.35 ± 0.03	1470 ± 24	276 ± 1	6.97 ± 0.14
200*	0.53 ± 0.03	1829 ± 378	270 ± 7	5 ± 1
200	0.56 ± 0.13	1647 ± 65	272 ± 3	6.05 ± 0.22
200*	1.00 ± 0.03	1658 ± 236	300 ± 10	7.15 ± 0.99
200	1.07 ± 0.06	1808 ± 72	300 ± 4	6.68 ± 0.29
200*	2.25 ± 0.03	1938 ± 303	310 ± 10	7 ± 1
200	2.40 ± 0.14	2013 ± 74	310 ± 3	6.41 ± 0.26

T (K)	P (GPa)	σ_0 ($\Omega^{-1}cm^{-1}$)	ω_{Dp} (meV)	γ_D (meV)
300	0 ± 0	9276 ± 2403	$162.6 \pm .8$	3.09 ± 0.81
300*	0.15 ± 0.02	2591 ± 687	260 ± 8	3.49 ± 0.93
300	0.17 ± 0.01	1434 ± 28	281 ± 2	7.39 ± 0.17
300*	0.53 ± 0.02	1814 ± 316	300 ± 15	7 ± 1
300	0.80 ± 0.02	1709 ± 37	280 ± 2	6.17 ± 0.18
300*	0.93 ± 0.06	1494 ± 212	281 ± 9	7.12 ± 0.90
300	1.18 ± 0.05	1685 ± 33	296 ± 2	6.98 ± 0.17
300	1.72 ± 0.05	1700 ± 26	305 ± 1	7.34 ± 0.15
300*	1.82 ± 0.04	1686 ± 214	299 ± 9	7.14 ± 0.83

Table 5.1: Parameters extracted from Drude-Lorentz fits to the transient optical response functions of K_3C_{60} measured at different temperatures and pressures. The plasma frequency ω_{Dp}, Drude scattering rate γ_D, and extracted DC conductivity σ_0 are displayed. The pressure values are extracted by fits of the ruby fluorescence line, as explained in Refs. [85, 84]. Entries in the table marked with * refer to data taken using the setup with reduced probe bandwidth [24].

pressure values much lower than then ones needed at equilibrium ($\sim$ 0.3 GPa vs $\sim$ 3 GPa). This enhanced responsiveness may result from the fact that as soon as pressure is applied, more energy is added to the system and stronger fluctuations detrimental for transient superconductivity might be induced.

The resonant excitation of K$_3$C$_{60}$ under pressure highlights additional properties of the superconducting-like gap induced transiently in K$_3$C$_{60}$. First, the size out-of-equilibrium 2Δ doesn't scale either with temperature, nor with mid infrared pump fluence, as described in Chapter 4 [23]. While the former behaviour is found also in the equilibrium temperature dependence of superconducting gap, unveiling the limits of the BCS model for the fullerides superconductor (see Chapter 3), the absence of a clear evolution with pump fluence is fairly interesting. For fluences higher than a specific critical value the effect seems to be saturated, i.e. the depletion in the $\sigma_1(\omega)$ spectrum is almost complete below $\sim$ 11 meV, while for low pump fluences the same spectral region is reshaped, but the gap is not completely opened.

The same anomalous behaviour is found in the superconducting like response of K$_3$C$_{60}$ as a function of pressure. Under the critical pressure value of $\sim$ 0.3 GPa at 100 K, 2Δ is in fact not becoming smaller, but evolving from the characteristic flat shape of the superconductor at ambient pressure back to the conventional Drude curvature.

Additionally, the study of the pressure dependence of the superconducting-like phase of K$_3$C$_{60}$ highlights that the nature of the light-induced state is the same at all the measured temperature, suggesting that some incipient features of transient superconductivity may already be present up to room temperature. In the absence of stronger MIR sources, it is however not possible to obtain a fully gapped state at 300 K characterised by infinite zero-frequency conductivity. Understanding whether light can overcome thermal electronic fluctuations hence remains an open question.

All these observations also provide guidance for a microscopic explanation of the results. One finds a very strong dependence of the light-induced optical conductivity on low pressure values, while at higher pressures (smaller lattice constants) the metallic phase is stabilised. This is compatible with

the interpretation reported in Chapter 4, in which the excitation of the mid-infrared phonon couples to the electronic properties of the system [77, 98, 99, 101, 112]. The dramatic dependence on the electronic bandwidth on pressure does not, on the other hand, support the explanation of the transient state based on quasi-particle cooling, which would require a strong reshaping of the polaronic feature which is needed in this picture [113].

All these experimental observations add interesting perspective of optimising light-induced superconductivity, and point towards the future investigation of the A_3C_{60} compounds with larger lattice spacing.

5.4 Summary

Alkali doped fullerides are extremely sensitive to the application of external hydrostatic pressure since their intermolecular bonds are mostly dominated by weak Van der Waals forces. While metallic K_3C_{60} at equilibrium is strengthened by pressure, i.e. its electronic mobility is enhanced, the equilibrium superconductor is quickly quenched already for pressure values of 3 GPa.

The same opposite trends of the response to pressure are expected to discriminate the nature of the MIR-driven phase found in K_3C_{60} above its critical temperature. Pressure dependent optical spectra of the transient state have been measured by means of a diamond anvil cell (DAC) integrated with a THz-TDS setup.

At all the measured temperatures ($T \geq 100$ K), the transient response quickly decays as pressure is applied. Already at 0.5 GPa the light-induced state is characterised by a response which can be unequivocally interpreted as the one of a metal, with a finite zero frequency conductivity and a finite scattering rate of the Drude electrons. For even higher pressure values the conductivity increases following the behaviour of the equilibrium metal, and the superconducting-like behaviour is never recovered.

The strong quenching of the superconducting-like response supports the former interpretation of the light-induced phase as a transient superconductor, but additionally extend it also to temperatures as high as room temperature.

These findings support the microscopic explanation of the superconducting-like nature of the transient state of K_3C_{60} at ambient pressure in terms of a modulation of the electronic *on site* correlations and stimulate the extension of the analysis to other members of the family of alkali doped fullerides.

Conclusions and Outlook

Understanding how collective properties of complex materials emerge and dominate over diverse competing phases is probably the most stimulating challenge which scientists face everyday. The reason of the predominance of superconductivity over other broken-symmetry ground states has become a central theme in the physics of high-T_c superconductors, and a lot of effort has been put in trying to overstep the current physical barriers.

Structural degrees of freedom in conventional superconductors are known to have strong influence on the electronic pairing mechanism below the critical temperature. In this thesis this specific relation has been experimentally exploited for the case of the three-dimensional molecular organic superconductor potassium doped fullerides K_3C_{60}.

Mid infrared pulses have been used to resonantly excite local molecular modes of the C_{60} molecules with the aim of affecting the electronic properties of the material. At equilibrium potassium doped fullerides become superconducting below $T_c \sim 20$ K thanks to a molecular Jahn-Teller deformation which favours the formation of a low-spin state and electrons with the same momentum.

The striking emergence of a driven broken-symmetry superconducting-like phase from the metallic one has been probed lasting for few picoseconds after excitation, by means of THz-Time Domain Spectroscopy (THz-TDS). In spite of its finite lifetime, such photo-excited superconducting state appears

to be characterised by an at least doubled electron pairing strength, and to extend to temperatures higher than 100 K.

In a second experiment, the response of such photo-induced state to the application of an external hydrostatic pressure has been studied to investigate over its real nature. As K_3C_{60} is pressurised its responsiveness to photo-excitation abruptly drops and no coherence is found in the optical response, as expected from a conventional equilibrium superconductor.

Beyond the scientific results presented so far, the experiments reported in this thesis required a laborious technological advancement, in particular for the integration of high pressure elements with THz-TDS. Balancing the stringent requirements needed for the application of high external hydrostatic pressure with the long far-infrared wavelengths used to probe the sample requires in fact a series of compromises in both the fields, which have been pushed here to their limit. The realised setup allows for the acquisition of clear THz spectra up to pressures of ~ 3 GPa.

Different theoretical interpretation have been proposed to explain the emergence of the superconducting-like phase in K_3C_{60}. The starting point of all these works are the nonlinearities driven in the system by means of the strong ultrashort pulses through lattice distortions. The ions of the lattice are forced to large oscillatory motions which may result in net non-zero higher order couplings that extend beyond the structural deformations.

One possible explanation of the superconducting-like phase of K_3C_{60} postulates an effective indirect lattice displacement along the coordinate of the Raman active mode with same symmetry of the phonon involved in the electron-phonon coupling at equilibrium. Alternatively, the reported observations could be explained in terms of coupling between the modulation of the molecular structure and the electronic states. In both these scenarios the coherent electronic response measured is interpreted as a light-induced *electronic* broken symmetry state.

Potassium doped fullerides are the least correlated material of the family of A_3C_{60} and the results presented in this thesis obtained by means of optical vibrational control, are only the starting point for the investigation of dynamical effects and control of superconductivity in carbon-based materials.
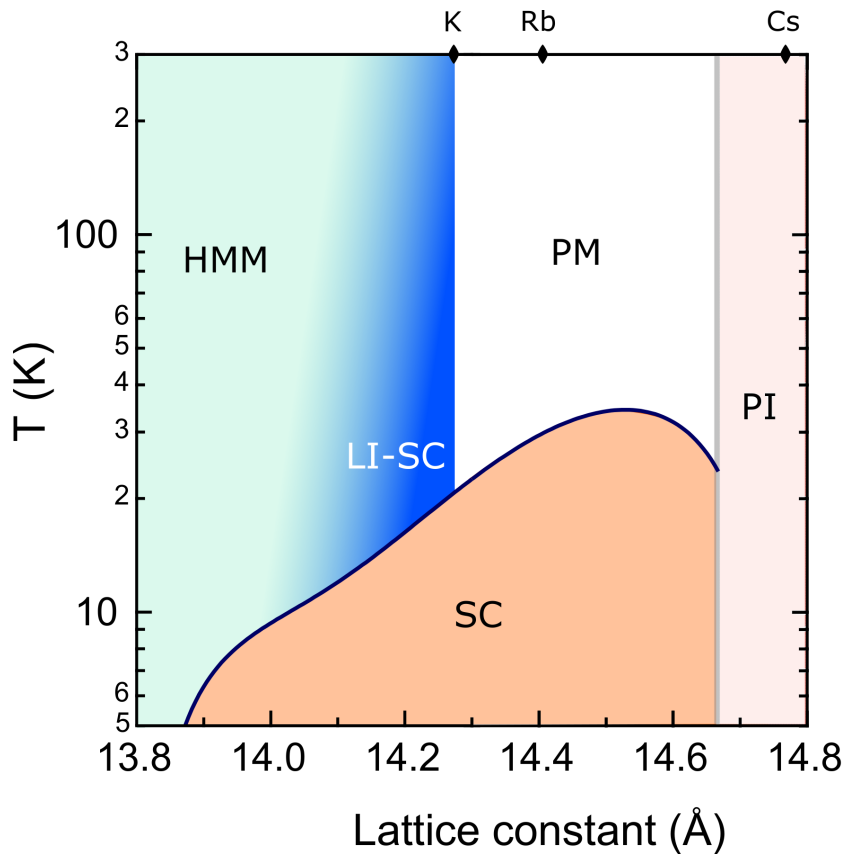
Figure 5.11: Schematic out-of-equilibrium phase diagrams for the three-dimensional alkali dope fullerides family A_3C_{60} as a function of lattice parameter. The dark blue line traces the equilibrium superconducting phase transition border for the equilibrium superconducting phase (SC, orange filled area). The dark blue shading stands for the transient Light-Induced Superconductor (LI-SC), which evolves into an High-Mobility Metal (HMM) under the application of pressure (light-green area). The black diamonds on the upper axis identify the equilibrium position of different doped fullerides, while PI, PM, and SC refer to the equilibrium paramagnetic insulating, paramagnetic metallic, and superconducting phase, respectively [76, 114, 115].

Exploring the response of the more correlated A_3C_{60} systems constitute a possible guide line for further experimental directions.

As electronic correlations become stronger, i.e. in Rb_3C_{60} and Cs_3C_{60}, the localisation of charges is favoured, over their mobility. Useful insights are expected to emerge from the observation of the response of such systems to the on-site resonant vibrational excitation, which will provide additional building blocks to be added to the current understanding of the observed phenomenon.

All discussed above could be summarised in a schematic representation of an attempted out-of-equilibrium phase diagram for the A_3C_{60} family under resonant photo-excitation. The equilibrium boundaries between the different phases, drawn in solid thick lines, are here plotted together with the recent findings of the light-induced superconducting-like state in K_3C_{60} (LI-SC, dark blue region). At glance this plot highlights that the light-induced superconducting phase quickly vanished with the lattice contraction in favour of an high mobility metallic phase (HMM, light blue region).

Transient data are still lacking in the expanded lattice region of this phase diagram, where at equilibrium the superconducting order is strengthened and result in an higher critical temperature T_c. Importantly the investigation of the expanded Cs_3C_{60} will further offer the possibility to observe the onset of such light-induced phase starting from an insulating phase, and eventually it will bring to light some of the most relevant ingredient for high temperature superconductivity.

A full investigation across the entire phase diagram by means of resonant optical mid-infrared excitation is expected to provide interesting insights of the optimisation of the light-induced superconductivity in these organic materials.

Appendices

Appendix A

A.1 Sample growth

Powders of C_{60} have been used in the low energy pump-probe experiment described in Chapter 3 and 4. The sample has been supplied from the Dipartimento di Scienze Matematiche, Fisiche e Informatiche, Università degli Studi di Parma, Italy, and its chemical purity has been characterised by means of powder X-ray diffraction and SQUID magnetometry. To prevent the sample from oxygen contamination, all the preparation was performed in an inert atmosphere (vacuum or Ar glove box with < 0.1 ppm of O_2 and H_2O).

Finely ground C_{60} powder and potassium metal, in stoichiometric amounts 1:3, were sealed in a cylindrical vessel and closed in a Pyrex vial under vacuum ($\sim$ 10-6 Torr). The potassium was kept separated from the fullerene powder during the thermal treatment, in this way only potassium vapours came in contact with C_{60}. Two thermal cycles were done on the two reagents, first at a temperature of 523 K for 72 h and then at 623 K for 28 h. The recovered black powder was then reground and pelletised. A further long annealing has been performed on the pellet by heating it to 623 K for 5 days.
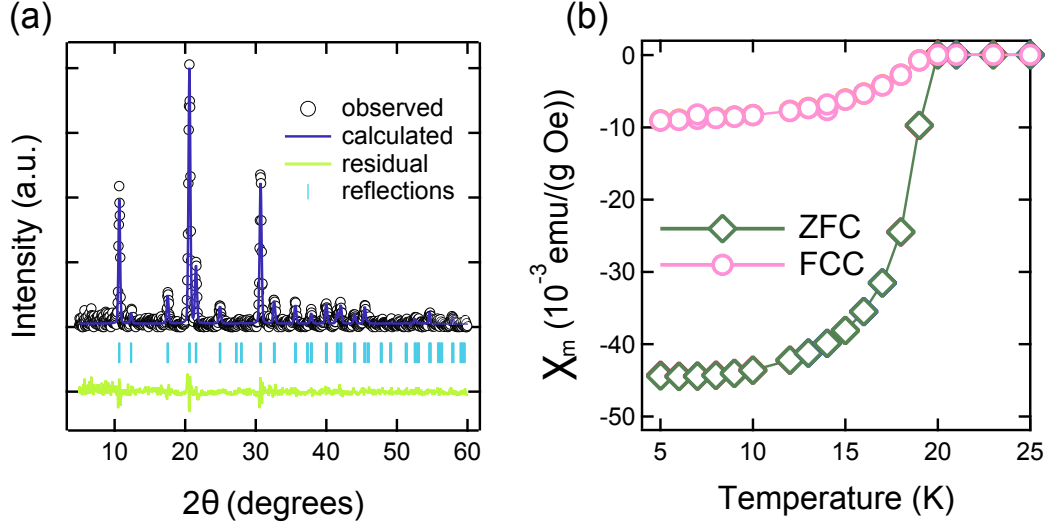
Figure A.1: **(a)** X-ray diffraction data for the powders of K$_3$C$_{60}$ used in this mid-infrared pump THz probe experiment, together with a single f.c.c. phase Rietveld refinement. **(b)** Temperature dependence of the sample magnetic susceptibility with and without magnetic field (FCC: Field cooled cooling. ZFC: Zero field cooling). Figure adapted from [24].

The final product, K$_3$C$_{60}$ showed an average grain size of 100-400 nm. Figure A.1**(a)** reports the experimental results of X-ray powder diffraction of the refined sample, which is in good agreement with previous observations [116]. A Rietveld refinement of the data with single phase f.c.c. K$_3$C$_{60}$ indicates complete phase purity within the experimental uncertainties. The width of the diffraction peaks has been used to extract the average size of the powder grains.

SQUID measurements were performed at zero (ZFC) and at 5 Oe (FCC) magnetic fields. The results of the temperature dependence of the DC magnetisation with and without the magnetic field are displayed in Fig. A.1**(b)**, in green and pink respectively. The critical temperature that can be extracted from these data is around 19.8 K in agreement with former literature findings [116, 117, 118], excluding the presence of defects in the sample ground state.
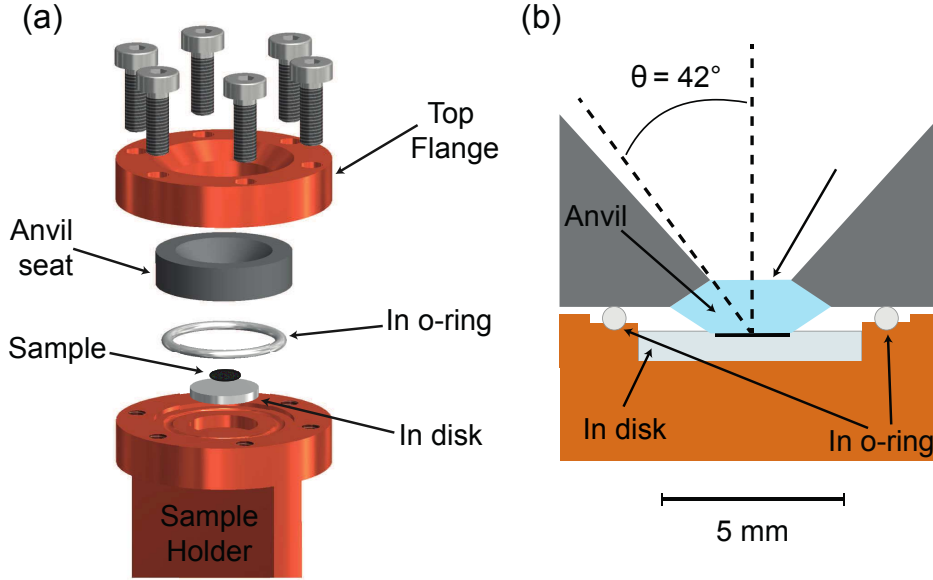
Figure A.2: Sample holder for MIR pump THz probe on K_3C_{60} at ambient pressure. In panel **(a)** all the mechanical components of the sample holder assembly are sketched. Panel **(b)** shows a side view of the sample compartment. The overall optical access is of $2\Theta \sim 85°$.

A.2 Sample handling

Due to the high reactivity of K_3C_{60} to the oxygen and water vapour contained in air [92, 93, 94], the loading and handling procedure for the experimental measurements reported in Chapter 2 and 4 had to be performed carefully in an inert atmosphere. Therefore, the sample has been prepared in an Argon atmosphere, with less than 1 ppm of Oxygen concentration, and with a percentage of $\sim 2\%$ of H_2O.

To prevent oxidation of the sample during the transport and installation in the experimental setup, the powders of K_3C_{60} have been pressed behind a transparent diamond window, and sealed by means of an Indium o-ring in a Copper holder. The used diamond is of type IIac and has a Böhler-Almax cut with an optical aperture of $2\Theta \sim 85°$, the diameter of the top is about 3.3 mm while the one of the culet of 2 mm. The anvil has been cut with 16 facet and it is 1.55 mm thick. A schematic view of the sample holder is displayed in Fig. A.2. To avoid external pressure onto the sample, the powders were

pressed from the diamond against a soft Indium disk.

The final sample of K_3C_{60} is then 2 mm wide, ~ 100 μm thick with a clean optical surface suitable for optical spectroscopy measurements.

The sample holder has then been mounted on the cold finger of an Oxford Optistat CF-V cryostat, which allowed cooling down to a few Kelvin.

A similar protocol has been followed for the loading of powders of K_3C_{60} in the Diamond Anvil Cell (DAC) described in Appendix D. The sample was directly loaded between the two anvils in a 1 mm diameter compartment drilled in a ~ 100 μm thick pre-indented Cu-gasket. A few rubies were additionally added on the side of the pellet, to be able to measure the local pressure. Once the DAC is sealed, no contamination of the sample is expected to happen.

Appendix B

Equilibrium infrared spectroscopy

The equilibrium response of powders of K_3C_{60} from the near infrared down to a few THz has been characterised by Fourier-transform infrared spectroscopy (FTIR), as reported in Chapter 3. Incoherent light delivered from a bulb source (FIR, MIR or NIR) is split and recombined to obtain an interferogram which impinges on the sample. The fast movement of one mirror in one of the two arms of the interferometer varies the pattern of the interferogram and allows the acquisition of broadband high-resolution spectra.

The data displayed in Chapter 3 have been measured at the solid state line SISSI of the Elettra Synchrotron, in Trieste by means of a Vertex 70 Interferometer [119]. An Hyperion 2000 microscope equipped with gold-coated Schwarzchild objectives (15x magnification, NA 0.4) is coupled to the system to allow a confinement of the long THz wavelengths down to few hundred microns. All spectra have been measured in reflection geometry. Commercial bulbs have been used to measure the reflectivity of powders of K_3C_{60} in the MIR and NIR spectral range (1000-10000 cm^{-1},$\sim$ 120-1200 meV), while the high brilliance of the Synchrotron radiation has been exploited to obtain high quality, low noise, far infrared spectra (40-1000 cm^{-1}, $\sim$ 5-120 meV). This setup has been used both for the measurement of the equilibrium re-
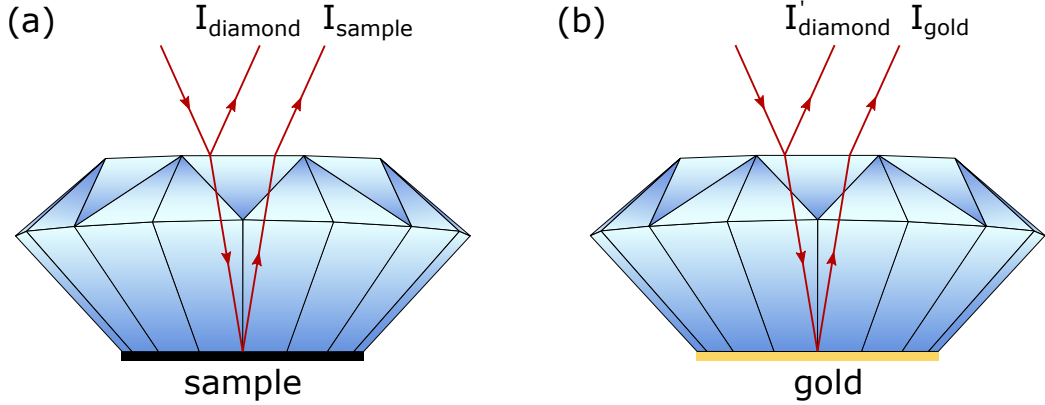
Figure B.1: K_3C_{60} absolute reflectivity retrieval behind a diamond window. In a first stage the intensity reflected from the sample I_{sample} is referenced to the one reflected from the first diamond interface $I_{diamond}$, panel **(a)**. By replacing the sample with a gold mirror, the same measurement provides the intensity reflected from the gold I_{gold} and from the same first diamond interface $I'_{diamond}$, panel **(b)**, used to retrieve the absolute value of the reflectivity.

sponse of K_3C_{60} at ambient pressure and under external hydrostatic pressure. In the former measurements, the spectra have been acquired from powders of K_3C_{60} sealed behind a diamond window in a sample holder described in A. To reach high pressure, powders of K_3C_{60} have been instead loaded in a Diamond Anvil Cell (DAC) together with a few ruby nanoparticles used to measure the effective pressure (see Appendix D).

In both cases the reflectivity spectra have been measured through a diamond window and the first diamond interface has been used to reference each reflected spectrum from the sample, as already described in literature [120]. In this step artefacts due to possible misalignment of the beam are removed. The reflection from a gold mirror, which is characterised by a $\sim 100\%$ featureless reflectivity up to ~ 8.5 eV has been used to retrieve the absolute value of each measured reflectivity curve. The gold mirror has been put behind the same diamond window and the intensity reflected from it and from the first diamond interface have been acquired in the same way as for the sample case, as represented in Fig. B.1. The final reflectivity of K_3C_{60} at the sample-diamond interface $R_{sample-diamond}$ has hence been referenced as

follows [120]:

$$R_{sample-diamond} = \frac{I_{sample}}{I_{diamond}} \cdot \frac{I'_{diamond}}{I_{gold}}. \tag{B.1}$$

This procedure has been used for all the reflectivity curves measured from powders of K_3C_{60}, at all the temperatures and pressures reported in Chapter 3.

In absence of transmission measurements, the reflectivity curves alone do not allow a direct reconstruction of the complex refractive index of the sample $N(\omega) = n(\omega) + k(\omega)$. A possible way around is offered by the Kramers-Kronig transformation, which allows the retrieval of the complex phase, given the spectral amplitude [79]. The full characterisation of the complex refractive index has thus been obtained by means of a Kramers-Kronig transformation through a transparent medium (the diamond), which considers the extra phase contribution introduced by the window itself [83]. To increase the reliability of the transformation, the measured data have been extrapolated up to visible range by means of literature data, as described in Chapter 3.

APPENDIX C

THz time resolved pump probe spectroscopy setup

The excitation with mid-infrared pulses tuned at resonance with the infrared active T_{1u} vibrational molecular mode in K_3C_{60} at ambient pressure unveils the existence of a superconducting-like transient phase that has been described and characterised in Chapter 4. In this appendix a detailed description of the experimental setup is given, for both the generation of intense ultrashort MIR pulses and the THz detection scheme.

C.1 Mid-infrared ultrashort pulses generation

The sub-picosecond strong mid-infrared pulses used in the experiment described in Chapter 4 and 5 have been obtained by difference frequency generation from two near infrared pulses generated as the output of a two-stage optical parametric amplifier (OPA) [121, 80]. The optical conversion scheme is pumped by the fundamental 800 nm light delivered from a conventional Ti:sapphire laser system, with a pulse duration of 100 fs, a 1 kHz repetition rate and 5 mJ of energy per pulse.

The optical parametric amplifier used is schematically shown in Fig. C.1. A
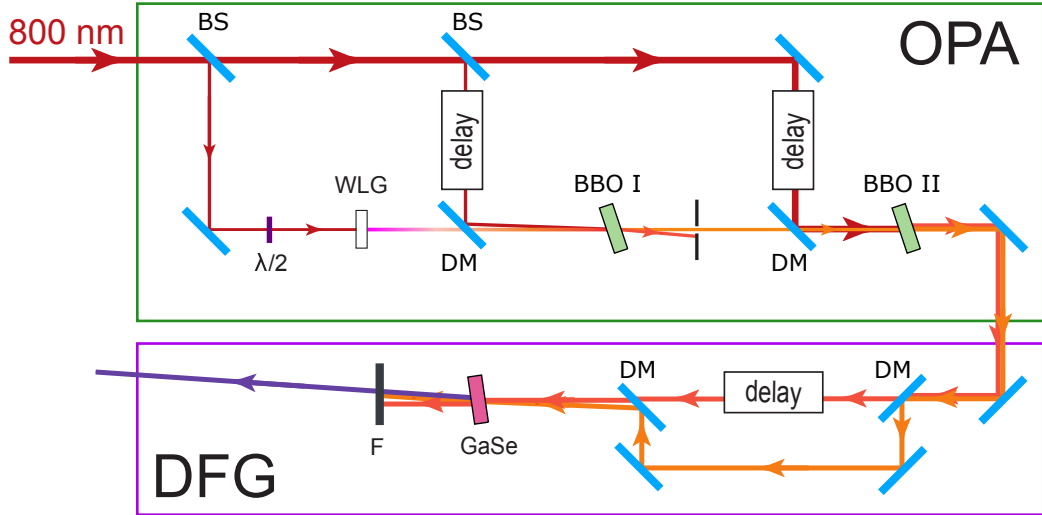
Figure C.1: Schematic representation of the double stage optical parametric amplifier (OPA) and the difference frequency generation setup (DFG) used to generate ultrashort MIR pulses. The 800 nm light is divided into the different stages of the OPA by means of beam splitters (BS) and the line thickness is roughly indicative of the beam intensity. WLG indicates the white light generation process in an Al_2O_3 crystal, DM are dichroic mirrors, BBO I and II are the amplification crystals used in the first and second stage respectively. The MIR generation is obtained in a GaSe crystal from the difference frequency of the NIR produced in the OPA. A final filter F is used to remove all the copropagating NIR contributions. Figure adapted from [122].

weak reflection of a few μJ of the 800 nm light is used to generate s-polarised white-light in a 2 mm thick Al_2O_3 crystal. Its visible content has been removed by means of a low pass filter, and the remaining near infrared light is used to seed the first amplification stage.

In this scheme the amplification crystals used are Type-II BBO crystals, cut at 28° to optimise the phase matching angle requirement for the amplification in the near infrared. The thickness of the crystals is such as to prevent any spectral broadening of the 800 nm pump, and is set to 3 mm and 2 mm for the first and second stage respectively.

The advantage of using a Type-II phase matching scheme, $e_{pump} \rightarrow e_{idler} + o_{signal}$, is multiple. First, it provides cross-polarised pulses, which can easily be divided for further manipulation. Second, in the chosen configuration, the

group velocity mismatch of signal and idler are opposite with respect to the pump, and thus the energy flow happens mostly in the direction from pump to signal and idler, resulting in a higher conversion efficiency of the parametric interaction. Finally Type-II phase matching provides a wider tuning range of the amplified beams [80].

In the first amplification stage, 175 μJ of pump are focussed down to 1.1 mm together with the infrared part of the white light whose spot has been accordingly matched. A small angle of about 1° between the two beams is held to allow the spacial filtering of the amplified signal used to seed the second stage. After the first nonlinear crystal $\sim 11\mu$J of s-polarised signal, centred at $\sim$1.44 μm, are obtained.

The signal of the first stage is then folded in a second collinear amplification stage together with 3.6 mJ of pump in a spot of about 4.4 mm. A total intensity of 1.8 mJ of amplified signal and idler is generated after the second nonlinear crystal. Figure C.2(a) reports representative spectra of the final signal and idler, tuned to $\sim$1.44 μm ($\sim$ 860 meV) and $\sim$1.8 μm ($\sim$ 690 meV) respectively. Both spectra have a bandwidth of less than 1% and a pulse duration of about 70 fs measured with a second harmonic FROG (SH-FROG) setup (group delay dispersion (GDD) of ~ 1000 fs^2, and third order dispersion (TOD) of ~ 2500 fs^3, see Fig.C.2(b)).

The NIR pulses are then recombined in a 1 mm z-cut GaAs nonlinear crystal as shown in the DFG block of Fig. C.1, to obtain MIR pulses. The crystal has been set to a Type II phase matching condition to obtain s-polarised mid-infrared pulses.

The MIR pulses were characterised by means of linear interferometry which revealed information about its spectral content, while crosscorrelation with 800 nm light has been used to determine the pulse duration. In Fig. C.3 a set of MIR spectra tuned over the entire phase matching bandwidth allowed by the setup is reported, together with a crosscorrelation measurement revealing a pulse length of less than 300 fs. Those pulses are the ones used in the wavelength dependence described in Chapter 4, where the pump photon energy was set roughly from 75 to 200 meV (6-16 μm).
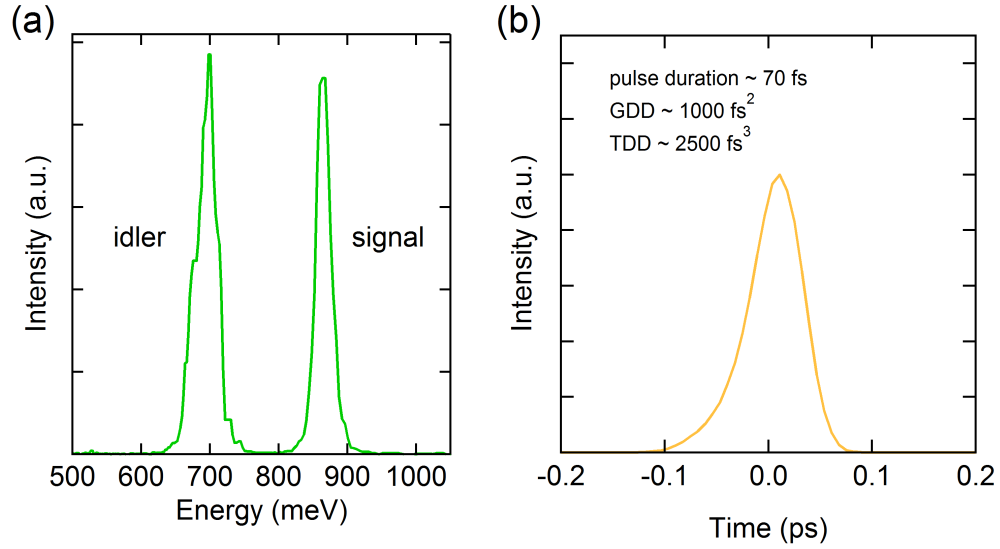
(a)

idler   signal

Intensity (a.u.)

500 600 700 800 900 1000
Energy (meV)

(b)

pulse duration ~ 70 fs
GDD ~ 1000 fs^2
TDD ~ 2500 fs^3

Intensity (a.u.)

-0.2   -0.1   0.0   0.1   0.2
Time (ps)

Figure C.2: **(a)** Representative signal and idler spectra measured at the output of the optical parametric amplifier. Both spectra are characterised by less than 1% of bandwidth. Panel **(b)** is the result of the analysis of a SH-FROG map, which returns a pulse duration of about 70 fs.

(a)

Intensity (a.u.)

80   120   160   200
Energy (meV)

(b)

pulse duration ~ 270 fs

Intensity (a.u.)

-1.0   -0.5   0.0   0.5   1.0
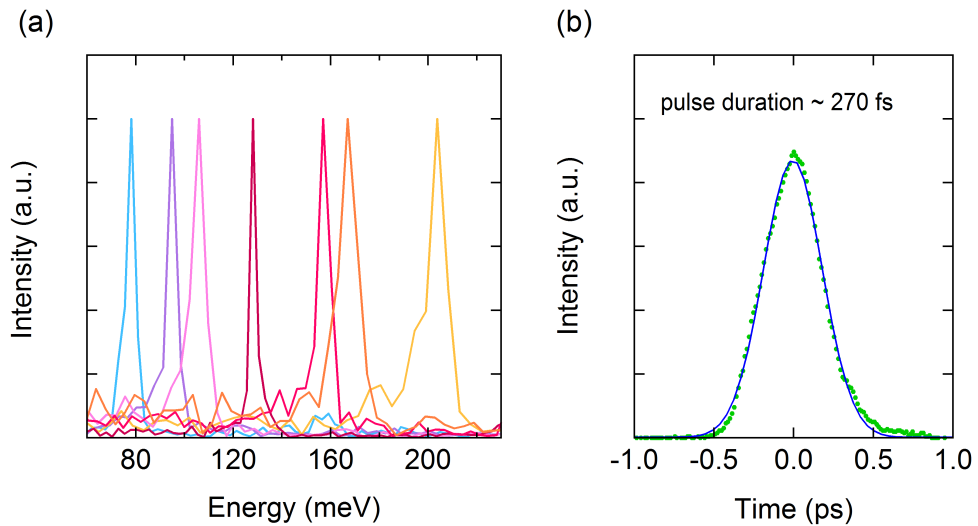Time (ps)

Figure C.3: **(a)** Normalised MIR spectra tuned over the entire phase matching bandwidth allowed by the setup. Pulses spanning from 75 to 200 meV were obtained. Panel **(b)** reports the crosscorrelation measurement performed with 800 nm pulses (green dots), together with a Gaussian fit (blue line). The mid-infrared pulses are characterised by a pulse duration of about 270 fs.

C.2 Generation and Detection of THz pulses

The THz pulses used to probe the light-induced superconducting-like phase of K_3C_{60} in the Chapter 4 and 5 have been generated by means of optical rectification of p-polarised 800 nm pulses in non-centrosymmetric nonlinear crystals. The optical reflectivity and complex optical conductivity spectra have been then recalculated from the THz spectra acquired by electro-optic sampling in a THz time domain spectroscopy setup (THz-TDS), which provides a complete characterisation of the spectrum and phase of the pulse, as explained in Appendix E [[123]].

The optical rectification of ultrashort pulses in noncentrosymmetric nonlinear crystals is a well established technique used to generate phase-stable, few-cycle THz pulses. The strong electric field of such femtosecond pulses triggers the onset of a nonlinear polarisation $P^{(2)}$ in the crystal proportional to its non-zero second-order susceptibility $\chi^{(2)}$. The temporal evolution of such modulation is then responsible for the emission of the THz radiation which is proportional to $d^2P^{(2)}/dt^2$ [124, 125, 126].

The most limiting factors in the generation of broad THz pulses by means of optical rectification are the bandwidth of the pump pulses used, the length of the crystal used and its transparency window in both the NIR and THz frequencies. For the case of 100 fs pulses centred at 800 nm, i.e. pulses with ~ 9.5 nm of bandwidth, frequencies up to ~ 4.4 THz can be generated.

Length and transparency of the nonlinear crystal affect both the intensity and the upper frequency which can be obtained via optical rectification. An efficient THz generation, requires a thickness of the nonlinear material shorter than the *walk-off length*, which is the length after which the 800 nm light and the generated low energy radiation will not be overlapped in time any more, and no phase-matching condition is satisfied. Within this limit, the longer the crystal, the stronger the generated THz field. Longer crystals on the other hand will pose a limit to the accessible THz bandwidth and a trade-off needs to be found to achieve broadband response and long interaction length. Finally the transparency of the material in the THz regime, i.e. the presence of low energy absorptions, can further limit the bandwidth

of the crystal due to a strong absorption coefficient. ZnTe for example, is characterised by a strong absorption around 5.4 THz and no spectral content can thus be generated around this frequency.

In the experiments reported in this thesis, two different p-polarised THz pulses with different spectral content have been used. In a first experimental configuration 100 fs long, 800 nm near-infrared light delivered from a 1 kHz Ti:sapphire system has been used for both the generation and detection of the THz pulses. 0.6 mJ of pump are sent at normal incidence into a 900 μm thick <110> ZnTe crystal, characterised by an electro-optic coefficient of about 4 pm/V [127]. The THz phase and spectral content have then been measured by means of electro-optic sampling in a 500 μm thick <110> ZnTe crystal, where 100 fs long, 800 nm pulses have been used to gate. In this experimental configuration, the THz pulse, displayed in Fig. C.4**(a-c)** is characterised by a band extending from 0.5 THz up to 2.7 THz (2-11 meV circa) and by a linear phase.

A much broader optical spectrum, from 1 THz up to 7.5 THz (4.1-31 meV) has been obtained by means of shorter near infrared pump pulses, with a broader spectral content. 0.9 mJ of 35 fs long, 800 nm pulses delivered by a 2 kHz repetition rate Ti:sapphire laser, are sent on a 200 μm thick <110> GaP crystal which has an electro-optical coefficient of 1 pm/V [128]. The resulting spectrum has been measured in another 200 μm thick <110> GaP crystal, where the short 35 fs, 800 nm pulses have been used as a gate. The final pulse, its spectral phase and its spectrum are reported in Fig C.4**(d-f)** respectively.

C.3   MIR-pump THz-probe setup

The MIR-pump THz-probe setup used in the experiment reported in Chapters 2 and 4 is schematically reported in Fig. C.5. The s-polarised mid-infrared pulses are sent onto the sample at normal incidence, while a small angle of about 17° has been set to the p-polarised THz probe. This angle is further reduced down to $\sim$ 7° by the refraction in the diamond window in front of the sample (see Appendix A).
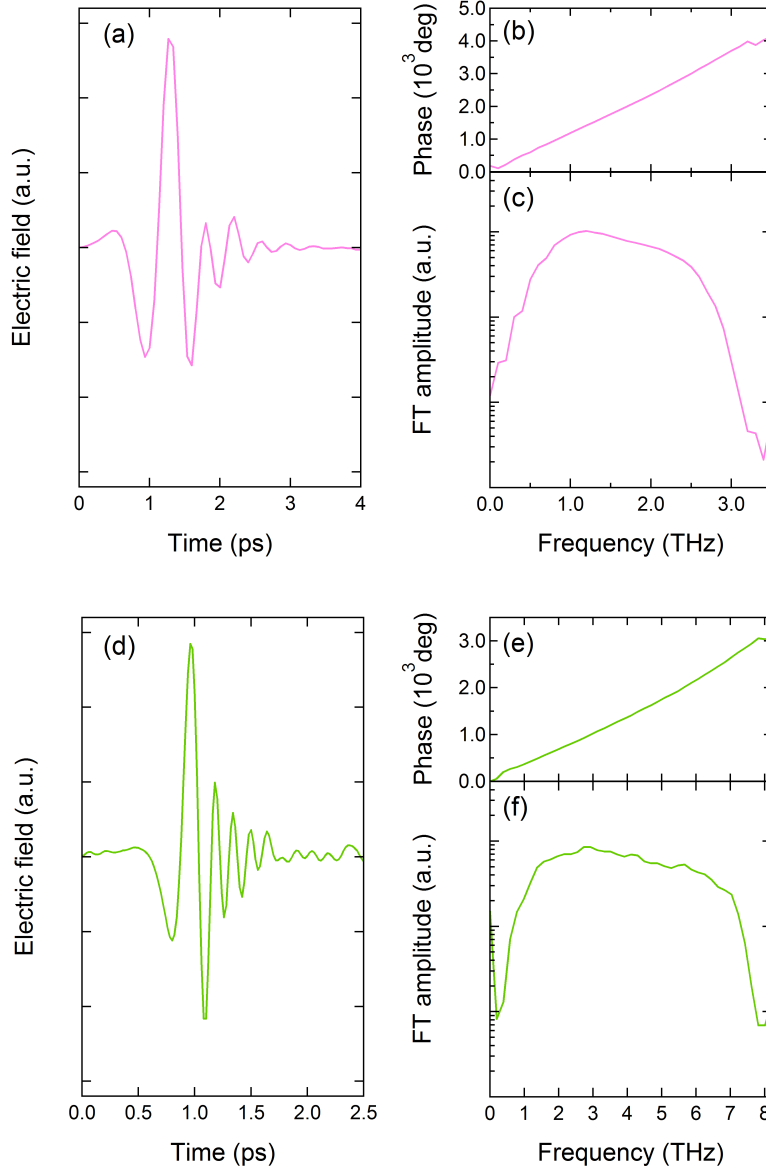
Figure C.4: Narrow and broad THz pulses used to probe the superconducting-like response of K_3C_{60}. Panels **(a-c)** show the pulse structure, the linear spectral phase and the 0.5-2.7 THz spectrum of the THz pulse generated by optical rectification of 100 fs long, 800 nm pulses in a 900 μm thick <110> ZnTe crystal, and probed in a 500 μm thick <110> ZnTe crystal. Panels **(d-e)** report the same information for the broader THz pulses generated by optical rectification of 35 fs long, 800 nm pulses in a 200 μm thick <110> GaP crystal and probed in a crystal with same specifications.

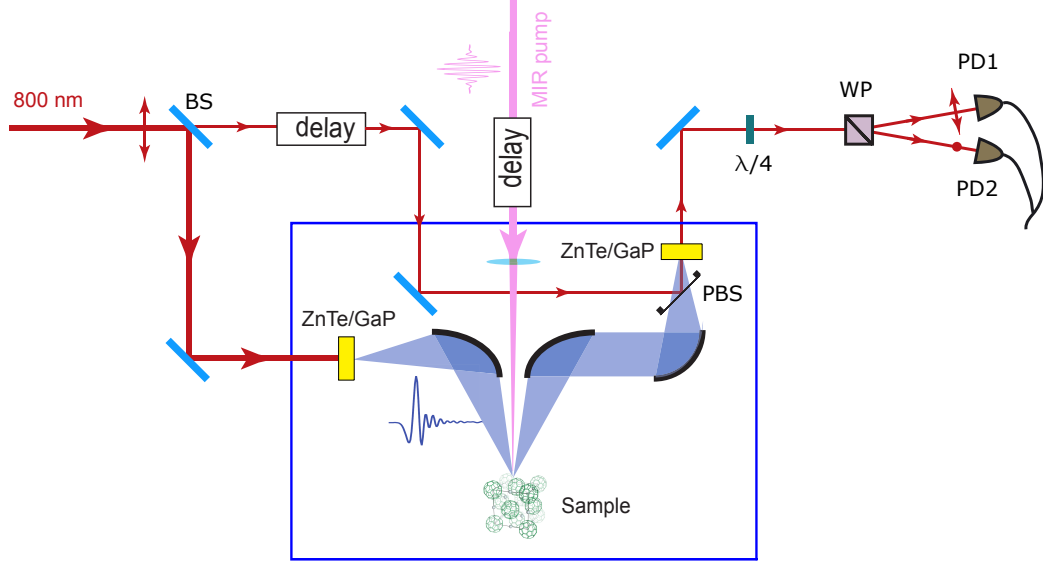**Figure C.5:** Schematic representation of the THz-time resolved setup. Red lines represent light at 800 nm, pink lines the MIR pump beam and the wide blue lines the THz light. The entire THz propagation path happens under vacuum (confined in the blue box). A first beam splitter (BS) divides the portion of light used for the THz generation from the one used as a gate in the detection. The nonlinear crystals (ZnTe or GaP) are represented in yellow. ($\lambda/4$) is the quarter wave waveplate, WP the Wollaston prism, PD1 and PD2 the two phtodiodes used for the electro-optic samplig of the THz field. PBS is a pellicle beam splitter used to recombine the THz and the 800 nm gate pulse. Figure adapted from [122].

In order to avoid all the air absorptions within the probe band, the THz generation and detection setup has been put in a vacuum chamber (blue square in Fig. C.5), and the sample has been mounted on the cold finger of a cryostat from Oxford Instruments without windows to prevent spurious reflections which would deteriorate the detection.

To optimise the pump-probe signal, the MIR spot size has been matched to the one of the lower frequency of the THz pulse at the sample position, to about 1 mm. In Fig. C.6 the frequency dependent spot sizes of the narrow and broad THz probe beams are reported, which are primarily limited by the f-number set in the experimental setup.

When THz-TDS is used in a time-resolved experiment, it is important to
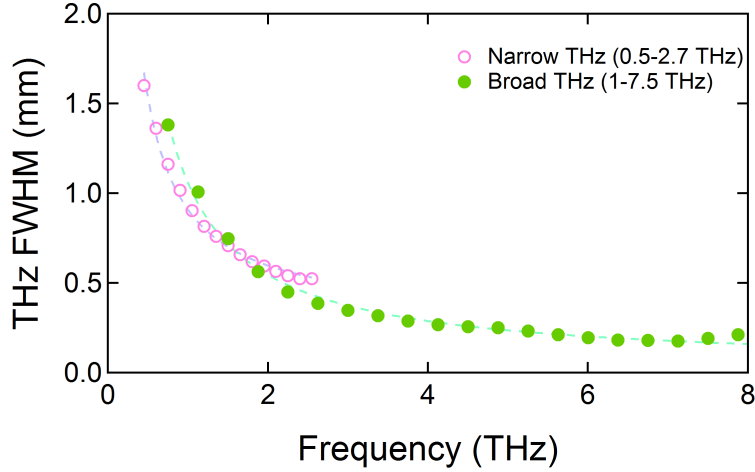
Figure C.6: Frequency resolved intensity spot size of the narrow and broad THz pulses used in the experiments reported in Chapters 4 and 5 (pink and green circles respectively). The dashed lines are $1/f$ fits of the two datasets, which report the proximity to the diffraction limit of the apparatus.

consider its temporal resolution. This detection scheme provides a resolution which is not set by the pulse length, which for THz pulses is considerably long, but is instead determined by its bandwidth [129, 130]. The broad pulses, with spectral content from 1 THz to 7.5 THz, will thus provide a finer temporal resolution of about 150 fs with respect to narrower ones ($\sim$ 300 fs). Independently of the THz probe pulse used in the pump probe experiments of Chapters 2 and 4, the temporal resolution was set primarily by the MIR pump pulse to 300 fs.

Appendix D

THz time domain spectroscopy under pressure

The transient optical response of K_3C_{60} after photo-excitation was measured under hydrostatic external pressure by integrating high pressure elements in the time-resolved THz spectroscopy setup described in the previous Appendix (Appendix C, Section C.3).

In the present section the technical limitations and compromises needed to perform such measurements are described, together with a few basic concepts of high pressure methods.

D.1 Hydrostatic high pressure by means of a diamond anvil cell

A diamond anvil cell (DAC) has been used to apply external hydrostatic pressure to the K_3C_{60} sample. The working mechanism of the DAC is pretty simple. Two diamonds with a flat tip (culet) squeeze a metallic gasket which has a hole in the center that confines the sample, as represented in Fig. D.1. Ruby nanoparticles are added in the sample compartment for the pressure calibration (see Section D.3).
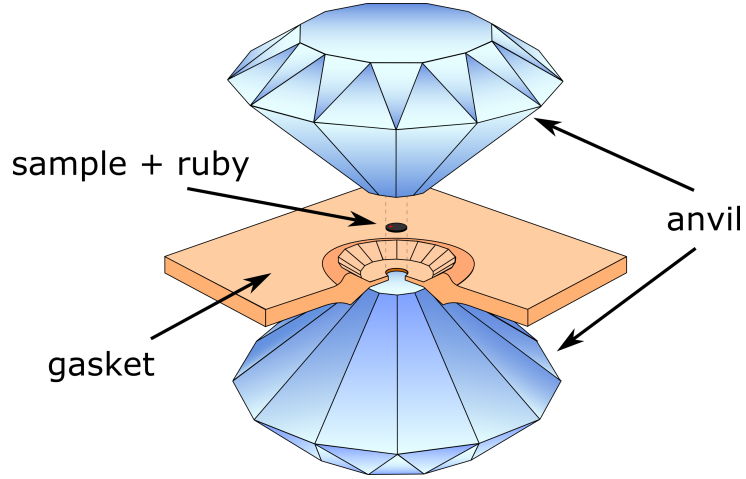
Figure D.1: Schematic representation of the diamond anvil cell. Two diamonds with a flat tip squeeze a metallic gasket which has a hole in the centre that confines the sample (dark disc). A few rubies are added on the sample surface for an accurate *in-situ* pressure measurement [131].

The size of the culet of the anvils is generally set based on the maximum desired pressure, defined as force over surface ($P = F/S$), and the wider the culet, the smaller the reachable pressure. In the experiment on the K_3C_{60}, relatively low pressures were targeted as the material is quite soft and at 3 GPa already the equilibrium superconducting phase is suppressed. Very pure type IIac anvils with 2 mm culet (Böhler-Almax cut, 1.55 mm thick), which allow reaching pressures as high as 3.5 GPa, have thus been chosen for the experiment described in Chapter 5.

A Cu gasket has been pre-indented by means of the same DAC in order to give stability and solidity. Gaskets 100 μm thick have been obtained from a 250 μm thick Cu plate. At the center of the indented gasket, a hole of 1.1 mm diameter has been drilled to host the pure sample, as the granularity of the K_3C_{60} powders have been exploited as a hydrostatic medium. No significant deformations of the hole were observed during the experiment.

The role of the gasket in the DAC it twofold. First if confines the sample laterally, but more importantly, it converts the axial pressure of the anvils to isotropic pressure [131].

D.2 Integration of THz-TDS with DAC

Hydrostatic pressure was applied using a membrane-driven Diacell®Bragg-LT diamond anvil cell (DAC) from Almax easyLab, designed for cryogenic experiments. This DAC allowed varying the static pressure by actuating a membrane with helium gas, without removing the cell from its holder, thereby ensuring maximum reliability and reproducibility of the measurement conditions. The DAC was mounted on the cold finger of a liquid helium cryostat, where the sample temperature and pressure were accurately measured using a ruby manometer [84, 85].

The most delicate aspect of the integration of high pressure elements in the THz-time-domain setup is the size of the sample with respect to the THz spot size at the sample position. As the sample and the Cu gasket lie on the same plane, the THz pulse reflected from the sample cannot be disentangled from the one also impinging on the surrounding copper. It is thus important to find a way around to avoid spurious reflections from the gasket which would affect the amplitude of the relative changes measured in the pump probe experiment.

A frequency resolved spacial distribution of the intensity of the THz beam is reported in Fig. C.6. All the frequencies above ~ 1 THz are mostly confined within 1 mm of spot size, and just the tails of the Gaussian profile carry information of the copper gasket. To minimize this contribution a sample compartment of 1.1 mm has been used and only frequencies above 1.4 THz have been trusted.

D.3 Ruby manometer

Ruby nanoparticles have been widely used as a universal standard for pressure calibration for pressures up to ~ 100 GPa [84]. The ruby manometer allows for *in-situ* reading, both of pressure and temperature, as it scales in a linear fashion over a wide temperature and pressure range [85].

The excitation with a green cw laser (532 nm) of rubies, i.e. Cr doped Al_2O_3 crystals, drives the electrons into an excited state from which they relax back
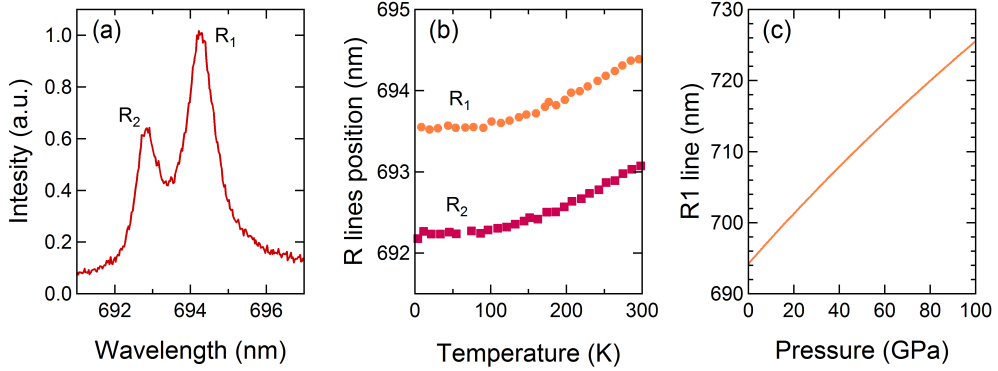
129

Figure D.2: **(a)** Normalised fluorescence spectrum of ruby nanoparticle at room temperature and ambient pressure. **(b)** R lines shift measured as a function of temperature. Data taken from [133]. **(c)** R_1 line shift as a function of pressure [84].

to the ground state via fluorescence in about 4-5 ms [132]. The radiative levels responsible for the fluorescence are known as the R_1 and the R_2 lines, which at ambient conditions are centred at 694.25 nm and 692.85 nm respectively and are relatively sharp (see Fig. D.2**(a)**). The shift and reshaping of these two lines as a function of temperature and pressure allows an accurate estimation of the experimental conditions.

In order to determine the effective pressure in each experimental run accurately, the temperature of the sample must be known first. A possible reliable reading can be obtained by looking at the blue shift of the emission lines at ambient pressure for colder temperatures. Figure D.2**(b)** reports the shift of the two lines measured from room temperature down to a few Kelvin. As the temperature approaches 100 K the two lines become less sensitive and the retrieval of the temperature becomes inaccurate [133].

Besides the peak positions, there is considerably more information available in the standard ruby pressure measurement: the splitting Δ, the widths δ_{R1} and δ_{R2} and the intensities I_1 and I_2. Central frequency, splitting and widths of the two R lines can be used above 100 K as a thermometer with a relatively good accuracy, while for cryogenic temperatures these quantity also become almost temperature independent [134]. In this case the ratio of the intensities I_1/I_2 is preferred for an accurate temperature reading and the temperature

can be extracted as [85, 135]

$$T(K) = \frac{\Delta}{k_B} \cdot \frac{1}{\ln(\eta I_1 / I_2)}, \tag{D.1}$$

where η is the ratio of the quantum efficiency of the R_2 to the R_1 transition for $k_B T > \Delta$. In the same way as the splitting Δ, the efficiency η does not vary significantly below 100 K, and their values are thus constant terms $\Delta/k_B = 42\ K$, $\eta = 0.65$ [136].

In the experiment reported in Chapter 5, the linear shift of the R lines of the rubies put on the top surface of the DAC has been used to retrieve the temperature above 100 K, while below this temperature value the ratio of the intensities has been used.

Once the temperature is known, the red shift of the R_1 ruby line with respect to the calibrated position provides an accurate measurement of the pressure. Figure D.2(**c**) displays the position of the R_1 line as a function of pressure at room temperature. The pressure value can be extracted from [137, 138, 84]:

$$P(GPa) = \frac{A}{B} \left[\left(\frac{\lambda}{\lambda_0} \right)^B - 1 \right], \tag{D.2}$$

where A and B are experimentally determined, equal to 1904 GPa and 7.665 respectively in quasi-hydrostatic conditions [84].

Appendix E

Models to retrieve the optical properties from THz-TDS

In the experiment reported in this thesis, the stationary electric field reflected by the sample, $E_R(t)$, and the pump-induced changes, $\Delta E_R(t, \tau) = E_R^{pumpon}(t, \tau) - E_R(t)$, were measured at several pump-probe delays τ.

For the case of narrow THz probe pulses, these two reflected pulses have been acquired one after the other [122, 23], while in the experiment with the extended broad THz pulses the electro-optic signal has been sampled simultaneously with two lock-in amplifiers [139]. The advantage of a double lock-in amplifier detection scheme, properly calibrated, relies on the fact that simultaneous measurements of the light-induced changes and the reference electric field allow avoiding the introduction of possible phase artefacts. This aspect becomes of severe relevance when the measured electric field contains fast-varying frequencies.

By Fourier transforming the temporal signals with respect to the time coordinate t, the complex-valued frequency dependent $E_R(\omega)$ and $\Delta E_R(\omega, \tau)$ have been obtained.

To retrieve the light-induced changes in the sample, first the complex Fresnel reflection coefficient of the photo-excited material, $r(\omega, \tau)$, has been deter-
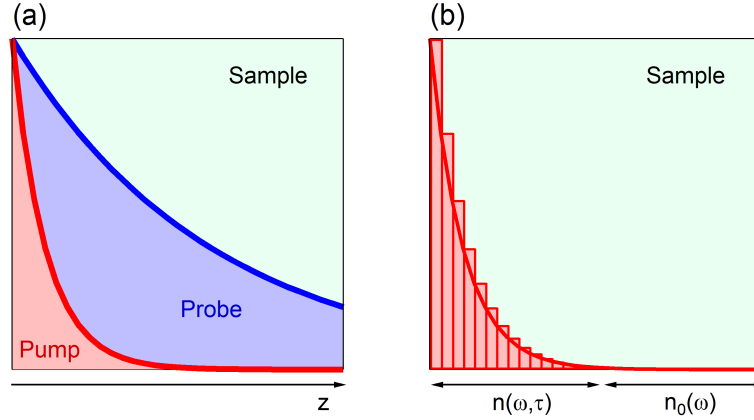
Figure E.1: **(a)** Schematics of pump-probe penetration depth mismatch. **(b)** Multi-layer model with exponential decay used to calculate the pump-induced changes in the complex refractive index $n(\omega, \tau)$.

mined as

$$\frac{\Delta E_R(\omega, \tau)}{E_R(\omega)} = \frac{r(\omega, \tau) - r_0(\omega)}{r_0(\omega)},$$
(E.1)

where $r_0(\omega)$ is the complex equilibrium value, extracted from the static reflectivity measurements (see Appendix B).

As the penetration depth of the MIR pump and of the THz probe are quite different, 700-800 nm and 150-200 nm respectively (see Fig E.1**(a)**), the "raw" light-induced changes were then reprocessed, for a more accurate estimate. Importantly, this renormalisation only affects the size of the response, whereas the qualitative changes in the optical properties are independent of it and of the specific model chosen to account for penetration depth mismatch.

All the spectra shown in Chapter 4 and 5 have been retrieved by treating the excited surface as a stack of thin layers with a homogeneous refractive index and describing the excitation profile by an exponential decay (see Fig. E.1**(b)**). By calculating the coupled Fresnel equations of a such multi-layer system, the complex refractive index at the surface, $n(\omega, \tau)$, can be retrieved, and from this the complex conductivity $\sigma(\omega, \tau)$ for a volume that is homogeneously transformed.

Bibliography

[1] D. I. Khomskii, *Basic Aspects of The Quantum Theory of Solids*. Cambridge: Cambridge University Press, 2010.

[2] "Introduction to Phase Transitions."

[3] ""Philip W. Anderson - Facts". Nobelprize.org."

[4] M. Sigrist and K. Ueda, "Phenomenological theory of unconventional superconductivity," *Reviews of Modern Physics*, vol. 63, no. 2, pp. 239–311, 1991.

[5] D. Sherman, U. S. Pracht, B. Gorshunov, S. Poran, J. Jesudasan, M. Chand, P. Raychaudhuri, M. Swanson, N. Trivedi, A. Auerbach, M. Scheffler, A. Frydman, and M. Dressel, "The Higgs mode in disordered superconductors close to a quantum phase transition," *Nature Physics*, vol. 11, no. 2, pp. 188–192, 2015.

[6] G. M. Luke, T. Fudamoto, K. M. Kojima, M. I. Larkin, J. Merrin, B. Nachumi, Y. I. Uemura, Y. Maeno, Z. Q. Mao, Y. Mori, H. Nakamura, and M. Sigrist, "Time-reversal symmetry-breaking superconductivity in Sr_2RuO_4," *Nature*, vol. 394, no. August, pp. 558–561, 1998.

[7] M. Hücker, M. V. Zimmermann, M. Debessai, J. S. Schilling, J. M. Tranquada, and G. D. Gu, "Spontaneous symmetry breaking by charge stripes in the high pressure phase of superconducting $La_{1.875}Ba_{0.125}CuO_4$," *Physical Review Letters*, vol. 104, no. 5, pp. 3–6, 2010.

Bibliography

[8] M. Hücker, M. V. Zimmermann, Z. J. Xu, J. S. Wen, G. D. Gu, and J. M. Tranquada, "Enhanced charge stripe order of superconducting $La_{2-x}Ba_xCuO_4$ in a magnetic field," *Physical Review B - Condensed Matter and Materials Physics*, vol. 87, no. 1, pp. 1–6, 2013.

[9] D. Nicoletti, E. Casandruc, D. Fu, P. Giraldo-Gallo, I. R. Fisher, and A. Cavalleri, "Anomalous relaxation kinetics and charge-density-wave correlations in underdoped $BaPb_{1-x}Bi_xO_3$," *Proceedings of the National Academy of Sciences*, vol. 114, pp. 9020–9025, aug 2017.

[10] T. M. Hoang, C. S. Gerving, B. J. Land, M. Anquez, C. D. Hamley, and M. S. Chapman, "Dynamic stabilization of a quantum many-body spin system," *Physical Review Letters*, vol. 111, no. 9, pp. 1–5, 2013.

[11] D. Nicoletti and A. Cavalleri, "Nonlinear light–matter interaction at terahertz frequencies," *Advances in Optics and Photonics*, vol. 8, no. 3, p. 401, 2016.

[12] A. Subedi, A. Cavalleri, and A. Georges, "Theory of nonlinear phononics for coherent light-control of solids," pp. 1–10, 2013.

[13] J. P. Sethna, *Statistical Mechanics: Entropy, Order Parameters, and Complexity*. OUP Oxford, 2006.

[14] T. F. Nova, A. Cartella, A. Cantaluppi, M. Först, D. Bossini, R. V. Mikhaylovskiy, A. V. Kimel, R. Merlin, and A. Cavalleri, "An effective magnetic field from optically driven phonons," *Nature Physics*, vol. 13, pp. 132–136, feb 2017.

[15] S. Kaiser, S. R. Clark, D. Nicoletti, G. Cotugno, R. I. Tobey, N. Dean, S. Lupi, H. Okamoto, T. Hasegawa, D. Jaksch, and a. Cavalleri, "Optical properties of a vibrationally modulated solid state Mott insulator.," *Scientific reports*, vol. 4, p. 3823, 2014.

[16] R. Singla, G. Cotugno, S. Kaiser, M. Först, M. Mitrano, H. Y. Liu, A. Cartella, C. Manzoni, H. Okamoto, T. Hasegawa, S. R. Clark, D. Jaksch, and A. Cavalleri, "THz-Frequency Modulation of the Hubbard U in an Organic Mott Insulator," *Physical Review Letters*, vol. 115, p. 187401, oct 2015.

[17] W. Hu, S. Kaiser, D. Nicoletti, C. R. Hunt, I. Gierz, M. C. Hoffmann, M. Le Tacon, T. Loew, B. Keimer, and A. Cavalleri, "Optically enhanced coherent

transport in $YBa_2Cu_3O_{6.5}$ by ultrafast redistribution of interlayer coupling," *Nature Materials*, vol. 13, pp. 705–711, may 2014.

[18] R. Mankowsky, A. Subedi, M. Först, S. O. Mariager, M. Chollet, H. T. Lemke, J. S. Robinson, J. M. Glownia, M. P. Minitti, A. Frano, M. Fechner, N. a. Spaldin, T. Loew, B. Keimer, A. Georges, and A. Cavalleri, "Nonlinear lattice dynamics as a basis for enhanced superconductivity in $YBa_2Cu_3O_{6.5}$," *Nature*, vol. 516, pp. 71–73, dec 2014.

[19] H. W. Kroto, J. R. Heath, S. C. O'Brien, R. F. Curl, and R. E. Smalley, "C_{60}: Buckminsterfullerene," *Nature*, vol. 318, pp. 162–163, nov 1985.

[20] R. Wood, *Optical and electronic properties of fullerenes and fullerene-based materials*, vol. 33. feb 2000.

[21] O. Gunnarsson, *Alkali-doped Fullerides. Narrow-band solids with unusual properties*, vol. XVII. 2004.

[22] J. Hedberd, "Free Science Images."

[23] M. Mitrano, A. Cantaluppi, D. Nicoletti, S. Kaiser, A. Perucchi, S. Lupi, P. Di Pietro, D. Pontiroli, M. Riccò, S. R. Clark, D. Jaksch, and A. Cavalleri, "Possible light-induced superconductivity in K_3C_{60} at high temperature.," *Nature*, vol. 530, no. 7591, pp. 461–464, 2016.

[24] A. Cantaluppi, M. Buzzi, D. Nicoletti, M. Mitrano, D. Pontiroli, M. Riccò, A. Perucchi, P. Di Pietro, and A. Cavalleri, "Pressure tuning of light-induced superconductivity in K_3C_{60}," *arXiv:1705.05939*, may 2017.

[25] J. S. Wong and C. B. Moore, "Bond Selective Excitation of Moleeules," 1981.

[26] Y. Wu, L. Fan, W. Huang, S. Chen, S. Chen, F. Chen, C. Zou, and Z. Wu, "Depressed transition temperature of $W_xV_{1-x}O_2$: mechanistic insights from the X-ray absorption fine structure (XAFS) spectroscopy," *Physical Chemistry Chemical Physics*, vol. 16, p. 17705, jul 2014.

[27] D. N. Basov, R. D. Averitt, D. van der Marel, M. Dressel, and K. Haule, "Electrodynamics of correlated electron materials," *Reviews of Modern Physics*, vol. 83, pp. 471–541, jun 2011.

[28] E. Dagotto, "Complexity in Strongly Correlated Electronic Systems," *Science*, vol. 309, pp. 257–262, jul 2005.

[29] F. J. Morin, "Oxides which show a metal-to-insulator transition at the neel temperature," *Physical Review Letters*, vol. 3, no. 1, pp. 34–36, 1959.

[30] A. Cavalleri, C. Tóth, C. W. Siders, J. A. Squier, F. Ráksi, P. Forget, and J. C. Kieffer, "Femtosecond Structural Dynamics in VO_2 during an Ultrafast Solid-Solid Phase Transition," *Physical Review Letters*, vol. 87, p. 237401, nov 2001.

[31] H. Y. Hwang, S. W. Cheong, P. G. Radaelli, M. Marezio, and B. Batlogg, "Lattice effects on the magnetoresistance in doped $LaMnO_3$," *Physical Review Letters*, vol. 75, no. 5, pp. 914–917, 1995.

[32] M. Rini, R. Tobey, N. Dean, J. Itatani, Y. Tomioka, Y. Tokura, R. W. Schoenlein, and A. Cavalleri, "Control of the electronic phase of a manganite by mode-selective vibrational excitation.," *Nature*, vol. 449, no. 7158, pp. 72–74, 2007.

[33] M. Först, C. Manzoni, S. Kaiser, Y. Tomioka, Y. Tokura, R. Merlin, and a. Cavalleri, "Nonlinear phononics as an ultrafast route to lattice control," *Nature Physics*, vol. 7, pp. 854–856, aug 2011.

[34] C. Raman and K. Krishnan, "A New Type of Secondary Radiation," *Nature*, vol. 121, no. 3048, pp. 501–502, 1928.

[35] R. Merlin, "Generating coherent THz phonons with light pulses," *Solid State Communications*, vol. 102, no. 2-3, pp. 207–220, 1997.

[36] T. Dekorsy, G. C. Cho, and H. Kurz, "Coherent phonons in condensed media," in *Light Scattering in Solids VIII* (M. Cardona and G. Güntherodt, eds.), vol. 76 of *Topics in Applied Physics*, pp. 169–209, Springer Berlin Heidelberg, 2000.

[37] T. P. Martin and L. Genzel, "Ionic Raman Scattering and Ionic Frequency Mixing," *Physica Status Solidi (B)*, vol. 61, no. 2, pp. 493–502, 1974.

[38] R. F. Wallis and A. A. Maradudin, "Ionic Raman Effect. II. The First-Order Ionic Raman Effect," *Physical Review B*, vol. 3, pp. 2063–2075, mar 1971.

[39] T. P. Martin and L. Genzel, "Ionic Raman Scattering and Ionic Frequency Mixing," *Physica Status Solidi (B)*, vol. 61, pp. 493–502, feb 1974.

[40] M. Först, R. Mankowsky, and A. Cavalleri, "Mode-Selective Control of the Crystal Lattice," *Accounts of Chemical Research*, vol. 48, pp. 380–387, feb 2015.

[41] R. Mankowsky, M. Först, and A. Cavalleri, "Non-equilibrium control of complex solids by nonlinear phononics," *Reports on Progress in Physics*, vol. 79, p. 064503, jun 2016.

[42] R. Mankowsky, *Nonlinear phononics and structural control of strongly correlated materials*. PhD thesis, 2015.

[43] T. Hasegawa, S. Kagoshima, T. Mochida, S. Sugiura, and Y. Iwasa, "Electronic states and anti-ferromagnetic order in mixed-stack charge-transfer compound (BEDT-TTF)(F_2TCNQ)," *Solid State Communications*, vol. 103, pp. 489–493, aug 1997.

[44] D. Fausti, R. I. Tobey, N. Dean, S. Kaiser, A. Dienst, M. C. Hoffmann, S. Pyon, T. Takayama, H. Takagi, and A. Cavalleri, "Light-induced superconductivity in a stripe-ordered cuprate.," *Science (New York, N.Y.)*, vol. 331, no. 6014, pp. 189–91, 2011.

[45] M. Först, R. I. Tobey, H. Bromberger, S. B. Wilkins, V. Khanna, A. D. Caviglia, Y.-D. Chuang, W. S. Lee, W. F. Schlotter, J. J. Turner, M. P. Minitti, O. Krupin, Z. J. Xu, J. S. Wen, G. D. Gu, S. S. Dhesi, A. Cavalleri, and J. P. Hill, "Melting of Charge Stripes in Vibrationally Driven $La_{1.875}Ba_{0.125}CuO_4$," *Physical Review Letters*, vol. 112, p. 157002, apr 2014.

[46] E. Pavarini, I. Dasgupta, T. Saha-Dasgupta, O. Jepsen, and O. K. Andersen, "Band-Structure Trend in Hole-Doped Cuprates and Correlation with T_{xmax}," *Physical Review Letters*, vol. 87, p. 047003, jul 2001.

[47] C. R. Hunt, D. Nicoletti, S. Kaiser, D. Pröpper, T. Loew, J. Porras, B. Keimer, and A. Cavalleri, "Dynamical decoherence of the light induced interlayer coupling in $YBa_2Cu_3O_{6+d}$," *Physical Review B*, vol. 94, p. 224303, dec 2016.

[48] M. Magnuson, T. Schmitt, V. N. Strocov, J. Schlappa, A. S. Kalabukhov, and L.-C. Duda, "Self-doping processes between planes and chains in the metal-to-superconductor transition of $YBa_2Cu_3O_{6.9}$," *Scientific Reports*, vol. 4, p. 7017, may 2015.

[49] D. R. Tobergte and S. Curtis, *Organic Molecular Solids*, vol. 53. Weinheim, Germany: Wiley-VCH Verlag GmbH, dec 2006.

[50] G. J. Burkhart and C. Meingast, "High-resolution thermal expansion of superconducting fullerides A_3C_{60} (A = K,Rb)," *Physical Review B*, vol. 54, no. 10, pp. R6865–R6868, 1996.

[51] A. Bright, A. Garito, and A. Heeger, "Optical properties of (TTF) (TCNQ) in the visible and infrared," *Solid State Communications*, vol. 13, pp. 943–948, oct 1973.

[52] M. Dressel, "Ordering phenomena in quasi-one-dimensional organic conductors," *Naturwissenschaften*, vol. 94, no. 7, pp. 527–541, 2007.

[53] T. Ishiguro, K. Yamaji, and G. Saito, *Organic Superconductors*, vol. 88 of *Springer Series in Solid-State Sciences*. Berlin, Heidelberg: Springer Berlin Heidelberg, 1998.

[54] S. E. Brown, P. M. Chaikin, M. J. Naughton, and A. Lebed, *The Physics of Organic Superconductors and Conductors*, vol. 110. 2008.

[55] "Das Benzol-Molekül."

[56] M. Imada, A. Fujimori, and Y. Tokura, "Metal-insulator transitions," *Reviews of Modern Physics*, vol. 70, no. 4, pp. 1039–1263, 1998.

[57] A. Georges, G. Kotliar, W. Krauth, and M. Rozenberg, "Dynamical mean-field theory of strongly correlated fermion systems and the limit of infinite dimensions," *Reviews of Modern Physics*, vol. 68, no. 1, pp. 13–125, 1996.

[58] Y. Ihara, H. Alloul, P. Wzietek, D. Pontiroli, M. Mazzani, and M. Riccò, "Spin dynamics at the Mott transition and in the metallic state of the Cs_3C_{60} superconducting phases," *EPL*, vol. 94, p. 37007, may 2011.

[59] K. Bechgaard, K. Carneiro, M. Olsen, F. B. Rasmussen, and C. S. Jacobsen, "Zero-Pressure Organic Superconductor: Di-(Tetramethyltetraselenafulvalenium)-Perchlorate [(TMTSF)$_2$ClO$_4$]," *Physical Review Letters*, vol. 46, pp. 852–855, mar 1981.

[60] D. Jérome, A. Mazaud, M. Ribault, and K. Bechgaard, "Superconductivity in a synthetic organic conductor (TMTSF)$_2$PF$_6$," *Journal de Physique Lettres*, vol. 41, pp. 95–98, 1980.

[61] A. Potočnik, A. Krajnc, P. Jeglič, Y. Takabayashi, A. Y. Ganin, K. Prassides, M. J. Rosseinsky, and D. Arčon, "Size and symmetry of the superconducting gap in the f.c.c. Cs$_3$C$_{60}$ polymorph close to the metal-Mott insulator boundary," *Scientific Reports*, vol. 4, p. 4265, may 2015.

[62] T. T. M. Palstra, A. F. Hebard, R. C. Haddon, and P. B. Littlewood, "Fermi-liquid behavior in the electrical resistivity of K$_3$C$_{60}$ and Rb$_3$C$_{60}$," *Physical Review B*, vol. 50, pp. 3462–3465, aug 1994.

[63] S. E. Brown, P. M. Chaikin, M. J. Naughton, and A. Lebed, *The Physics of Organic Superconductors and Conductors*, vol. 110. 2008.

[64] H. W. Kroto, J. E. Fischer, and D. Cox, *The Fullerenes*. Elsevier Science, 2012.

[65] O. Gunnarsson, "Superconductivity in fullerides," *Reviews of Modern Physics*, vol. 69, pp. 575–606, apr 1997.

[66] L. Degiorgi, G. Briceno, M. S. Fuhrer, A. Zettl, and P. Wachter, "Optical measurements of the superconducting gap in single-crystal K$_3$C$_{60}$ and Rb$_3$C$_{60}$," *Nature*, vol. 369, pp. 541–543, jun 1994.

[67] A. Y. Ganin, Y. Takabayashi, P. Jeglič, D. Arčon, A. Potočnik, P. J. Baker, Y. Ohishi, M. T. McDonald, M. D. Tzirakis, A. McLennan, G. R. Darling, M. Takata, M. J. Rosseinsky, and K. Prassides, "Polymorphism control of superconductivity and magnetism in Cs$_3$C$_{60}$ close to the Mott transition," *Nature*, vol. 466, pp. 221–225, jul 2010.

[68] R. M. Fleming, a. P. Ramirez, M. J. Rosseinsky, D. W. Murphy, R. C. Haddon, S. M. Zahurak, and a. V. Makhija, "Relation of structure and superconducting transition temperatures in A$_3$C$_{60}$," 1991.

[69] O. Zhou, Q. Zhu, J. E. Fischer, N. Coustel, G. B. Vaughan, P. a. Heiney, J. P. McCauley, and a. B. Smith, "Compressibility of M_3C_{60} Fullerene Superconductors: Relation Between T_c and Lattice Parameter.," *Science (New York, N.Y.)*, vol. 255, no. 5046, pp. 833–835, 1992.

[70] L. Degiorgi, E. J. Nicol, O. Klein, G. Gr?ner, P. Wachter, S.-M. Huang, J. Wiley, and R. B. Kaner, "Optical properties of the alkali-metal-doped superconducting fullerenes: K_3C_{60} and Rb_3C_{60}," *Physical Review B*, vol. 49, pp. 7012–7025, mar 1994.

[71] M. Tinkham, "Introduction to superconductivity," 1996.

[72] L. Degiorgi, P. Wachter, G. Grüner, S.-M. Huang, J. Wiley, and R. B. Kaner, "Optical response of the superconducting state of K3C60 and Rb3C60," *Physical Review Letters*, vol. 69, pp. 2987–2990, nov 1992.

[73] L. Degiorgi, G. Briceno, M. Fuhrer, A. Zettl, P. Wachter, and E. Nicol, "The electrodynamic response of K_3C_{60} and Rb_3C_{60} single crystals," *Synthetic Metals*, vol. 70, pp. 1325–1327, mar 1995.

[74] M. Capone, M. Fabrizio, C. Castellani, and E. Tosatti, "Strongly correlated superconductivity.," *Science (New York, N.Y.)*, vol. 296, pp. 2364–2366, jun 2002.

[75] M. Capone, M. Fabrizio, C. Castellani, and E. Tosatti, "Colloquium: Modeling the unconventional superconducting properties of expanded A3C60 fullerides," *Reviews of Modern Physics*, vol. 81, pp. 943–958, jun 2009.

[76] Y. Nomura, S. Sakai, M. Capone, and R. Arita, "Unified understanding of superconductivity and Mott transition in alkali-doped fullerides from first principles," *Science Advances*, vol. 1, pp. e1500568–e1500568, aug 2015.

[77] M. Kim, Y. Nomura, M. Ferrero, P. Seth, O. Parcollet, and A. Georges, "Enhancing superconductivity in A_3C_{60} fullerides," *Physical Review B*, vol. 94, no. 15, p. 155152, 2016.

[78] V. Buntar and H. W. Weber, "Magnetic properties of fullerene superconductors," *Superconductor Science and Technology*, vol. 9, pp. 599–615, aug 1996.

[79] M. Dressel and G. Gruner, *Electrodynamics of Solids*. Cambridge: Cambridge University Press, 2002.

[80] K. R. Wilson and V. V. Yakovlev, "Ultrafast rainbow: tunable ultrashort pulses from a solid-state kilohertz system," *Journal of the Optical Society of America B*, vol. 14, no. 2, p. 444, 1997.

[81] I. Kézsmárki, R. Gaál, C. C. Homes, B. Sípos, H. Berger, S. Bordács, G. Mihály, and L. Forró, "High-pressure infrared spectroscopy: Tuning of the low-energy excitations in correlated electron systems," *Physical Review B - Condensed Matter and Materials Physics*, vol. 76, no. 20, pp. 2–6, 2007.

[82] A. Perucchi, L. Baldassarre, P. Postorino, and S. Lupi, "Optical properties across the insulator to metal transitions in vanadium oxide compounds," *Journal of Physics: Condensed Matter*, vol. 21, no. 32, p. 323202, 2009.

[83] J. Plaskett and P. Schatz, "On the Robinson and Price (Kramers-Kronig) Method of Interpreting Reflection Data Taken through a Transparent Window," *Journal of Chemical Physics Volume*, vol. 38, no. 3, pp. 612–617, 1963.

[84] H. K. Mao, J. Xu, and P. M. Bell, "Calibration of the ruby pressure gauge to 800 kbar under quasi-hydrostatic conditions," *Journal of Geophysical Research*, vol. 91, no. B5, p. 4673, 1986.

[85] B. A. Weinstein, "Ruby thermometer for cryobaric diamond-anvil cell," *Review of Scientific Instruments*, vol. 57, no. 5, pp. 910–913, 1986.

[86] G. Klupp, P. Matus, K. Kamarás, A. Y. Ganin, A. McLennan, M. J. Rosseinsky, Y. Takabayashi, M. T. McDonald, and K. Prassides, "Dynamic Jahn-Teller effect in the parent insulating state of the molecular superconductor Cs_3C_{60}.," *Nature communications*, vol. 3, p. 912, jan 2012.

[87] A. Karamatskou, R. Santra, and O. Vendrell, "Ab Initio Investigation of Nonlinear Mode Coupling in C_{60}," *The Journal of Physical Chemistry Letters*, no. 5, pp. 5543–5547, 2017.

[88] M. J. Rice and H. Y. Choi, "Charged-phonon absorption in doped C_{60}," *Physical Review B*, vol. 45, no. 17, pp. 10173–10176, 1992.

[89] J. van den Brink, O. Gunnarsson, and V. Eyert, "Optical conductivity in A_3C_{60} (A=K,Rb)," *Physical Review B*, vol. 57, no. 4, pp. 2163–2167, 1998.

[90] M. C. Martin, X. Du, J. Kwon, and L. Mihaly, "Observation and assignment of silent and higher-order vibrations in the infrared transmission of C_{60} crystals," *Physical Review B*, vol. 50, no. 1, pp. 173–183, 1994.

[91] J. Menéndez and J. B. Page, "Vibrational spectroscopy of C_{60}," in *Light Scattering in Solids VIII. Topics in Applied Physics*, vol. 76, pp. 27–95, Springer Berlin Heidelberg, jul 2000.

[92] G. J. Snyder and A. Simon, "Reaction of alkali metal intercalated C_{60} with oxygen: Deintercalation, activation, and decomposition," *Advanced Materials*, vol. 6, pp. 374–376, may 1994.

[93] A. Böttcher, S. Fichtner-Endruschat, M. Wohlers, and H. Niehus, "Electron emission during oxidation of Cs-fullerides," *Surface Science*, vol. 388, pp. 177–185, oct 1997.

[94] J. A. Nisha, V. Sridharan, J. Janaki, Y. Hariharan, V. S. Sastry, C. S. Sundar, and T. S. Rakhakrishnan, "Studies of C_{60} oxidation and products," *Journal of Physical Chemistry*, vol. 100, no. 11, pp. 4503–4506, 1996.

[95] A. Rothwarf and B. N. Taylor, "Measurement of recombination lifetimes in superconductors," *Physical Review Letters*, vol. 19, no. 1, pp. 27–30, 1967.

[96] J. Demsar, R. D. Averitt, A. J. Taylor, V. V. Kabanov, W. N. Kang, H. J. Kim, E. M. Choi, and S. I. Lee, "Pair-Breaking and Superconducting State Recovery Dynamics in MgB_2," *Physical Review Letters*, vol. 91, p. 267002, dec 2003.

[97] W. Zimmermann, E. H. Brandt, M. Bauer, E. Seider, and L. Genzel, "Optical conductivity of BCS superconductors with arbitrary purity," *Physica C: Superconductivity and its applications*, vol. 183, no. 1-3, pp. 99–104, 1991.

[98] G. Mazza and A. Georges, "Nonequilibrium superconductivity in driven alkali-doped fullerides," *Physical Review B*, vol. 96, no. 6, pp. 1–10, 2017.

[99] J. R. Coulthard, S. R. Clark, S. Al-Assam, A. Cavalleri, and D. Jaksch, "Enhancement of superexchange pairing in the periodically driven Hubbard model," *Physical Review B*, vol. 96, p. 085104, aug 2017.

[100] M. Knap, M. Babadi, G. Refael, I. Martin, and E. Demler, "Dynamical Cooper pairing in nonequilibrium electron-phonon systems," *Physical Review B*, vol. 94, p. 214504, dec 2016.

[101] D. M. Kennes, E. Y. Wilner, D. R. Reichman, and A. J. Millis, "Transient superconductivity from electronic squeezing of optically pumped phonons," *Nature Physics*, vol. 13, pp. 479–483, jan 2017.

[102] M.-Z. Huang, Y.-N. Xu, and W. Y. Ching, "Pressure dependence of the band structure, density of states, Fermi surfaces, and optical properties of superconducting K_3C_{60}," *Physical Review B*, vol. 47, pp. 8249–8259, apr 1993.

[103] G. Sparn, J. D. Thompson, S. M. Huang, R. B. Kaner, F. Diederich, R. L. Whetten, G. Grüner, and K. Holczer, "Pressure Dependence of Superconductivity in Single-Phase K_3C_{60}.," *Science (New York, N.Y.)*, vol. 252, pp. 1829–31, jun 1991.

[104] D. Varshney, "Effect of pressure on transition temperature of Rb_3C_{60} fullerides," *High Pressure Research*, vol. 26, pp. 203–222, sep 2006.

[105] P. Auban-Senzier, R. Kerkoud, D. Jerome, F. Rachdi, and P. Bernier, "Fullerenes Under Pressure Studied by ^{13}C-NMR," *MRS Proceedings*, vol. 359, p. 261, jan 1994.

[106] S. Kawasaki, J. Fukui, T. Motoyama, Y. Suzuki, S. Shibasaki, and G.-q. Zheng, "The Mott State and Superconductivity in Face-Centred Cubic Structured Cs_3C_{60} : A ^{133}Cs-Nuclear Magnetic Resonance Study under Pressure," *Journal of the Physical Society of Japan*, vol. 82, p. 014709, jan 2013.

[107] J. Diederichs, A. K. Gangopadhyay, and J. S. Schilling, "Pressure dependence of the electronic density of states and T_c in superconducting Rb_3C_{60}," *Physical Review B*, vol. 54, pp. R9662–R9665, oct 1996.

[108] A. Oshiyama and S. Saito, "Linear dependence of superconducting transition temperature on Fermi-level density-of-states in alkali-doped C_{60}," *Solid State Communications*, vol. 82, pp. 41–45, apr 1992.

[109] P. W. Stephens, "The C_{60} Molecule," in *Physics and Chemistry of Fullerenes*, pp. 1–58, WORLD SCIENTIFIC, nov 1993.

145

[110] A. Zettl, L. Lu, X. D. Xiang, J. G. Hou, W. A. Vareka, and M. S. Fuhrer, "Normal-state transport properties of fullerene superconductors," *Journal of Superconductivity*, vol. 7, pp. 639–642, jun 1994.

[111] B. Lorenz and C. Chu, "High Pressure Effects on Superconductivity," in *Frontiers in Superconducting Materials*, pp. 459–497, Berlin/Heidelberg: Springer-Verlag, 2004.

[112] M. Knap, M. Babadi, G. Refael, I. Martin, and E. Demler, "Dynamical Cooper pairing in nonequilibrium electron-phonon systems," *Physical Review B*, vol. 94, p. 214504, dec 2016.

[113] A. Nava, C. Giannetti, A. Georges, E. Tosatti, and M. Fabrizio, "Cooling quasiparticles in A3C60 fullerides by excitonic mid-infrared absorption," *Nature Physics*, oct 2017.

[114] A. Y. Ganin, Y. Takabayashi, P. Jeglic, D. Arcon, A. Potocnik, P. J. Baker, Y. Ohishi, M. T. McDonald, M. D. Tzirakis, A. McLennan, G. R. Darling, M. Takata, M. J. Rosseinsky, and K. Prassides, "Polymorphism control of superconductivity and magnetism in Cs_3C_{60} close to the Mott transition.," *Nature*, vol. 466, pp. 221–5, jul 2010.

[115] R. H. Zadik, Y. Takabayashi, G. Klupp, R. H. Colman, A. Y. Ganin, A. Potocnik, P. Jeglic, D. Arcon, P. Matus, K. Kamaras, Y. Kasahara, Y. Iwasa, A. N. Fitch, Y. Ohishi, G. Garbarino, K. Kato, M. J. Rosseinsky, and K. Prassides, "Optimized unconventional superconductivity in a molecular Jahn-Teller metal," *Science Advances*, vol. 1, pp. e1500059–e1500059, apr 2015.

[116] P. W. Stephens, L. Mihaly, P. L. Lee, R. L. Whetten, S.-M. Huang, R. Kaner, F. Deiderich, and K. Holczer, "Structure of single-phase superconducting K_3C_{60}," *Nature*, vol. 351, pp. 632–634, jun 1991.

[117] Y. Iwasa, K. Tanaka, T. Yasuda, T. Koda, and S. Koda, "Metallic reflection spectra of K_3C_{60}," *Physical Review Letters*, vol. 69, pp. 2284–2287, oct 1992.

[118] Z. Zhang, C. C. Chen, and C. M. Lieber, "Tunneling Spectroscopy of M_3C_{60} Superconductors: The Energy Gap, Strong Coupling, and Superconductivity.," *Science (New York, N.Y.)*, vol. 254, no. 5038, pp. 1619–21, 1991.

[119] S. Lupi, A. Nucara, A. Perucchi, P. Calvani, M. Ortolani, L. Quaroni, and M. Kiskinova, "Performance of SISSI, the infrared beamline of the ELETTRA storage ring," *Journal of the Optical Society of America B*, vol. 24, no. 4, p. 959, 2007.

[120] C. Marini, E. Arcangeletti, D. Di Castro, L. Baldassare, A. Perucchi, S. Lupi, L. Malavasi, L. Boeri, E. Pomjakushina, K. Conder, and P. Postorino, "Optical properties of $V_{1-x}Cr_xO_2$ compounds under high pressure," *Physical Review B - Condensed Matter and Materials Physics*, vol. 77, no. 23, pp. 1–9, 2008.

[121] R. a. Kaindl, M. Wurm, K. Reimann, P. Hamm, A. M. Weiner, and M. Woerner, "Generation, shaping, and characterization of intense femtosecond pulses tunable from 3 to 20 μm," *Journal of the Optical Society of America B*, vol. 17, no. 12, p. 2086, 2000.

[122] M. Mitrano, *Nonequilibrium emergent phenomena in organic molecular solids*. PhD thesis, 2015.

[123] F. Wooten, "Optical Properties of Solids," *American Journal of Physics*, vol. 70, p. 1269, 2002.

[124] I. Wilke and S. Sengupta, "Optical 2 Nonlinear Techniques for Terahertz Pulse Generation and Detection — Optical Rectification and Electrooptic Sampling," pp. 41–72.

[125] C. O. Sullivan and J. A. Murphy, *Terahertz Sources , Detectors , and Optics*.

[126] S. L. Dexheimer, *Terahertz spectroscopy: principles and applications* , vol. 131. 2008.

[127] Q. Wu and X. C. Zhang, "Ultrafast electro-optic field sensors," *Applied Physics Letters*, vol. 68, no. 12, pp. 1604–1606, 1996.

[128] Q. Wu and X.-C. Zhang, "7 terahertz broadband GaP electro-optic sensor," *Applied Physics Letters*, vol. 70, no. 14, p. 1784, 1997.

[129] C. A. Schmuttenmaer, "Exploring dynamics in the far-infrared with terahertz spectroscopy," *Chemical Reviews*, vol. 104, no. 4, pp. 1759–1779, 2004.

[130] J. T. Kindt and C. A. Schmuttenmaer, "Theory for determination of the low-frequency time-dependent response function in liquids using time-resolved terahertz pulse spectroscopy," *The Journal of Chemical Physics*, vol. 110, pp. 8589–8596, may 1999.

[131] J. Loveday, *High-Pressure Physics*. Chapman and Hall/CRC, 2012.

[132] K. Syassen, "Ruby under pressure," *High Pressure Research*, vol. 28, no. 2, pp. 75–126, 2008.

[133] D. D. Ragan, R. Gustavsen, and D. Schiferl, "Calibration of the ruby R1 and R2 fluorescence shifts as a function of temperature from 0 to 600 K," *Journal of Applied Physics*, vol. 72, no. 12, pp. 5539–5544, 1992.

[134] D. M. Adams, R. Appleby, S. K. Sharma, and D M Adams et al, "Spectroscopy at very high pressures. X. Use of ruby R-lines in the estimation of pressure at ambient and at low temperatures," *Journal of Physics E: Scientific Instruments*, vol. 9, no. 12, pp. 1140–1144, 2001.

[135] R. C. Powell, B. DiBartolo, B. Birang, and C. S. Naiman, "Fluorescence Studies of Energy Transfer between Single and Pair Cr^{3+} Systems in Al_2O_3," *Physical Review*, vol. 155, pp. 296–308, mar 1967.

[136] T. H. Maiman, R. H. Hoskins, I. J. D'Haenens, C. K. Asawa, and V. Evtuhov, "Stimulated optical emission in fluorescent solids. II. Spectroscopy and stimulated emission in ruby," *Physical Review*, vol. 123, no. 4, pp. 1151–1157, 1961.

[137] A. D. Chijioke, W. J. Nellis, A. Soldatov, and I. F. Silvera, "The ruby pressure standard to 150 GPa," *Journal of Applied Physics*, vol. 98, no. 11, 2005.

[138] C.-S. Zha, H.-k. Mao, and R. J. Hemley, "Elasticity of MgO and a primary pressure scale to 55 GPa," *Proceedings of the National Academy of Sciences of the United States of America*, vol. 97, no. 25, pp. 13494–13499, 2000.

[139] F. D'Angelo, H. Němec, S. H. Parekh, P. Kužel, M. Bonn, and D. Turchinovich, "Self-referenced ultra-broadband transient terahertz spectroscopy using air-photonics," *Optics Express*, vol. 24, no. 9, p. 10157, 2016.

Acknowledgements

Along the years of my PhD I already had the chance of expressing my gratitude to most of the people who helped and supported me. Nevertheless, I would like to spend a few more words to thank friends and colleagues.

I will start by thanking my supervisor, Prof. Andrea Cavalleri, whose charisma and energy always influenced my working attitude. I thank him for his patience, when along the first year, he was entering my office accompanied by his typical "how is it going?", and he was nicely but astonishingly listening to my colourful description of how I spent my weekend or my last holidays. It took a while before I understood he was clearly referring to the lab activity.

I learned a lot form all the discussions we had, where he always found the time to explain all the details still obscure to me. I am very thankful for all the opportunities he gave me, including travelling and invitation to meetings with valuable scientific outcomes.

I clearly would like to extend my acknowledgements also to Michael Först, always available to help when needed.

I am really grateful to my coadvisor Prof. Wilfried Wurth, with whom I had the chance to discuss regularly not only about the outcome of my work, but also about more personal decisions. I appreciate his honesty and his insights about the academic life, which will be guiding me in my future decisions.

Beyond acknowledging people who guided and trained me, I want to thank all the people that, willing or not, were at my side during these years. I probably should apologize with the majority of them for having been moody. Despite my lack of

emotional control you have been there, to listen and give suggestions in front of a smoking Kaffe, or of a glass of Sekt (preferably Prosecco).

I need to start from Andrea, not only for having "adopted" me from work-day-one, but also for having accompanied me in all my trips :). He is my personal advisor and shopper, whose warm-heart has accompanied me in the most difficult decisions.

I definitely must thank all my officemates, Eliza, Mariana and Sven, as they are those who actively and passively shared all my experiences, and they have always shown great patience. I enjoyed our many attempts of learning foreign languages, the hours spent in listening to the Swiss radio, the gardening moments and, last but not least, the many gossiping ones.

I owe a big thank to "my" multiple PostDocs: Matteo, Michele and Gregor, with whom I established deep and unique connections.

In the first half of my PhD I met Matteo, who has been always there for me, and still is. He is a loyal friend. He taught me a lot and has been always willing to listen to my voice before taking any decision, helping my professional grow.

Later I met Michele, positive and genuine, whose energies seem to be endless. I honestly thank him for all the practical help he gave me and for his availability of giving wise advices. He tried hard to convince me that electronic is not magic, and I have to admit that he is probably right :). I was lucky to meet a colleague with whom connecting so deeply, even beyond the professional life. Not everyday one meets a person so skilled in "glove-launching".

Only at the very end of my PhD I met Gregor, completely different character than the italians, with a deep passion for music and arts. His creativity and style make him unique and still now I admire the way he combines all his interests to physics.

I want to thank Daniele, for his presence at work and in my personal life. This can be perfectly captured in our adventure at Centro Rivolta. Thank to Lorenzo and him, I discovered the Hamburger wildlife, became a St. Pauli supporter and one of the few buyer of Capitan Morgan Cola.

Thanks to Matthias, Thomas, Tobia, Razvan and all the MPSD team for all the beautiful shared moments and for the deep insights on the greman coffee.

A big source of energy came from sun, biers, sekt, and cocktails, that have just been an excuse to meet with all my closest friends without whom I would probably have a better liver, but a sadder story to tell.

I am so glad to have met Hauke and FRAncesca, two opposite personalties united by the love for metal music. This is how I like to think of them, even tough this is

not exactly true. The few kg added after I met them were well re-payed from all the excursions and laughs had together.

I was lucky to meet Francy with whom I shared a lot of stories, gossip or just insights on our life. She helped me to bring to Hamburg a forgotten piece of my italian life, and for this I am very grateful to her.

Many were the nights in the company of Roland, Francois, and Ravi, waiting for Dragon Ball, eating dates, or having one or two power naps. Every moment in their company brought warm feelings even in the coolest hamburger night.

I want to thank Ivanka, for her motivational skills. Without her I would have not made it to the gym not even half the times I have. I am still waiting though to go to the gym next Sunday together.

I wouldn't have probably survived any winter schools without the CFEL girls: Maria, Marta and Maria. Our Mediterranean temperament united us to our girl's lunches, which were a pleasant pause to the daily stress.

I owe a special acknowledgement to my family. Beyond the freedom I got in all the choices of my life, I received an unlimited support in all the decisions I made. I thank my mother and my father for having accepted my curiosity of moving abroad and for having shared with me wise and precious life insights. I owe a lot to my sister Agnese, my dearest and closest friend. She is my advisor, my mentor, my clone. I thank her for all her warnings and solace, and for having always been behind my steps.

I am very thankful to Fra and Chicca who, even if from far, stand at my side questioning my decisions helping my personal growth.

Last but not least, I am totally glad of having lived this experience at the side of Giulio. He guided me with his love, firmness, awareness and ethic. I am lucky to have you in my life.